UNIVERSITÉ DU QUEBEC À CHICOUTIMI

MÉMOIRE PRÉSENTÉ À
UNIVERSITÉ DU QUEBEC À CHICOUTIMI
COMME EXIGENCE PARTIELLE
DE LA MAÎTRISE EN INGÉNIERIE

PAR

WEILI WU

THE MODELING OF HOT TEARING IN ALUMINIUM ALLOY

January 2003

Bibliothèque
Paul-Émile-Boulet

UQAC
Université du Québec à Chicoutimi

Mise en garde/Advice

Afin de rendre accessible au plus grand nombre le résultat des travaux de recherche menés par ses étudiants gradués et dans l'esprit des règles qui régissent le dépôt et la diffusion des mémoires et thèses produits dans cette Institution, **l'Université du Québec à Chicoutimi (UQAC)** est fière de rendre accessible une version complète et gratuite de cette œuvre.

L'auteur conserve néanmoins la propriété du droit d'auteur qui protège ce mémoire ou cette thèse. Ni le mémoire ou la thèse ni des extraits substantiels de ceux-ci ne peuvent être imprimés ou autrement reproduits sans son autorisation.

Motivated by a desire to make the results of its graduate students' research accessible to all, and in accordance with the rules governing the acceptation and diffusion of dissertations and theses in this Institution, the **Université du Québec à Chicoutimi (UQAC)** is proud to make a complete version of this work available at no cost to the reader.

The author retains ownership of the copyright of this dissertation or thesis. Neither the dissertation or thesis, nor substantial extracts from it, may be printed or otherwise reproduced without the author's permission.

Dedicated to those who have filled my life with love

My husband, Xiaoguang;

My daughter, Dana; my son, Rudi

And

My dear parents in China

RÉSUMÉ

Le présente mémoire fait partie d'un projet de recherche d'envergure élaboré par la chaire industrielle Alcan-UQAC sur la solidification et la métallurgie de l'aluminium (CSMA), portant sur la fissuration à chaud des alliages d'aluminium coulés en régime semi-continu.

La modélisation de la microstructure a été réalisée à partir d'un modèle mathématique développé par un chercheur de la CSMA et de la simulation de la solidification d'un alliage Al-4.5%Cu; les résultats des simulations ont été ajustés et validés à l'aide de données expérimentales pertinentes.

L'information fournie par le modèle de microstructure, tel le champ de température, l'évolution de la fraction solide, la grosseur et la morphologie des grains, est essentielle à toute étude théorique portant sur la fissuration à chaud.

De manière à prédire la susceptibilité à la fissuration à chaud durant la solidification, deux critères ont été introduits séparément dans le modèle microstructural. Le critère développé par Lahaie et Bouchard (LB) est basé sur le comportement idéalisé d'un corps à l'état semi ou quasi solide, alors que celui de l'équipe Rappaz-Drezet-Grenaud (RDG) considère la diminution significative de pression à l'intérieur de la zone critique semi-solide, lorsqu'une pore à tendance à se former dans le réseau de dendrites, sous l'influence du changement de volume et des contraintes thermiques associées au processus.

Dans le modèle idéalisé de LB, on considère le comportement visqueux et les forces de capilarité du liquide résiduel qui entoure les grains pour évaluer les conditions de déformations critiques et les contraintes de rupture de l'assemblage quasi-solide. Pour un alliage donné, la déformation critique dépend principalement de la fraction solide, des conditions de solidification et du taux de déformation.

Nos simulations ont permis d'identifier les conditions de solidification qui peuvent conduire à la formation de criques; elles ont aussi été utilisées pour analyser la susceptibilité à la fissuration à chaud d'un alliage Al-4.5%Cu sous différentes conditions de solidification.

Pour vérifier la pertinence du modèle microstructural développé et des critères de fissuration suggérés, de même que pour valider le comportement d'un alliage Al-Cu en cours de solidification, quelques expériences ont été réalisées sur un simulateur reproduisant les conditions de solidification de la croûte d'un lingot industriel coulé en régime semi-continu. Les déformations sous l'effet d'une charge croissante ont été mesurées directement sur la surface du mini lingot expérimental, dont la croûte était quasi ou complètement solide. Le phénomène de fissuration fut provoqué sous ces conditions particulières de coulée et de contraintes.

Les résultats anticipés par la modélisation mathématique furent comparés à ceux obtenus expérimentalement. Les écarts parfois importants ont donné lieu à une discussion qui a permis de mettre en lumière la faiblesse des critères de fissuration proposés et de suggérer de nouvelles pistes plus prometteuses.

L'utilisation du critère LB dans le modèle microstructural conduit à des contraintes de rupture du même ordre de grandeur que celles mesurés expérimentalement. En améliorant le modèle LB, notamment en introduisant des paramètres réalistes de distribution spatiale de la fraction solide, tel que récemment proposé par un co-directeur du présent mémoire, on obtient une meilleure corrélation entre la déformation critique prédite par la modélisation et celle observée expérimentalement.

Les simulations réalisées en faisant appel au critère de fissuration proposé par RDG indiquent que cette approche peut être intéressante pour étudier la formation de criques dans la région centrale d'un lingot cylindrique. Cependant, d'autres travaux sont requis pour indiquer si ce critère est applicable à la fissuration à chaud dans la croûte d'un lingot conventionnel coulé en régime semi-continu.

Des voies nouvelles sont suggérées pour améliorer notre compréhension des mécanismes de fissuration à chaud des alliages d'aluminium.

ABSTRACT

Hot tearing is one of the "universal" defects in many aluminium casting products. The formation of hot tearing involves complex solidification phenomena and processing conditions. During the DC casting process, it often initiates at the surface and propagates towards centre. In the present work, a coupled solidification model (microstructure) and hot tearing model has been developed in order to predict the hot tearing susceptibility of aluminium alloys and thus to better control its occurrence.

The microstructure modeling in this project was progressed from two-dimensional simulation of Al-4.5%Cu binary alloy solidification, and the modeling results were compared with the experimental data. The information provided by the microstructural model, such as temperature field, evolution of solid fraction, the final grain size and the microstructure morphology, is essential for the further study of hot tearing.

In order to predict the hot tearing susceptibility during solidification, two hot tearing criteria with different aspects have been implemented into the microstructural model. The Lahaie Bouchard (LB) criterion is based on the mechanical response of the semi-solid body, while the Rappaz Drezet Grenaud (RDG) criterion considers the pressure drop from both thermal deformation and solidification shrinkage through the mushy zone.

In the microstructure – hot tearing model using LB criterion, by combining the constitutive law that reflected the viscous behaviour and the critical fracture based on the capillary force, a critical strain can be calculated to identify when and where hot tearing could occur. The critical strain is influenced by cooling condition, strain rate, solid fraction and alloy composition. The modeling results give an overall indication of the appearance of hot tearing, and can be used to investigate the susceptibility of hot tearing tendency influencing by the solidification parameters and the thermal properties of the Al-Cu alloys.

To valid the coupled microstructure-hot tearing model, some experiments have been carried out on the Direct Chill Ingot Surface Simulator (DCSS). The displacements under applied tensile loads were measured and the occurrence of the hot tearing was observed. The results from modeling and experiments were compared and discussed. The complete microstructure – hot tearing model (with the LB criterion), corresponds with the facture stress range found in the experimental data. By further correction based on a recently modified constitutive model, the critical strain range between the modeling and experiment can give better agreement to identify the appropriate condition for the susceptibility of hot tearing.

The modeling results from the RDG criterion showed that it is more suitable for the central type of hot tearing. It needs to be studied further to know whether this criterion is applicable for the surface hot tearing as in the case of DC cast sheet ingots.

ACKNOWLEDGEMENTS

It is with great pleasure that I acknowledge all those who were involved directly or indirectly in making this work a success.

First, I would like to thank my supervisors, Prof. Michel Bouchard, Dr. Xiaohong Yang and Dr. Daniel Larouche, for their guidance and encouragement.

Special thanks must be expressed to Gilles Lemire and Sébastien Duperré for their technical support and helping to perform all the experiments.

Finally, I thank Mr. Joseph Langlais from ALCAN Arvida Research and Development Centre for his kindly permission to use the DC ingot surface simulator to complete this project.

TABLE OF CONTENTS

CHAPTER 1

CHAPTER 2

CHAPTER 3

CHAPTER 4

CHAPTER 5

LIST OF FIGURES

CHAPTER 2

CHAPTER 3

CHAPTER 4

CHAPTER 5

LIST OF TABLES

CHAPTER 3

CHAPTER 5

CHAPTER 1

INTRODUCTION

CHAPTER 1

INTRODUCTION

Hot tearing is one of the most common and serious defects found in many aluminium casting processes, including continuous casting and Direct Chill semi-continuous casting. The cooling conditions in Direct Chill casting can produce thermal stress build-up and distortion in the freezing shell zone, which leads to hot tearing. It initiates at the surface region of the ingot and propagates towards the center through the shell zone causing a high rejection rate for various products.

The importance of studying and explaining the hot tearing tendency in aluminium alloys has been recognized for a long time. To prevent and eventually eliminate this defect, the first step is to understand the mechanisms of hot tearing and then find efficient methods to solve it in its embryonic stage. Computational modelling is thus a very useful tool in achieving this goal. Many investigations have contributed to a general understanding of the mechanisms of hot tearing and some theories have tried to interpret how various factors can affect hot tearing susceptibility.

The occurrence of hot tearing usually appears complex, involving many physical phenomena, such as heat transfer, fluid flow, solidification, microstructure evolution and thermal deformation. The interrelation of those features makes the problem more

This project strives to improve a two-dimensional microstructural model simulating the solidification phenomena in the surface region of DC casting, and to couple it with two hot tearing criteria in order to predict its occurrence at different conditions. The microstructural model provides basic information during the solidification, such as temperature distribution, evolution of fraction solid and the probable final microstructure, to predict hot tearing further. The two hot tearing criteria have different aspects: one is LB criterion*, which is based on the mechanical deformation of the semi-solid body, and the other is RDG criterion*, which considers the pressure drop associated with the shrinkage and thermal deformation in the mushy zone.

The solidification fundamentals, the mechanisms of hot tearing formation as well as the current modelling of microstructure and hot tearing are given in Chapter 2. Chapter 3 provides a detailed description of the complete microstructural–hot tearing model developed in this project. Chapter 4 discusses the modelling results. Finally, to validate the coupled microstructure–hot tearing model, some experiments were carried out with the Al-4.5%Cu alloy using a Direct-Chill casting ingot Surface Simulator. In Chapter 5 the experimental results are compared with those from the modelling, and the agreement and discrepancy between both are discussed.

*: See sections 2.2.2.3 and 2.2.2.4 for more details.

CHAPTER 2

LITERATURE REVIEW

CHAPTER 2

LITERATURE REVIEW

In recent years, computer simulation has become a cost effective tool for studying the characteristics of solidification process, which will eventually help prevent casting defects like hot tearing in its earliest stages, and optimize the properties of aluminum casting products during the manufacturing process. Numerical modeling is an excellent way to understand the solidification process, and improve quality control and processing in industry. Using mathematical and numerical models as a predictive tool can resolve difficulties in the manufacture of engineering components and make significant savings in both product development, and volume production.

2.1 MICROSTRUCTURE MODELING

The numerical simulation of aluminum casting is based on the fundamentals of solidification, analyzing the characteristics of individual problems, and the variable governing equations. Solidification is known to play an important role in the manufacturing of most metals. Microstructure and most defects originate in the mushy zone. Microstructural parameters (such as grain size and type, dendrite arm spacing, *etc*) form the basis that influences the mechanical properties in cast components of alloys.

2.1.1 Solidification Fundamentals

The basic theories of the solidification process are well described by Flemings [1], Kurz and Fischer [2]. Solidification is the transformation process from liquid to solid, comprises two basic phenomena: *Nucleation* and *Growth of Crystals* from the melt. It begins when the melt cools and reaches the liquidus temperature. The rate of this process determined by the rate of heat extraction from the system, the driving force (i.e. minimization of free energy ΔG) for nucleation, and the growth of crystals from undercooling (ΔT).

2.1.1.1 Nucleation of crystals

Nucleation is the first stage of solidification. It can be defined as the formation of smallest crystal from the melt capable of continued growth. As the temperature of the liquid is reduced below its freezing point, the solid tends to form in very small regions throughout the bulk of liquid. The change in the free energy to form a small embryo, which involves the volume free energy and the surface free energy, can be written as [3]:

$$\Delta G = \frac{4}{3}\pi r^3 \Delta G_v + 4\pi r^2 \gamma \tag{2.1}$$

where, ΔG_v is the change of volume free energy, r is the radius of nuclei and γ is the surface energy.

Figure 2.1 shows that the net energy to grow the embryo increases before reaching a maximum value. Embryos not reaching the maximum require more energy to grow, so they will shrink and dissolve again. When an embryo is equal or above the critical size r^*

($r \geq r^*$), nucleation occurs due to an energy reduction. The temperature at which this can occur is called the homogeneous nucleation temperature. For metals like aluminum, it is several tens of degrees below the equilibrium freezing point.

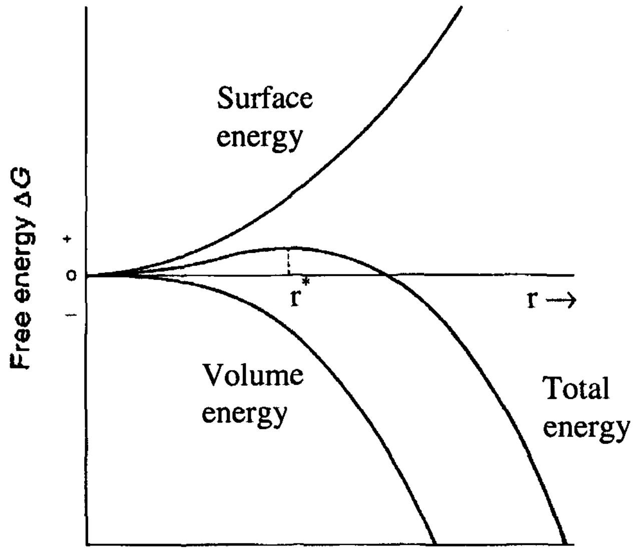

Figure 2.1 Free energy formation of a nucleus as a function of its radius [3]

However, it is common for the liquid to contain other solid particles, oxides on the melt surface, or to stick to the mold wall where the new crystals may form. In this case the interfacial energy component from Equation 2.1 can be reduced or almost eliminated. Thus, the presence of foreign nuclei in a melt can give a much lower nucleation temperature, involving progressively less supercooling of the liquid for more effective nucleation. This is known as heterogeneous nucleation.

The number and size of nuclei beginning the solidification process depend on the cooling rate of the melt. The nucleation rate and the growth rate are obviously boosted by increasing the undercooling. There are two main empirical methods, which represent the relationship between nucleation number N and the undercooling ΔT. *Continuous nucleation* assumes a continuous dependency of N (at a temperature where nucleation occurs continuously) once the nucleation temperature is reached, while the *instantaneous nucleation* assumes site saturation, which means all nuclei are generated at nucleation temperature T_n. Above the critical nucleation undercooling ΔT_n, almost no nuclei are formed (see Figure 2.2 [4]).They are evidently under the influence of the composition of alloys and, most importantly, the presence of grain refining particles, which are preferable sites for crystal nucleation.

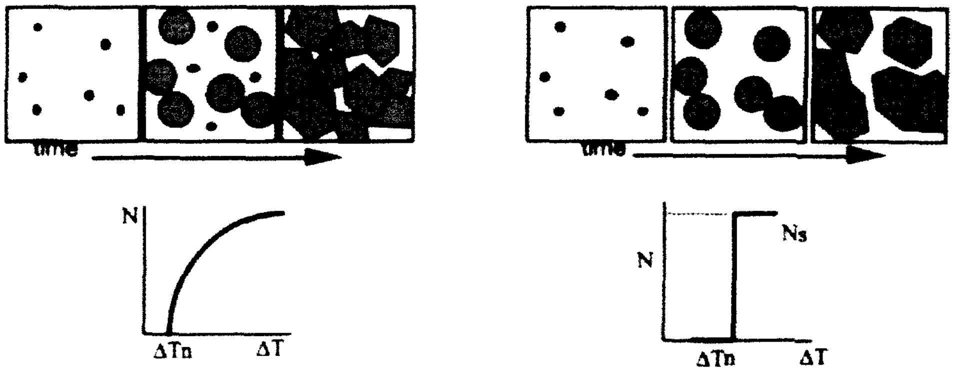

a) continuous nucleation

b) instantaneous nucleation (site saturation)

Figure 2.2 Schematic comparisons between continuous and instantaneous nucleation methods [4]

2.1.1.2 Growth of crystals

The growth of crystals is the second stage of solidification, when the heat is extracted through the solid, and the freezing front is cooled below the equilibrium freezing point. As the rate of heat extraction increases, the temperature of the solidifying front falls, and the rate of advancing front correspondingly increases. At this stage, the number of grains remains constant and solidification process advances via the lengthening of dendrites. Then the dendrite arm thickens until the grains are in contact.

Three growth forms are usually present in the solidification process: planar, cellular and dendritic (Figure 2.3 [5]). For pure metal, as the driving force for solidification increases, the solidification front undergoes such transitions. When the liquid temperature is higher than the freezing point of the melt and the temperature gradient of the liquid is positive, the solidifying front is known as planar. At higher advance rates, the front develops deep into the liquid and spaces evenly over the front. Ahead of the advancing interface, the liquid develops a negative temperature gradient. This is called cellular growth. At higher velocities still, the cells grow into rapidly advancing projections looking like a treelike complex geometry called dendritic growth.

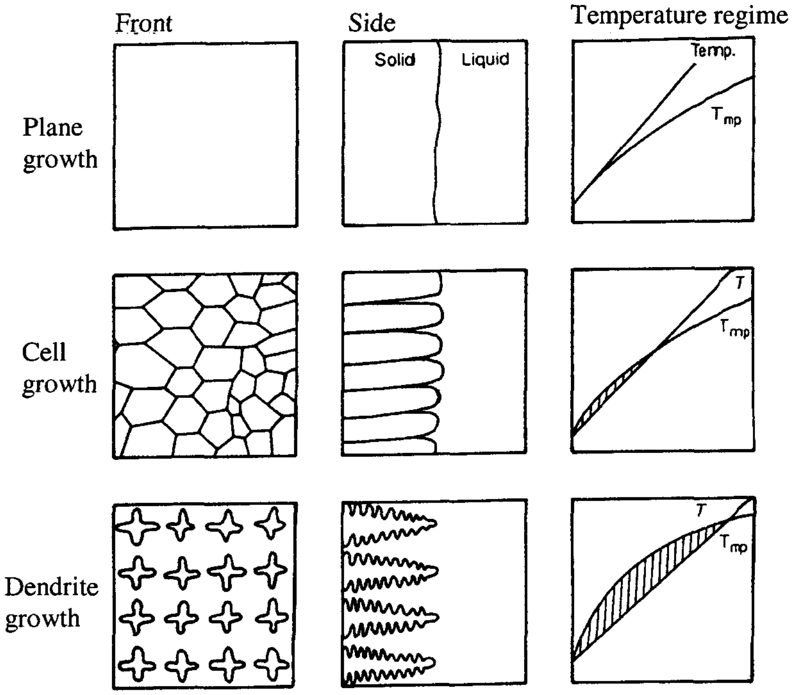

Figure 2.3 The transition of growth morphology [5]

In the case of alloys, the transition of growth morphology depends on the local constitutional undercooling. The criterion of the interface instability can be expressed as follows [5]:

$$\frac{G}{R} \leq -\frac{mC_0(1-k)}{kD} \tag{2.2}$$

Where, G is the temperature gradient in the liquid front, R is the growth velocity, C_0 is the original composition of the melt, m is the slope of the liquidus, k and D are the partition and the solute diffusion coefficients in the liquid respectively.

Figure 2.3 illustrates how the progressive increase in the constitutional undercooling causes progressive instability in the solidifying front. As the constitutional undercooling increases, the initial planar form changes to form cells. With further instability ahead of the solidification front, it is provoked to grow as dendrites. It is therefore clear that the constitutional undercooling, assessed by the ratio G/R, is the key factor that controls the form of growth. With reduced thermal gradient and increased growth velocity, the system tends to become dendritic growth, which is the common form of solidification in most commercial practice.

For aluminum alloys used industrially, the dendritic growth is the most common form of solidification. This study will therefore focus on the dendritic growth. It includes two main types: the columnar dendrite by constrained growth and the equiaxed dendrite by unconstrained growth.

Columnar growth

Directional or columnar solidification, where G and R are coupled, is often referred as constrained growth [2]. The advance rate of the isotherms constrains the dendrites to grow at a given velocity. This forces them to adopt the corresponding tip undercooling. The columnar dendrites are in contact with the mold wall and heat is conducted through the wall. The heat flow is parallel and opposite to the growth direction. Therefore, the melt is the hottest part of the system, see Figure 2.4 a) and b)), in which the growth velocity V is the critical solidification parameter in columnar dendrite growth.

A columnar dendrite grows both forwards and sideways, forming the primary dendrite axes (trunks). From the primary axes, it generates many secondary arms (Figure 2.5). During solidification, these arms bind together with almost atomic perfection, forming a single-crystal lattice known as a grain. The boundaries formed between trunks oriented differently, and originating from different nucleation events, are known as grain boundaries. In the metallurgy of wrought material, the grain size of the alloy is usually the most important structural feature. However, in casting products, the grain size is sometimes important, but most often, the secondary dendrite arm spacing is the most important structural length measurement.

Equiaxed growth

In equiaxed growth, heat flows from crystal to the melt and the dendrites grow freely and as rapidly as the imposed undercooling permits. The dendrites grow in a radial fashion until they impinge upon other dendrites, originating from different nuclei. In this case, the heat produced by the solidification must be transported through the melt, thus making the crystals the hottest part of the system. The heat flux is radial and in the same direction as the crystal growth, see Figure 2.4 c) and d). It is evident that the melt must always be cooled to below freezing point (requires undercooling), before the equiaxed dendrites can grow further. The undercooling *ΔT*, or more specifically, the concentration undercooling ΔT_c is the critical solidification parameter in equiaxed growth.

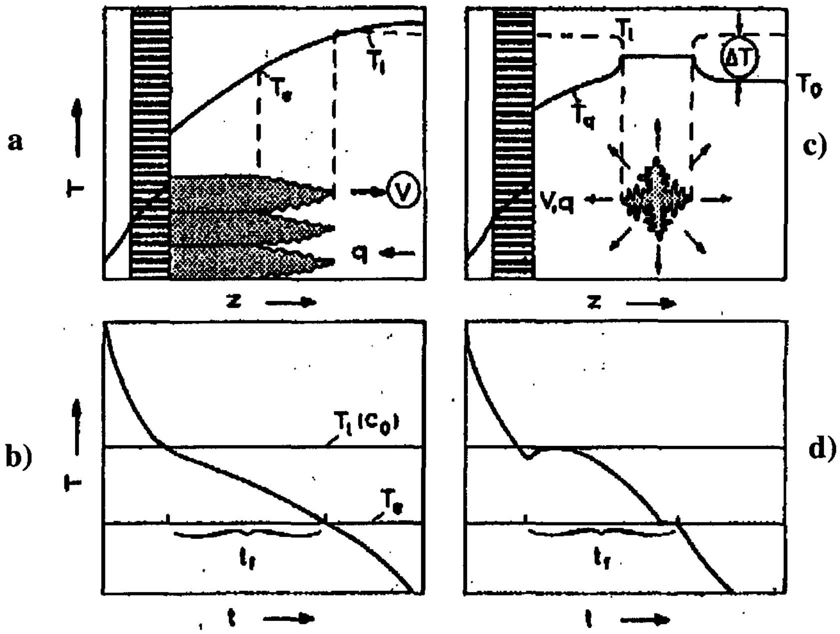

Figure 2.4 Thermal fields and cooling curves of alloy dendrites [2]
a) and b) are for columnar dendrite; c) and d) are for equiaxed

The challenge to predict the size of equiaxed grains involves having a better understanding of the original equiaxed nuclei. Three principal sources of nuclei can be considered [6]:

Constitutional Supercooling drives heterogeneous nucleation. Because the tips of the dendrites in the columnar grains are at a temperature below the bulk alloy liquidus temperature, an area in the liquid may become active with foreign nuclei.

Big-Bang mechanism. Equiaxed grains grow from predendritic shaped crystals that were formed when pouring at or near the mold walls. These crystals are carried into the bulk by fluid flow with some surviving.

Dendritic Fragmentation. During dendritic growth exposed to convection, parts of dendrites (i.e. dendrite arms) may break and be washed into the bulk.

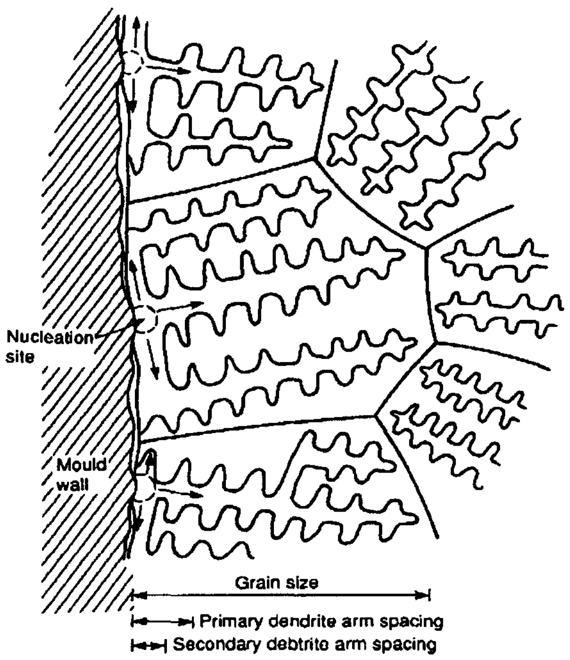

Figure 2.5 Schematic description of grain size and the dendrite arm spacing [5]

Columnar to equiaxed transition (CET)

The transition from columnar to equiaxed growth occurs when the melt has lost its superheat, thereby becoming slightly undercooled. New grains in the melt, growing either from detached dendrite arms or foreign nuclei, form a barrier ahead of the columnar zone.

Hunt [7] used selected columnar growth and nucleation models to determine whether the structure would be fully equiaxed or fully columnar, depend on where the temperature gradient was lower or higher when compared with a critical value. The factors promoting a columnar-to-equiaxed transition are: a large solute content which increases the value of ΔTc; a low temperature gradient that increases the size of the supercooling region; a small value for ΔTn (potent nucleation sites); and a large number of nuclei.

Rappaz and Gandin [8] have used the probabilistic model to predict the columnar to equiaxed transition (see Figure 2.6). In Figure 2.6, equiaxed grains nucleate and grow in front of the columnar zone and the condition of their formation is schematically illustrated. When these equiaxed grains are sufficient in size and number to block the advance of the columnar front, the columnar-to-equiaxed transition (CET) will occur. Their results indicated the importance of alloy composition and cooling rate in the transition.

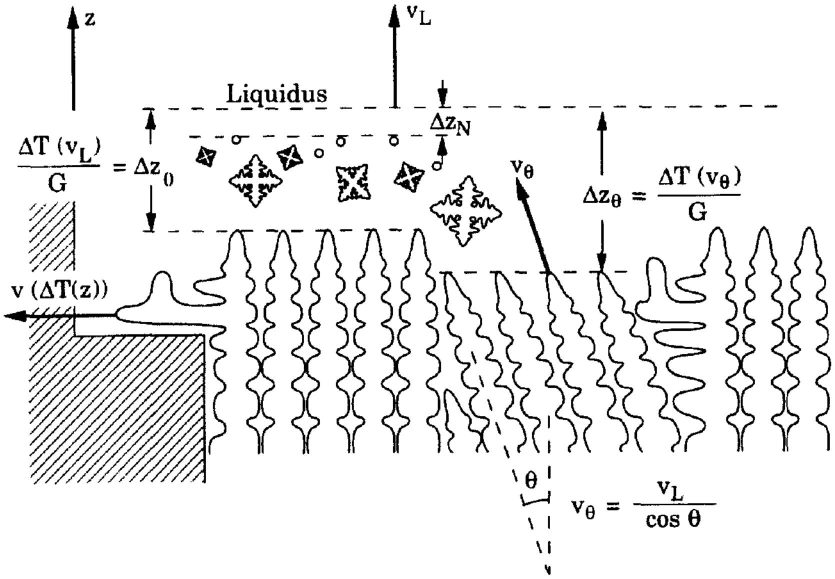

Figure 2.6 Formation of equiaxed grains ahead of the columnar front [6]

By adding the inoculants known as grain refining master alloys, this transition can be greatly encouraged [9, 10, 11].

Eutectic Growth

For many dilute aluminium alloys, eutectic growth will usually form during the last stage of solidification. As a result, secondary phases are generated near the end of freezing. The basic difference between eutectic growth and dendritic growth is that in a eutectic alloy, two solid phases form simultaneously from the melt. Eutectic solidification involves the following stages: eutectic liquid is supercooled; one of the solid phases begins to nucleate. Repeated nucleation and/or overgrowth of one solid phase by the other produces a eutectic grain that has a common liquid-solid interface. The solute rejected into the liquid by each phase is taken up by the adjacent phase particles.

When a eutectic liquid solidifies, the resulting material generally consists of a dispersed, two-phase microstructure approximately ten times finer than dendrites, formed under the same conditions. One of the interesting characteristics of eutectic alloys is their great variety of microstructures, which are classified into three categories: regular, complex regular and irregular. Al-Si foundry alloys are often of near-eutectic composition due to their excellent castability.

2.1.1.3 Microstructure

Dendritic solidification microstructure is characteristic of most aluminum alloy castings. The most important structural character to describe the dendrite structure is the secondary dendrite arm spacing (called DAS). DAS for both columnar and equiaxed growth are shown in Figure 2.5. The mechanical properties of most cast alloys strongly depend on it. As DAS decreases, the ultimate tensile strength, ductility and elongation will increase at the same time.

The secondary dendrite arm spacing is controlled by the cooling rate and coarsening process, (i.e. by the local solidification time). To reduce its surface energy, the dendrite has to reduce its surface area: small arms prefer to go into solution and large arms tend to grow at their expense, so that the average spacing between arms increases.

The general relationship between dendrite arm spacing and the local solidification time can be described as:

$$\lambda_2 = K * t_f^{\ n} \tag{2.3}$$

Where, λ_2 is dendrite arm spacing in micrometer, t_f is the local solidification time in seconds, K is a proportionality coefficient and n is between 0.3-0.4. For an Al-Cu alloy system, K and n are 7.5 and 0.39 respectively [5, 12].

Fine dendrite arm spacing is usually associated with a less microsegregation and uniform distribution of small constituent particles, and therefore, it is generally preferred.

The casting microstructure morphology relies on the macro thermal parameters like temperature gradient G and solidification rate R. As the ratio of G/R decreases, the microstructure changes from planar, cellular, and columnar dendritic to equiaxed dendritic, (see Figure 2.7). If the thermal gradient of the liquid is lower than a certain value, the columnar to equiaxed transition will occur [4, 7]. For dendritic solidification, the secondary arm spacing is decreased by increasing the castings cooling rate [2]. Based on the experiments, Alicia E. Ares et al observed that both the primary and secondary arm spacing has a peak value during the transition from columnar to equiaxed region as shown in Figure 2.8 [13].

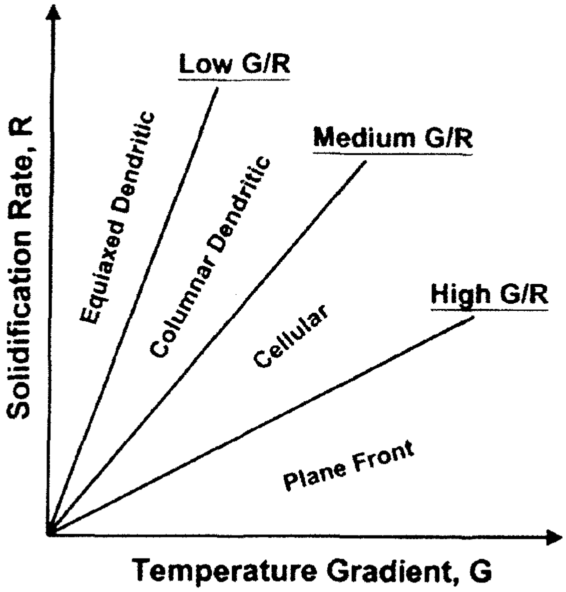

Figure 2.7 As-cast grain morphology as function of temperature gradient *G* and solidification rate *R* [4]

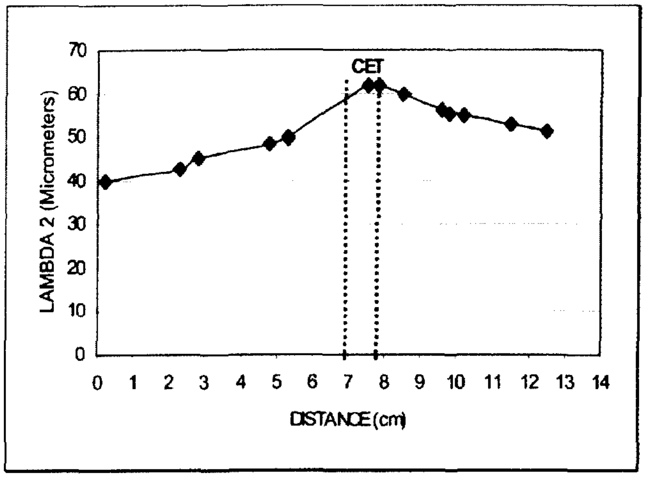

Figure 2.8 The secondary arm spacing λ_2, for Al-4%Cu alloy as a function of distance from the bottom [13]

2.1.2 Microstructure Models

Based on the fundamentals of solidification and the understanding of physical phenomena and material behaviors, a lot of effort has been made to establish a useful mathematical and numerical model of the casting process. Current modeling techniques are capable of restricting mistakes during the design process on computer and of predicting certain critical microstructure and casting defect features.

The microstructural model is the center point of solidification modeling. Using solidification kinetics can provide essential information, such as grain size, dendrite morphology, the evolution of fraction solid, *etc.*

Generally there are two approaches to microstructure modeling [14,15]: microscopic and macro-microscopic modeling. Microscopic is more fundamental that uses nucleation and dendrite growth laws to estimate the evolution of fraction solid during the solidification process. Macro-microscopic uses heat transfer equations to give an overview of the solidification paths for different regions of the castings. The basic mechanisms of nucleation and growth at the microscopic scale have been combined together with macroscopic continuity equations. To achieve these goals, some commercial codes in FEM/FDM analysis were developed and used, such as ProCAST, ABAQUS and MAGMASOFT, etc. [16, 17, 18, 19].

2.1.2.1 Modeling of heat transfer

Heat transfer in the earlier stages of solidification affects the microstructure evolution and its final mechanical properties of casting. The heat balance in the system forms the basis for solidification modeling. At one point (shown in Figure 2.9 [20]), the external and internal sources of heat flow to the system are equal to enthalpy change of the system:

$$q_e + q_i = \rho c_p \frac{\partial T}{\partial t} \tag{2.4}$$

where q_e is the external heat flux into the system, q_i is the heat generated inside the system, and ρc_p is the volumetric specific heat. The left-hand-side of Equation 2.4 is the heat flow to the system (from both external and internal sources) and the right-hand-side of equation represents the change of enthalpy in the system.

The external heat flux q_e to the system is carried out by conduction. The two-dimensional system can be written as:

$$q_e = div(\kappa \cdot gradT) = \kappa \cdot (\frac{\partial^2 T}{\partial x^2} + \frac{\partial^2 T}{\partial y^2}) \tag{2.5}$$

where, κ is the thermal conductivity.

In the solidification process, the internal heat flux q_i is related to the latent heat release, and can be written as:

$$q_i = L\frac{\partial f_s}{\partial t} \tag{2.6}$$

where, L is the latent heat of fusion per volume and f_s is the fraction solid.

Combining Equations (2.4) to (2.6) together:

$$\kappa \cdot (\frac{\partial^2 T}{\partial x^2} + \frac{\partial^2 T}{\partial y^2}) = \rho c_p \frac{\partial T}{\partial t} - L \frac{\partial f_s}{\partial t} \tag{2.7}$$

The term $\frac{\partial f_s}{\partial t}$ functions like a bridge between macroscopic modeling and microscopic modeling. For different growth morphology, such as columnar and equiaxed, $f_s(T)$ must be solved by a different methods [15].

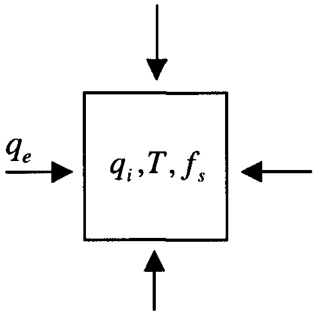

Figure 2.9 Heat balance in a simplified system [20]

2.1.2.2 Modeling of solidification kinetics

Nucleation modeling

Nucleation models are based on the assumption that the nucleation site frequency is related to the undercooling [2]. The classic nucleation (called instantaneous nucleation, see Figure 2.2) model is given as [15]:

$$\dot{n} = \frac{dn}{dt} = K_1[n_0 - n(t)]\exp(\frac{-K_2}{T(\Delta T)^2}) \tag{2.8}$$

where, n_0 is the initial nucleation site density and n(t) is the nucleation site density (or the grain density) at the time *t*. K_1 is proportional to the collision frequency of the atoms in the melt with the heterogeneous nucleation sites, and K_2 is related to the interfacial energy balance between the nucleus, the liquid and the foreign nucleation site. This nucleation law activates all available nuclei at a very small range of undercooling.

Assuming that the available number of nuclei is much higher than the active ones, a power law and an exponential law are each described as follow [21]:

$$\dot{n} = k_1 \cdot \Delta T^n \tag{2.9}$$

$$\dot{n} = k_2 \cdot (\exp[k_3 \cdot \Delta T] - 1) \tag{2.10}$$

The adjustable parameters k_1, n, k_2 and k_3 are affected by the adaptability of the models [4].

Furthermore, if all nuclei of a certain class are active at a certain undercooling, it is natural to relate the nucleus density to the undercooling. Taking this argument into account, Thévoz et al [22] proposed a statistical approach (called Gaussian distribution), which indicates a continuous dependency of *n(t)* on the temperature:

$$\dot{n} = \frac{dn}{dt} = \frac{n_0}{\sqrt{2\pi}\Delta T_\sigma}\exp[-\frac{(\Delta T - \Delta T_N)^2}{2(\Delta T_\sigma)^2}] \tag{2.11}$$

ΔT_N is the average nucleation undercooling and ΔT_σ is the standard deviation of nucleation. This relationship is plotted in Figure 2.10.

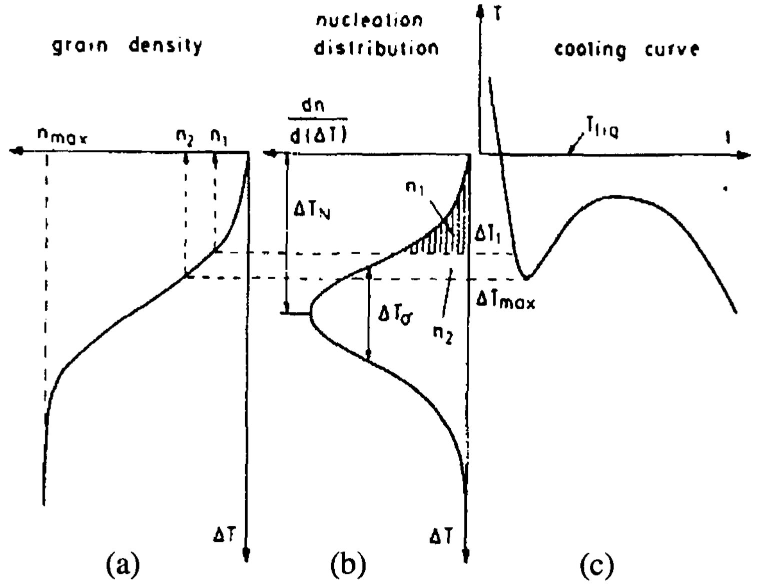

a. grain density; b. nucleation distribution; c. cooling curve

Figure 2.10 continuous distribution of nucleation sites used in modeling of equiaxed solidification [15]

Figure 2.11 shows the calculated dendritic equiaxed grain sizes by using different nucleation laws. Nucleation is assumed to occur at a Gaussian distribution, which corresponds more between predicted and experimentally observed grain sizes [23].

Dendritic growth modeling

Dendritic growth is found in the majority of industrial aluminum alloys. From the dendrite formation point of view, columnar and equiaxed growths are considered as constrained and unconstrained respectively. Accordingly, the modeling of dendritic growth is distinct, but both are aspects of heat transfer and solute diffusion in the system.

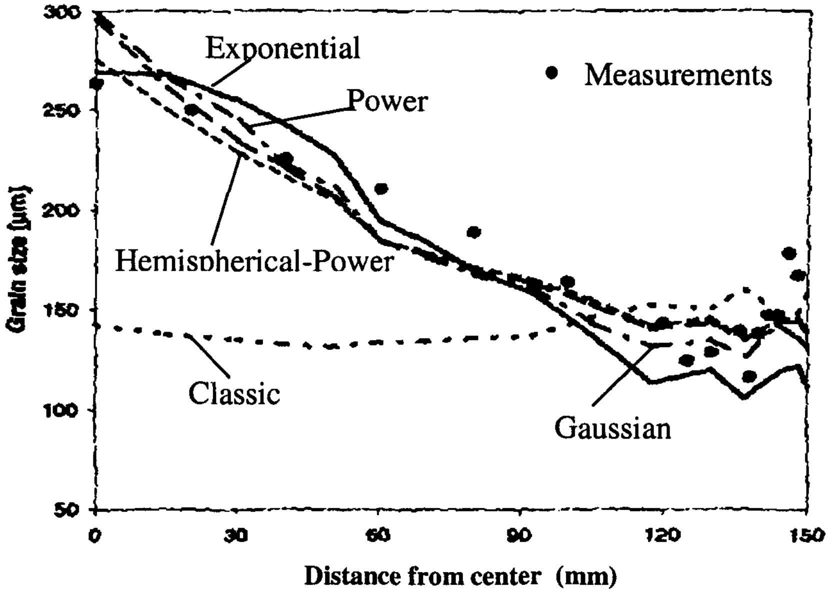

Figure 2.11 Calculated grain size, using different nucleation laws [21]

a) Columnar growth modeling

Columnar dendrite growth modeling is based on knowing the solidification front velocity [15]. Columnar dendrites always grow in a positive liquid temperature gradient so that the latent heat of fusion is dissipated through the solid. Columnar dendrite grows in direct contact with the heat sink and depends on the temperature gradients in system.

The growth rate of the columnar dendrite tips is directly related to the speed at which the corresponding liquidus isotherm is moving. The tip growth rate V is an elementary parameter in columnar dendrite growth. Traditional models did not track the dendrite tip position, thus the growth velocity was only derived from the temperature field (see Figure 2.12). In Figure 2.12, T^* is the dendrite tip temperature, T_l is liquidus temperature, T_q is measurable temperature, and G_l^* and G_s^* are the thermal gradients at the interface in the liquid and solid phases, respectively.

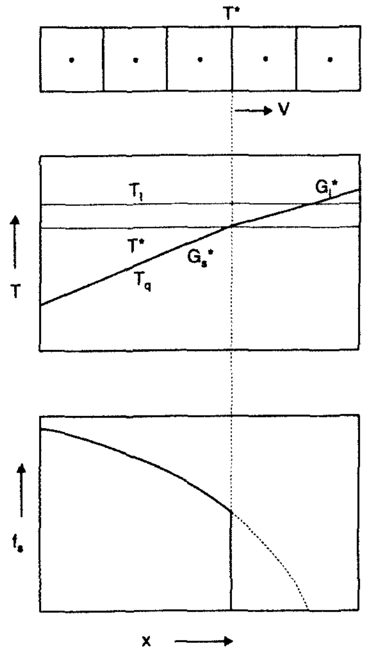

Fig 2.12 Traditional modeling of columnar growth [20]

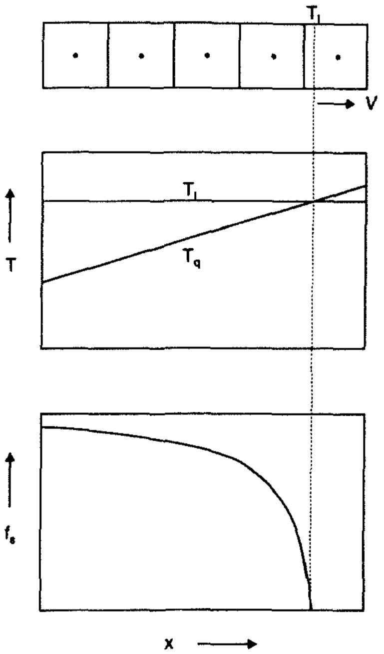

Fig 2.13 Flood and Hunt model for columnar growth [20]

Later advanced models included the effect of tip undercooling on growth velocity. Flood and Hunt model kept the tip position at the boundary, but changed the location of the meshes at each time step in the model, as shown in Figure 2.13.

As the interface position is tracked, the meshes are not relocated in the models afterwards. The interface position is tracked by using the truncated Sheil's equation, the truncated Brody-Fleming's equation, or Giovanola - Kurz model (see Figure 2.14).

All the above-mentioned models use the heat balance Equation 2.4 and solute diffusion equations. The temperature change (undercooling), the fraction solid behind solidifying interface, the columnar dendrite tip radius, and the tip growth velocity are all calculated according by relevant methods.

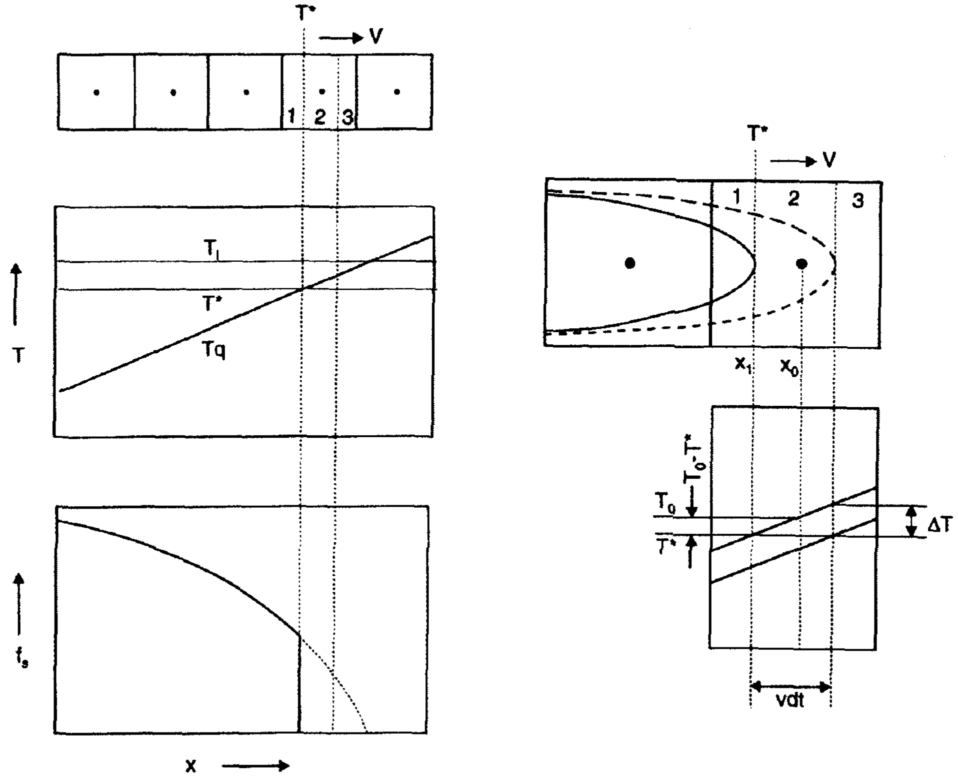

Fig 2.14 Current approach to columnar growth [20]

b) Equiaxed growth modeling

Equiaxed growth modeling is totally different from the columnar one. In equiaxed growth, the crystals grow independently in a supercooled melt and are the hottest part in the system. The heat produced by the solidification must be transferred through the melt. The heat flux is radial and in the same direction as the growth [2]. Hence, parameters like grain number n, grain size R, growth velocity V and undercooling ΔT or concentration undercooling ΔT_c are all interacting in equiaxed growth. In this case, the velocity of the interface is related to the local undercooling, rather than to the isotherms, and the density of the grains plays a more important role. In brief, equiaxed growth modeling must couple the nucleation and growth laws with the heat balance equation of the system [15].

In the equiaxed model the total volume is divided into small volume units. The temperature in each volume unit is considered to be uniform. The grain number n is first calculated using the nucleation law. The growth velocity V and the mean tip radius $\bar{R}$ of equiaxed dendrite are deduced from the heat balance and solute diffusion equations. Then the volume fraction solid can be calculated. Figure 2.15 is a schematic representation of a solute diffusion model for equiaxed dendritic solidification, in which δ is the solute boundary layer thickness, f_s and f_g are the standard fraction solid and the volume fraction solid of equiaxed grain, R_g and R_{tot} are the radius of a grain envelope and the final equiaxed grain, respectively.

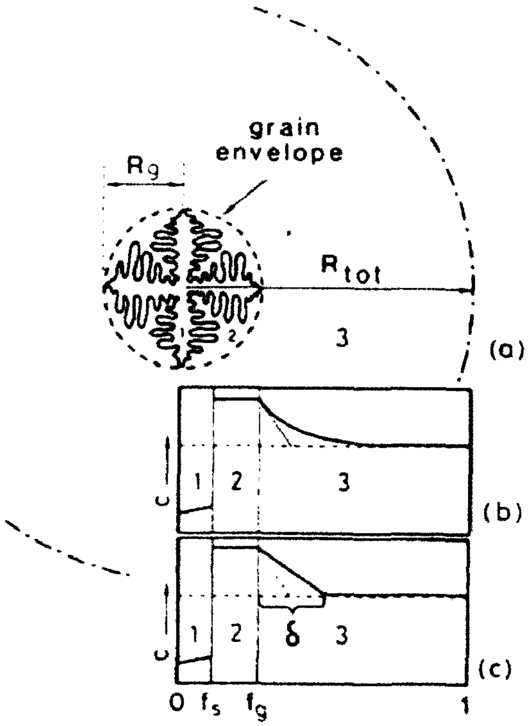

1-solid 2- interdendrite liquid 3-outside liquid

Figure 2.15 A solute diffusion model for equiaxed dendritic solidification [15]

c) Columnar to equiaxed transit Modeling

Columnar to equiaxed transition is the result of the competition between columnar and equiaxed structure. This phenomenon is very important in the solidification process, as it could significantly influence the properties of the final casting products [24].

In the columnar growth zone, if the interface velocity is relatively low due to the latent heat released ahead of the solidification front, the equiaxed grains could nucleate and rapidly develop to block and stop the columnar dendrite growth. A quantitative model to evaluate this transition condition was given by J. D. Hunt [7], which can predict whether the structure will be fully equiaxed or columnar.

If:

$$G_L < 0.617 \cdot N_0^{\frac{1}{3}} \cdot (1 - \frac{\Delta T_n^3}{\Delta T_c^3}) \cdot \Delta T_c \qquad (2.12)$$

the structure will be fully equiaxed. Where G_L is the temperature gradient in the melt, N_0 is the number density of nucleating sites, ΔTn is the nucleation undercooling and ΔTc is the growth undercooling of the columnar dendrites.

If:

$$G_L > 0.617 \cdot (100 * N_0)^{\frac{1}{3}} \cdot (1 - \frac{\Delta T_n^3}{\Delta T_c^3}) \cdot \Delta T_c \qquad (2.13)$$

the structure will be fully columnar. Thus, from the characteristics of the alloy, the nucleation parameters and the stationary growth rate of the columnar front, it is possible to calculate the critical gradients from which the structure is switching from 100% columnar to 100% equiaxed.

2.1.2.3 Modeling with the stochastic method

The recently developed stochastic or probabilistic modeling used a nanometers-to-micrometers scale simulation, as well as the discrete and crystallographic aspects of dendritic growth; unlike the above-mentioned deterministic models, which are based on the continuum equations and work with either the centimeters-to-meters (macrostructure) or of micrometers-to-millimeters (microstructure) scales [4, 25]. This method of modeling primarily uses mainly the *Monte Carlo* (MC) and the *Cellular Automaton* (CA) techniques. The divided meshes in this method are smaller than the grain size of the secondary dendrites arm spacing, which are determined by the statistic probability and present either liquid state or solid state (see Figure 2.16).

Individual grains are identified, their shape and size can be shown graphically throughout the solidification, and phenomena such as crystal remelting can be simulated [20, 26]. The significance of stochastic/probabilistic approaches is that the evolution of simulated microstructures can be directly visualized and compared with the actual microstructures from experiments at two different scales: dendrite grain characteristics such as the grain size and location, and the columnar-to-equiaxed transition size can be visualized at the micro-scale. Meanwhile, dendrite morphology (including dendrite tip, various dendrite arm spacing and micro-segregation patterns) can be viewed at the mesoscale, where the relative effects of the solidification parameters can be qualitatively predicted [11, 26].

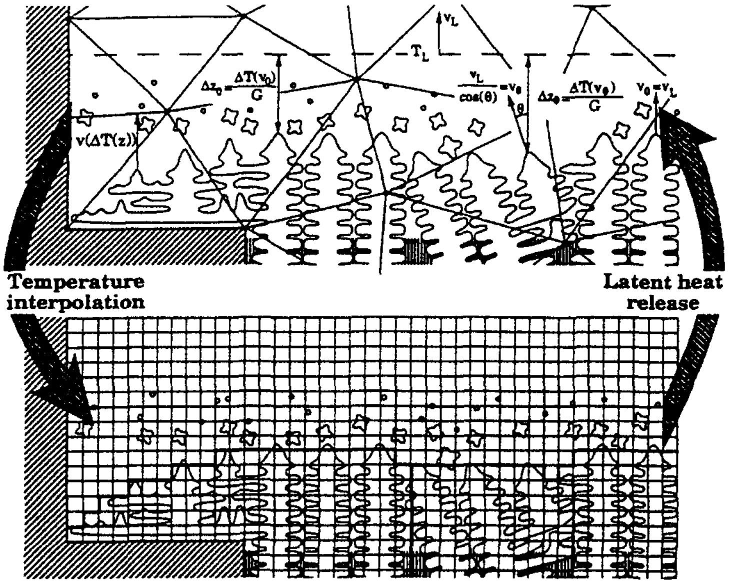

Figure 2.16 Schematic diagram of the coupling between the microstructure calculation using the cellular automaton and the thermal calculation by Finite Elements [25]

2.2 HOT TEARING MODELING

2.2.1 The Mechanisms of Hot Tearing

Hot tearing is recognized as one of the most common and serious defects found in aluminum castings. Figure 2.17 [27] shows the typical appearance of hot tearing in the microstructure and Figure 2.18 shows a filled hot tear in an Al-10%Cu alloy. The importance of studying and understanding the occurrence of hot tears in aluminum alloys has long been recognized. Various methods have been used to test and evaluate the severity of hot tears and its related properties [27, 28, 29, 30, 31] and several theories have attempted to explain their occurrence [32, 33, 34, 35, 36].

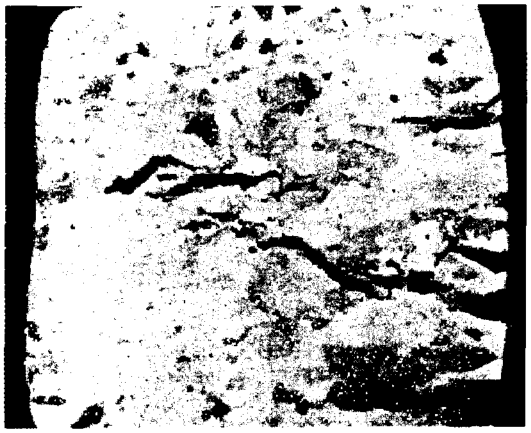

Figure 2.17 The typical appearance of hot tearing in the microstructure showing the multi-branched intergranular cracks [34]

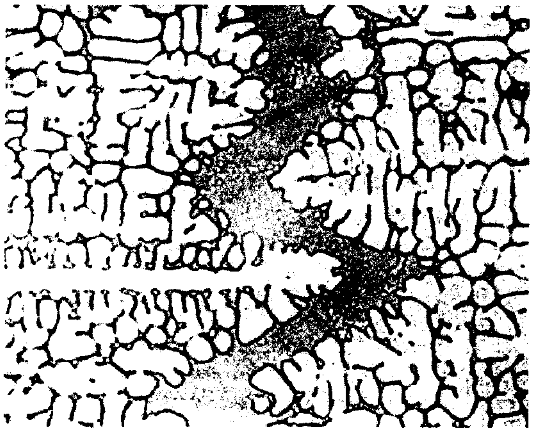

Figure 2.18 A filled hot tear in an Al-10%Cu alloy [5]

During the solidification process, the heat extraction induces surface stresses, which are generated by the contraction of metal. The type of cracks caused by the stresses is a uniaxial tensile failure in a weak material and is "intergranular" in nature, because they propagate along the grain boundaries where low melting point precipitates are found. Therefore, a tear occurs when liquid metal is still present during solidification, generally referred to hot tearing, whereas a crack is a fracture occurring when the material is entirely solidified [5, 37].

Hot tearing develops at high temperatures during cooling and solidification of the casting. Nearly all researches indicate that the hot tearing most likely occurs in the mushy zone at the temperature near the solidus temperature where the fraction solid is close to one. In this zone the solidifying process is in a critical film stage (see Figure 2.19 [38] $T_{cr} - T_s$). When the surrounding liquid cannot fill the gap between dendrites, and the strength of the metal cannot resist the tensile stress that developed while cooling, imposing itself across the already partially-solidified grain, hot tearing will occur, because the strength and ductility of the metal are very low there [36].

Early studies have found that, when the contraction of the solidifying casting is excessively restrained by the mold or cores, hot tears will easily occur in the weak areas where the strain is concentrated. Usually these weak areas are localized hot spots like gate and riser contacts, re-entrant angles or abrupt enlargements in the casting sections, where liquid films will retain the longest, becoming the preferred sites for hot tearing [33, 34, 37, 39]. With regard to hot tearing in DC casting, the hot tears occur mostly at the surface region of the ingots, because the stresses responsible for tears are primarily generated at the impingement point of the water curtain on the ingot surface [33].

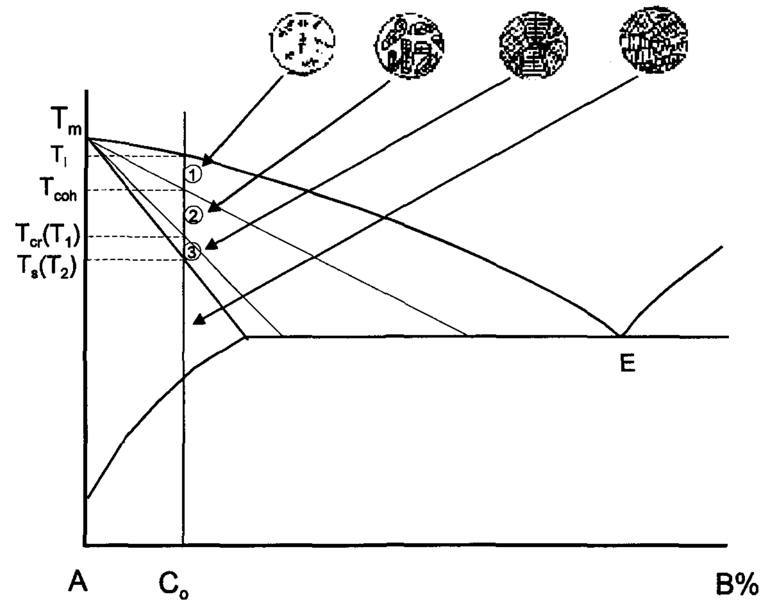

T_l Liquidus (f_l=1.0): solidification starts;
T_{coh} Coherent temperature (f_l=0.6): dendtirtes interlocks ;
$T_{cr}(T_1)$ Critical Temperature or Upper-limit Temperature (f_l=0.1): *liquid flow stops and metal begins to gain strength* ;
T_2 Lower-limit Temperature (f_l=0.01): hot tear takes place;
T_s Solidus (f_l=0.0): solidification finishes.

Figure 2.19 Solidification stages from the point view of hot tearing occurrence [38]

Based on the *film-strain* theory on hot tearing formation by Pellini [33], hot tearing susceptibility generally develops in the mushy zone at liquid fractions below 10%. It only occurs when stresses exceeding its strength and ability to deform in the hot tearing temperature range are produced in the metal (see Figure 2.20). While the hot zone is narrow and exists only a thin film, its strength is inadequate to withstand the accumulated strain. This may be enough to cause hot tearing in the weak liquid film [35].

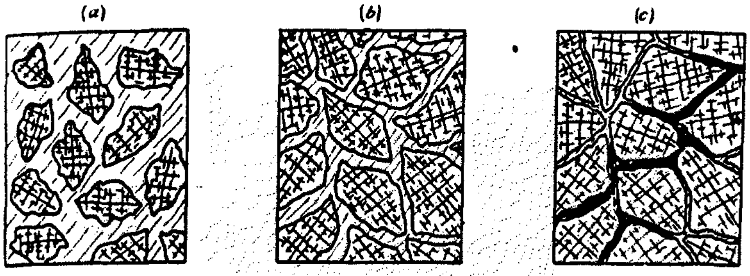

Figure 2.20 Mechanism of film-stage tearing [38]
a) Solid nuclei together with considerable liquid metal. Hot-tearing is not possible at this stage;
b) Crystals separated by thick liquid films. The stage when a "build-up" of strain in the possible hot spot approach;
c) Stage just before complete solidification. Thin liquid films separate crystals. The developed strain concentration was sufficient to cause hot tearing.

Scanning electron microscope (SEM) analysis reveals that grain boundaries, microstructural barriers and the differences in the stress/strain state play an important role in the earlier stages of hot tearing. The tear propagation decelerates as the tip of tear moves closer to the grain boundary [40, 41, 42, 43, 44]. An in-situ SEM observation by W. M. van Haaften [45] showed that hot tearing started at the weak spot, such as a pore or liquid film surrounding a grain boundary, which first opened as a wedge, then followed perpendicular to the tensile direction, and finally, propagated by a sliding motion, as shown in Figure 2.21.

Hot tearing in real castings is caused by a number of complex variables; the evaluation of the principal features is not always easy. However, the susceptibility to hot tearing generally varies with the chemical composition, microstructure of alloys and the casting conditions.

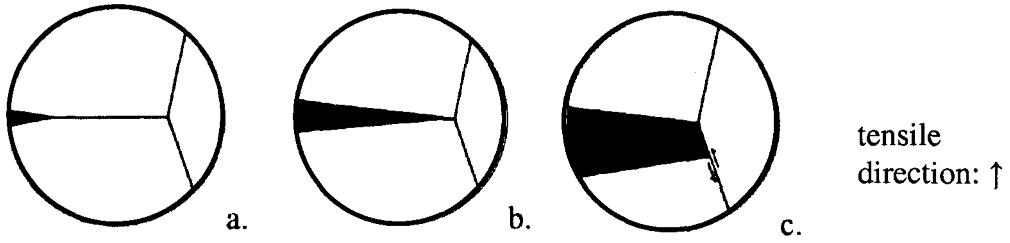

a) separation by a wedge b) crack arrest c) sliding

Figure 2.21 Schematic drawing of three stages of grain boundary separation [45]

The composition of alloys determines the freezing range and the duration of the film condition. A wider temperature range of the mushy zone and a longer time interval of the film stage may increase the tendency of hot tearing [27-30, 35, 46, 47]. Refined grain size and equiaxed dendrite morphology could reduce the susceptibility of hot tearing [27, 29, 30, 32, 35, 47, 48, 49, 50]. Higher pouring temperature and casting speed favor hot tears, while molds or core forms and the like are influenced by changing contraction conditions. In practice, all of these parameters are interactive, which makes prediction of hot tearing extremely difficult [28, 30, 31, 35, 51].

2.2.2 Modeling Approaches

According to the mechanisms of hot tearing, any variables influencing high temperature strength, ductility, shrinkage characteristics, or any conditions leading to dendrite separation, fractures and incipient cracks will change hot tearing tendencies.

Figure 2.22 gives an overall view of the most important parameters influencing hot tearing in the DC casting process. The susceptibility of hot tearing in any given alloy concerns its mechanical properties, which are determined by the microstructure, and by measuring the stress build-up in thermal casting conditions. Consequently, the solidification model alone is unable to predict hot tearing occurrence, because it lacks the indispensable factor: the stress-strain behaviors during solidification process are not included. Calculating thermal stresses and strains has been proven essential in predicting hot tearing. Thus, the prediction of hot tearing must combine both microstructure model providing basic information, and the thermo-mechanical model, which can give supplementary details influencing the mechanical properties during solidification process [52].

Though hot tearing prediction is still limited, the most recent method is to modify the technology at the planning stage through computer numerical modeling, in addition to traditional experimental investigation. Computer simulation of hot tearing utilizes a sequential thermo-mechanical analysis approach by helping of the existing finite element codes, such as ABAQUS, MARC, THERCAST, *etc* [17, 28, 39, 53, 54, 55, 56, 57].

There are different ways to achieve the predicting hot tearing tendency goal. In order to find an index or a critical value for the occurrence of hot tearing, most researchers simulate the rheological stress-strain/strain rate behaviors in the mushy zone and study the ability of interdendritic liquid flow to compensate thermally induced deformation.

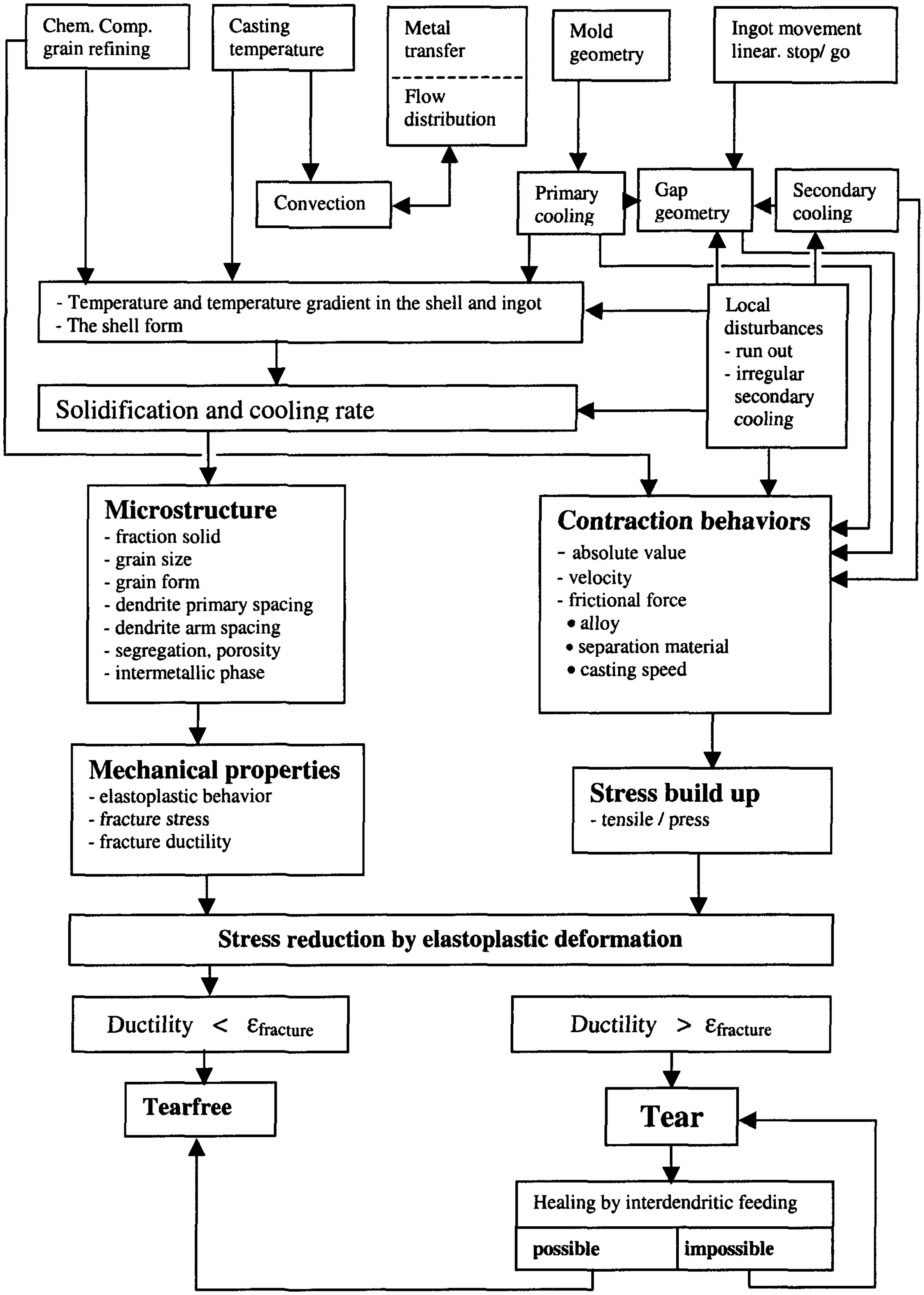

Figure 2.22 Important parameters influencing the hot tearing during the DC casting process [50]

2.2.2.1 Criteria function models

These models are based on empirical functions, which relate the local conditions (e.g., cooling rate, solidification velocity, thermal gradient, etc.) causing hot tearing. There are several indexes on the cracking susceptibility coefficient (CSC), which attempt to describe hot tearing tendency. Some models are based on the relationship between vulnerable time (interdendritic separation time) and the feeding time for stress- relaxation processes by considering the accumulation of strain in a local hot spot [5, 58, 59]. Others are based on the competition between the solidification and shrinkage rates during a risk period, i.e. the later stage of solidification, when grains cannot move freely and accommodation becomes difficult. The solidifying front requires time through this zone while the area in question contracts itself at the component rate [60, 61, 62]. Different models evaluated tensile strength and ductility during the solidification process, as well as the relationship between temperature, fraction solid and mechanical properties of alloys. They indicated that a critical tensile stress is responsible for the nucleation and propagation of hot tears [48, 50, 63, 64].

The commonly used criterion was a cracking susceptibility coefficient index (CSC), proposed by Clyne and Davies [58], which is defined as:

$$CSC = t_v / t_r \tag{2.14}$$

Where, t_v is the vulnerable time period for tears to spread, and t_r is the time available for stress relaxation processes such as liquid and mass feeding. When fraction solid f_s is between 90% and 99% (according to the time t_v), the liquid flow will be restricted due to narrow interdendritic channels, and when f_s is between 40% and 90% (correspond to the time t_r), the feeding to incipient tears is possible. This CSC index can be used to rank various alloys in terms of their susceptibility or resistance to hot tears, but it is unable to predict whether the casting made from a given alloy under certain process and cooling conditions will exhibit hot tear defects.

Katgerman [59] later took the coherency temperature into account and modified the above mentioned fraction solid range. The limit of t_v would be between 0.99 and f_s^{cr}, which corresponds to the critical point i.e. interdendritic liquid film formation. The limit of t_r would be between f_s^{cr} and the f_s^{coh}, which corresponds with the dendrite coherency point.

Considering the accumulation of strain in a local hot spot, Campbell [5] modified the index and redefined it as follows:

$$CSC = \frac{\alpha \Delta T L a}{l^2} \cdot \frac{t_v}{t_r} \tag{2.15}$$

Where, α is the coefficient of thermal expansion, ΔT is the undercooling temperature from the liquidus, L is the casting length, a is the grain size and l is the length of the hot spot measured in the direction of strain. This CSC index is empirical and suitable for a qualitative assessment of relative hot tearing tendencies of different alloys. The first term on the right hand side refers to the thermal strain accumulating at the hot spot. Since the solidification model can provide accurate information about grain size and fraction solid, it is possible to estimate t_r and t_v. Then one can calculate the hot tearing susceptibility for a given casting design by using the above criterion. This gave the typical "Λ" curve as shown in Figure 2.23.

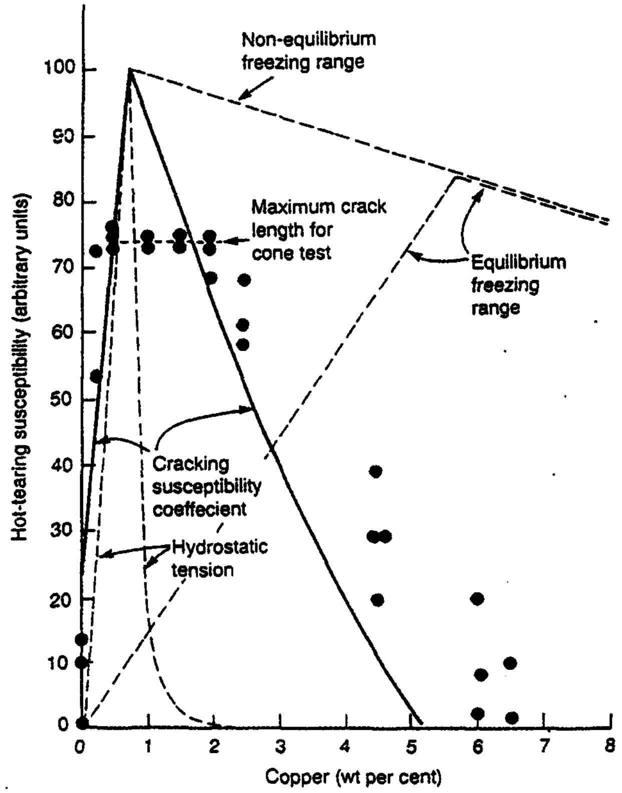

Figure 2.23 A summary of Hot tearing response of Al-Cu alloy [5]

2.2.2.2 Rheological models

Assuming the semi-solid metal to be elasto-viscoplastic with strain rate dependent behaviors, i.e. the rheological properties in the mushy zone have a significant effect on the hot tearing, some rheological models are established based on the experimental observations [28, 53, 55, 57, 65, 66, 67, 68].

In a popular model, the total strain rate is the sum of the elastic strain rate $\dot{\varepsilon}^{el}$, the visco-plastic strain rate $\dot{\varepsilon}^{vp}$, the thermal contraction strain rate $\dot{\varepsilon}^{th}$ and the transformation strain rate $\dot{\varepsilon}^{tr}$ [57, 69]:

$$\dot{\varepsilon} = \dot{\varepsilon}^{el} + \dot{\varepsilon}^{vp} + \dot{\varepsilon}^{th} + \dot{\varepsilon}^{tr} \tag{2.16}$$

In this equation, the elastic strain is given by Hooke law, the visco-plastic strain is determined by Parzina law or others, the thermal contraction strain is linked to the local cooling rate and the dilatation coefficient, and the transformation strain depends on the fraction solid and shrinkage rate. In these calculations, the solid-state rheology is determined by tensile tests. For alloys that have a large freezing range, a creep strain may be included in the calculation [70]. This model gave a critical value of thermo-mechanical and metallurgical parameters involving the formation of hot tearing in the solidification range.

U. Chandra [55] proposed a methodology using a sequential thermo-mechanical analysis approach. It consists of a thermal model for the temperature and solid/liquid fraction, a stress model for the strain rate and accumulated strain, and a strain based hot tear/fracture criterion for its occurrence. A liquid fraction, a hot tears or fracture in the liquid film takes place under one-dimensional strain condition. The dependent critical strain ε_{fr}, and the equivalent strain ε_0, including any relevant terms of the strain tensor, are all calculated and compared. If the accumulated equivalent strain exceeds the critical strain corresponding to the liquid fraction, hot tearing may occur.

Instead of using the equivalent plastic strain as criterion B. Magnin [67] et al proposed using a positive plastic strain $\varepsilon^{ii}_{p\max}$ as a hot tearing criterion for billets. They investigated both the ductility and rheology behaviors for Al-4.5%Cu alloy by tensile testing, and provided an elastoviscoplastic law. If the calculated $\varepsilon^{ii}_{p\max}$ is greater than the fracture strain curve determined experimentation, the hot tearing may occur, as shown in Figure 2.24.

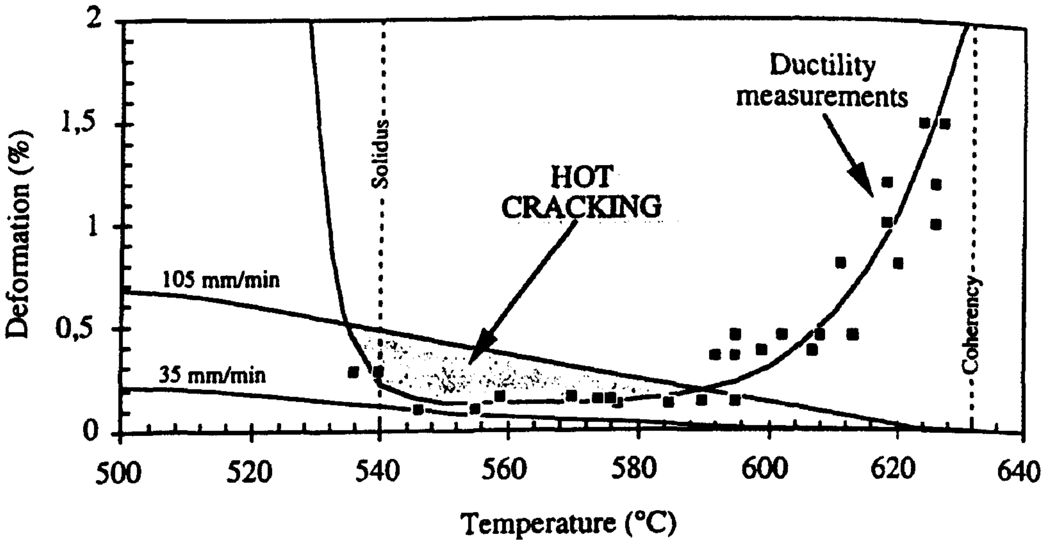

Figure 2.24 Prediction of hot cracking risk by comparison of ductility in semi-solid state with computed strain in the center of the billet for two different casting speeds [67]

In order to represent complex bodies with complex rheological properties, Liangyi Zhao et al [66] proposed a five-component elasic-visco-plastic rheological model for Al-4.5%Cu alloy. A creep equation can be obtained and the rheological parameters can be defined from this model. The strain can therefore be calculated to identify and analyze hot tearing, which may happen when the strain exceeds the ductility of the alloy.

2.2.2.3 Physical models

These models are based on deformation mechanisms. The interdendritic fracture appearance of hot tears originating at near-solidus temperature indicates that the basic mechanism of hot tearing is a separation at the film stage of solidification. It has a tight relationship with the stress generating from the build up of stresses during the solidification process.

A. K. Dahle et al [71] measured the strength of the mushy zone. By analyzing the relationship trend between strength and fraction solid, a hot tearing criterion was proposed. The results indicated that the rigid dendrite network is established at the maximum packing fraction solid instead at dendrite coherency point. The vulnerable area (see section 2.2.2.1) of the mushy zone, i.e. brittle interdendritic liquid film, begins there. In this stage, hot tearing may occur and is related to the morphological features of the microstructure and strain rate.

C. H. Dickhaus et al [36] simulated the solidification of a shell of Al alloys during continuous casting. They found that the low extension rates were combined with lower tensile strength (≈ 0.1 N/mm^2) and a higher elongation at fracture ($\approx$ 1%). According to them, when a separation occurs on the grain boundaries, the stress needed to cause fracture should be:

$$\sigma = \frac{2 \cdot \gamma}{h} \tag{2.17}$$

where, σ is the tensile strength, γ is the surface tension, and h is the liquid film thickness. The mechanical properties depend on the weakest point.

This relationship was extended by D. Lahaie and M. Bouchard [64] to develop a new mechanical fracture criterion for hot tearing. Assuming a DC casting semi-solid body submitted to a constant tensile strain rate $\dot{\varepsilon}$, and that the fracture surfaces of hot tears are intergranular, the fracture will initiate at the solid-liquid interface near the free surface of the ingot. They proposed that the initiated fracture stress σ_f depends on the fraction solid according to:

$$\sigma_f = \frac{4\gamma_{l/g}}{3h} * \frac{1}{\{1+[\frac{f_s^m}{1-f_s^m}]\varepsilon\}} \tag{2.18}$$

Where, $\gamma_{l/g}$ is the surface energy of the liquid/gas, ε the total strain, f_s the fraction solid and m the grain type parameter, which is 1/2 for columnar and 1/3 for equiaxed grain, respectively.

If the accumulated stress in the body σ_i is greater than the fracture stress σ_f, hot tears may occur. This mechanical hot tearing criterion, now referred as LB criterion, has been incorporated into the microstructural model in this project. The details will be described and discussed in the next chapter.

2.2.2.4 Models evaluated with pressure drop

Some researchers [43, 44, 72, 73, 74, 75, 76, 77] proposed that the thermally induced shrinkage not only caused the formation of macrosegregation and porosity, it also affected the liquid pressure drop and generated hot tearing. Therefore its effect should be included in the modeling to predict hot tearing defects.

Rappaz et al [72, 73, 75] took into account the influence of the pressure drop associated with the solidification shrinkage and tensile deformation at the stage near the end of the mushy zone. The thermal stress caused deformation resulting in hot tearing during the liquid to solid process. What also related to hot tearing was the solidification shrinkage, which induced porosity in the mushy zone. Both led to a decrease of the pressure in the liquid. If this type of depression were become lower than a certain value, hot tearing could nucleate and propagate from an existed pore or air bubble. They therefore proposed a hot tearing criterion (referred to as RDG criterion thereafter), which is based on a mass balance performed over the liquid and solid phases. This model considers the interactions between the deformation of solid skeleton and the feeding ability of the interdendritic flow. A maximum pressure drop was calculated, influencing of the pressure drop contributions associated with deformation and shrinkage. If the pressure drop in the liquid at the roots of the dendrites is greater than a given cavitations pressure, hot tearing may initiate (see Figure 2.25).

Furthermore, the observations by SEM of hot tearing formation were made for aluminum and the succinonitrile-acetone (SCN-acetone) alloy [42, 43, 44]. By pulling apart columnar growing dendrites, it was found that hot tearing always occurs in grain boundaries at a higher level of fraction solid. It is directly nucleated within the interdendritic liquid or developed from pre-existing micro pores or air bubbles induced by solidification shrinkage.

. To determine the propagating condition of hot tearing based on RDG model, J. F. Grandfield et al [74] calculated the reaction from pressure that was created by a nucleated tear due to feeding, dissolved gas and capillary effects. The equiaxed structure was particularly discussed in their work.

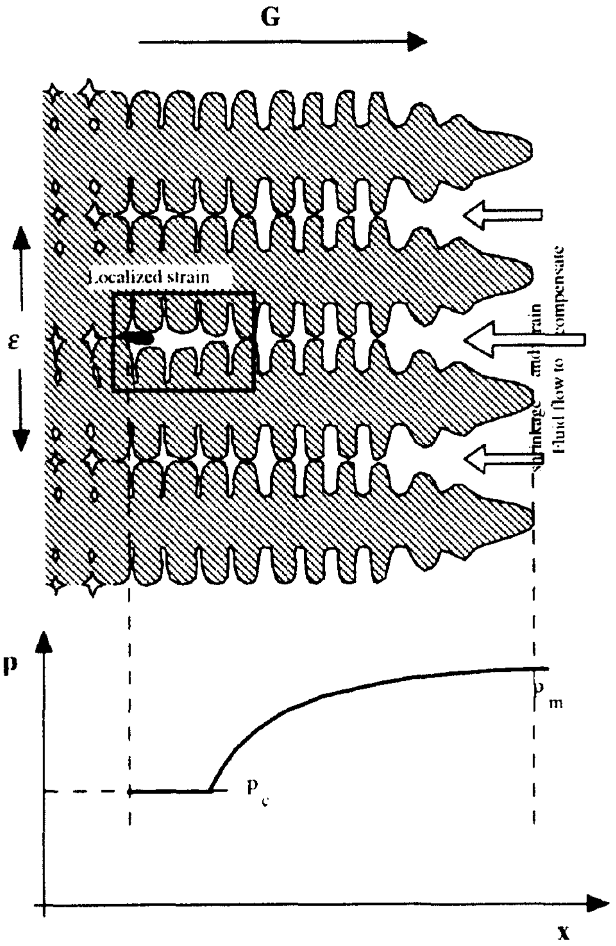

Figure 2.25 Schematically description of RDG criterion [72]

CHAPTER 3

DESCRIPTION OF MODEL

CHAPTER 3

DESCRIPTION OF MODEL

In this study, two hot tearing criteria were incorporated into a two-dimensional microstructure model in order to predict the hot tearing tendency for aluminum alloys. An overview of the complete microstructure-hot tearing model is shown in Figure 3.1.

3.1 THE MICROSTRUCTURAL MODEL

The microstructure modelling is based on a microstructural model originally developed by X. Yang [78, 79]. The characteristics included in this model are: columnar growth, equiaxed growth, columnar to equiaxed transition and the fraction solid evolution. The modelling results were obtained by simulating these solidification processes. The goal of the microstructural model was to provide basic information and to establish a complex microstructure-hot tearing prediction model for the Direct-Chill Casting Surface Simulator (DCSS) [80].

3.1.1 Description

The geometrical form of the two-dimensional microstructural model is based on the specimen used in DCSS experiments that is shown in Figure 3.2.

The computational domain, which is a 90 x 100 mm rectangular area taken from the center layer of the specimen is shown in Figure 3.3. Similarly, the computational area for the aluminum cooling plate was taken from the center part that is in direct contact with the specimen during solidification (see Figure 3.4).

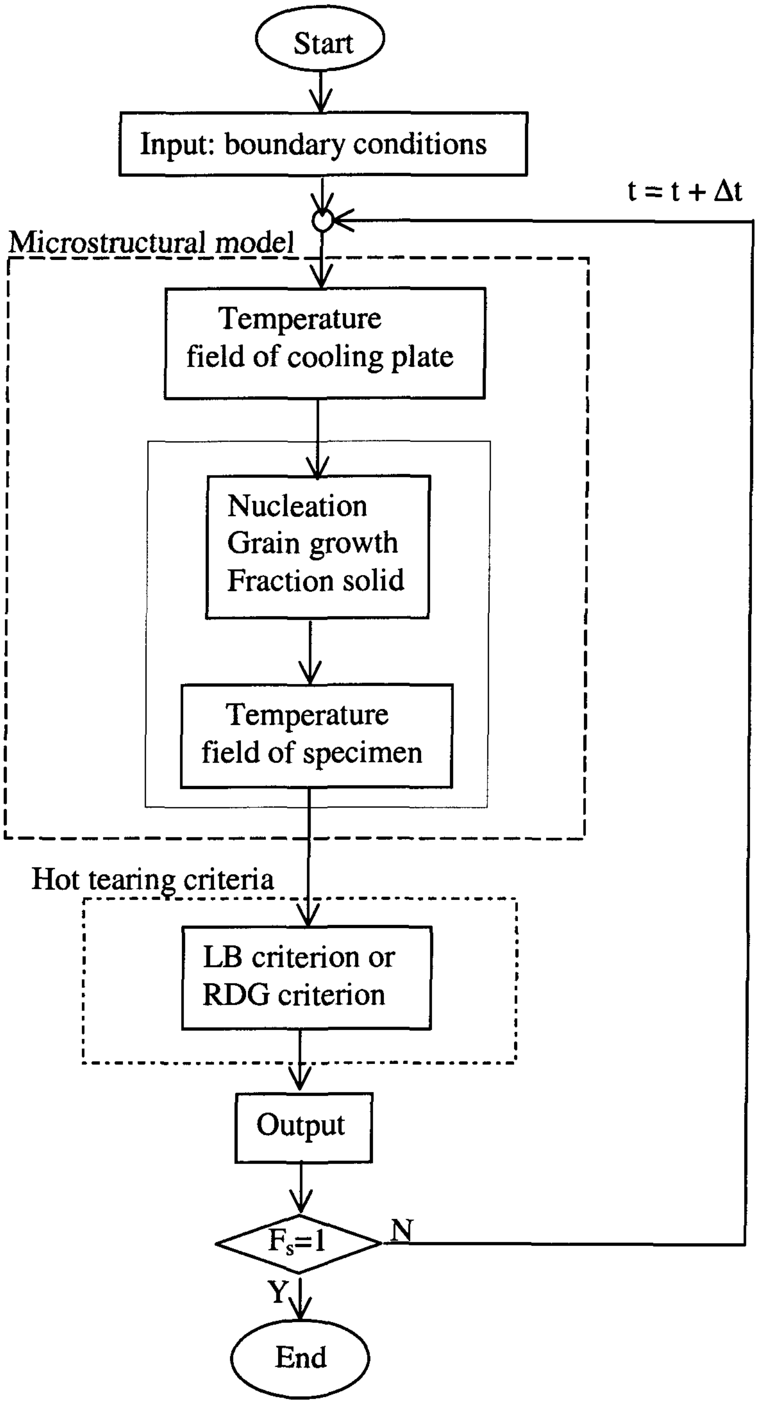

Figure 3.1 An overview of the complete microstructural-hot tearing model

Figure 3.2 The experimental specimen used in DCSS

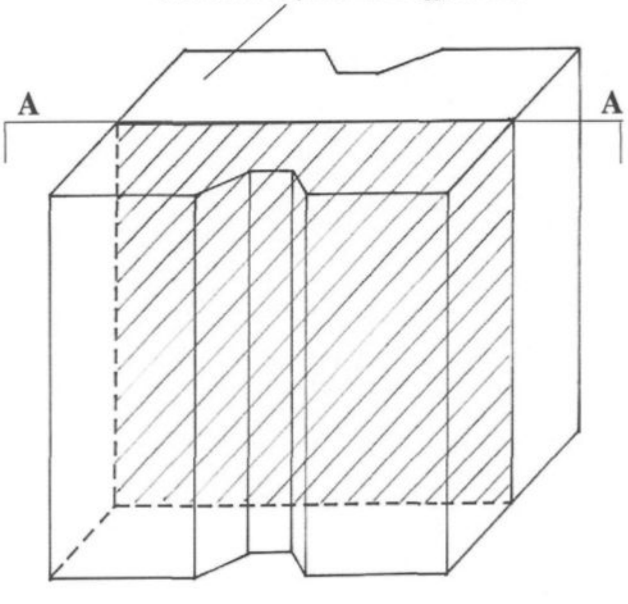
Chilled surface in contact with the water-cooled aluminum plate in Figure 3.4

Figure 3.3 Schematic description of the modeling area

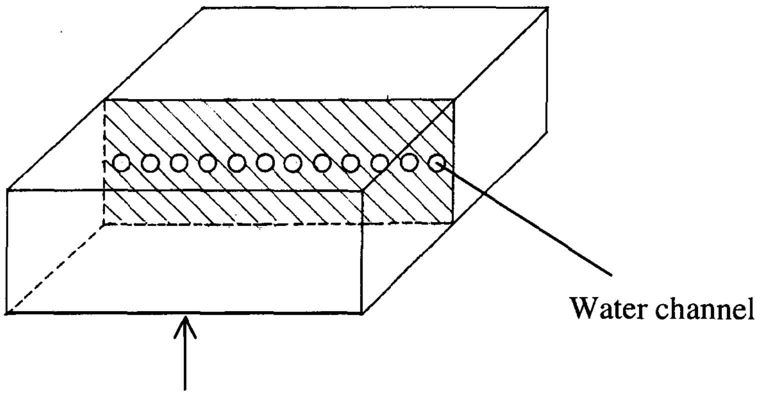

Figure 3.4 Schematic description of the water-cooled aluminum plate

3.1.2 The Modeling Assumptions

In order to develop a numerical simulation with actual casting conditions, the following assumptions were considered in the microstructural model to simplify the calculation:

- The heat extraction on the cooling side is uniform during the solidification process;
- The calculation begins from the melt cooling down, therefore the effect of pouring turbulence and the natural convection is not included in the model;
- All the equiaxed nuclei are formed at the onset of solidification and are uniformly distributed in the liquid without any grains remelting. If

undercooling ΔT reaches the maximum value (recalescence point), the nucleation rate is considered to be at its maximum value at the same time;

- The new equiaxed grains grow as spheres, which are only randomly created at each time step Δt, that means $n(t)$ grains with mean radius $\bar{R}(t)$ at time t will become $n(t+\Delta t)$ with the mean radius $\bar{R}(t+\Delta t)$ after the time step Δt (see Figure 3.5).

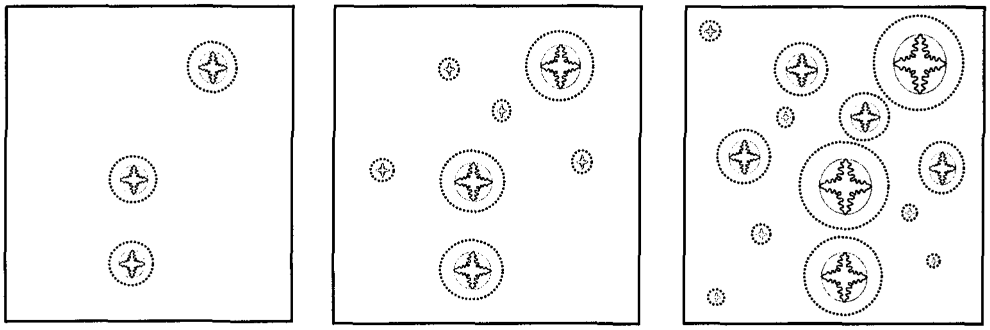
a) at time t-Δt
b) at time t
c) at time t+Δt

Figure 3.5 Description of the assumption for nucleation and grain growth in equiaxed structure

3.1.3 Numerical Simulation Procedure

3.1.3.1 Computational method

As Figure 3.6 shows, the computational areas of the specimen and cooling plate were further divided into 45 x 50 and 45 x 15 regularly spaced meshes, respectively. Finite volume centers were staggered with respect to the mesh point locations.

The physical model was then solved numerically using a fixed grid and explicit time stepping schemes with Finite Difference Method formulations in space and time. The continuous variables, such as the temperature distribution, the rate of nucleation, the growth velocity of the dendrite tip, the position of interface, and the evolution of fraction solid, were discretized for the equilibrium equations and calculated to provide the solidification conditions at each finite difference mesh point. All variables were evaluated at the control finite volume centers by using an explicit time dependent algorithm, as shown in Figure 3.7. The algorithm's code is written in FORTRAN and run with the software of the Microsoft Visual Fortran version 6.5.

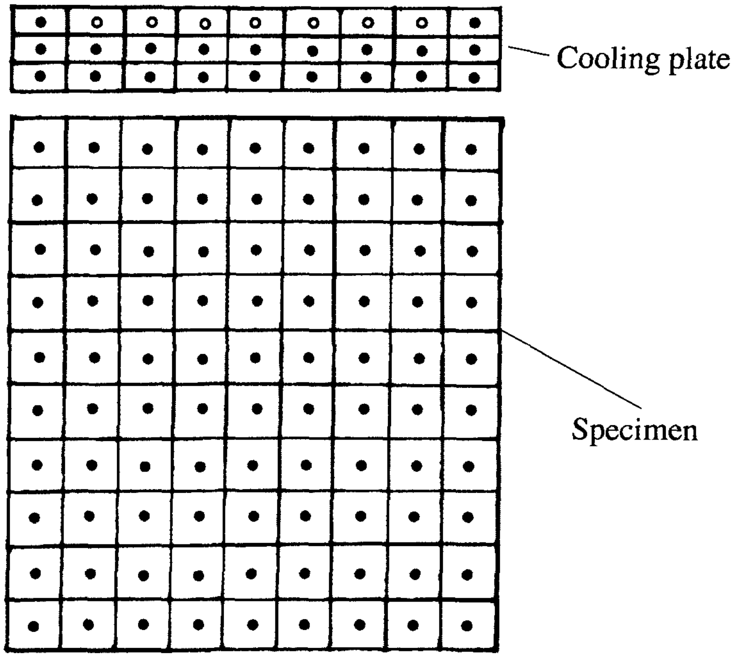

Figure 3.6 Description of the computational areas of the specimen and cooling plate

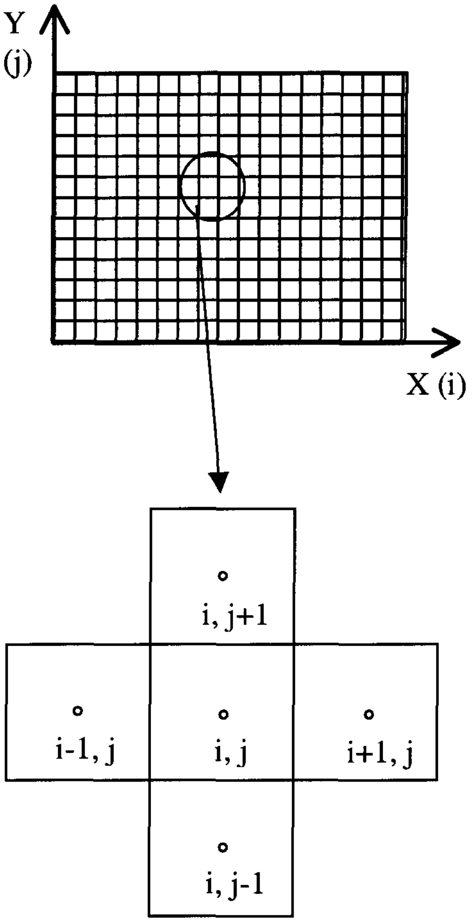

Figure 3.7 Schematic description of finite enmeshment of microstructure model

3.1.3.2 Boundary and initial conditions

The schematic view of the thermal boundary conditions is shown in Figure 3.8. One side of the specimen was contacted with a water-cooled aluminum plate, while the three other sides were adiabatic with insulating materials. The constant heat transfer coefficients between the specimen and its surrounding were imputed in the model. The heat transfer coefficient of the cooling plate side was chosen to obtain the better agreement between coefficient of the cooling plate side was chosen to obtain the better agreement between measured and calculated temperature field. Moreover a zero heat transfer boundary condition was applied to three insulated sides. By solving inverse matrix, the temperature profiles were deduced from location-dependent heat flow extracted at the cooling surface.

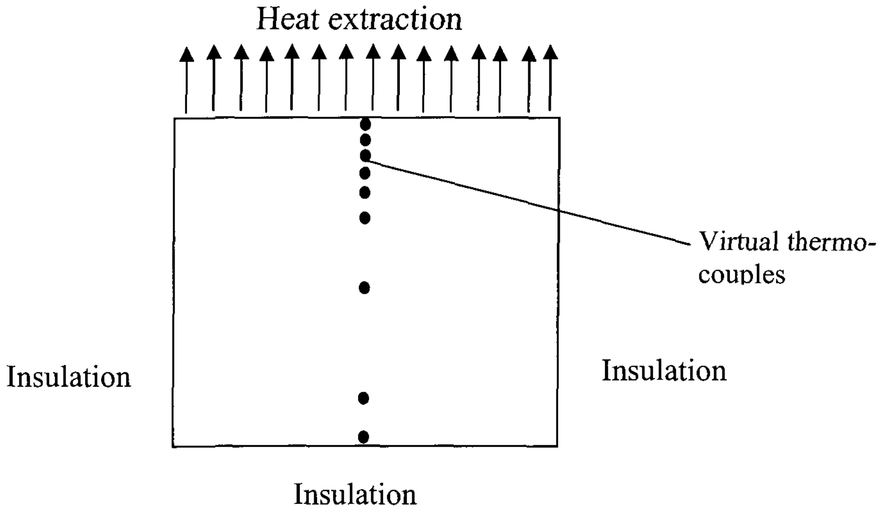

Figure 3.8 Description of the boundary conditions

In this study, the modeling was applied to the binary Al-4.5%Cu alloy. The values of the thermophysical properties and solidification parameters for Al-4.5%Cu alloy were provided in the Table 3.1 and 3.2, respectively.

Table 3.1 Thermophysical properties for Al-4.5%Cu alloy

Description	**Value**	**Reference**
Melt temperature of pure aluminum (T_m)	660.45 °C	
Temperature of liquidus (T_l)	645.24 °C	
Temperature of solidus (T_s)	571.85 °C	
Eutectic temperature (T_e)	548.2 °C	2, 81
Eutectic composition (C_e)	33.2 °C	2, 12, 80
Diffusion coefficient in liquid (D)	$3.0*10^{-9}$ m^2/s	2, 12, 82, 83
Density in liquid (ρ_l)	2537 kg/m^3	70
Density in solid (ρ_s)	2699 kg/m^3	
Effective specific heat in liquid (C_p)	955 J/kg*°C	2, 77, 82
Effective specific heat in solid (C_p)	1115 J/kg*°C	
Latent heat (L)	368 J/m^3	77
Thermal conductivity coefficient in liquid (κ_l)	95 W/K*m	82
Thermal conductivity coefficient in solid (κ_s)	150 W/K*m	81
Gibbs free energy (Γ)	$2.4*10^{-7}$ J/mol	2
Equilibrium partition coefficient (k)	0.17	2, 84
Slop of liquidus (m)	-3.38	

Table 3.2 Solidification parameters used in the model

Description	**Value**	**Reference**
Initial nucleation site density n_o	4.0×10^{11}	
Average nucleation undercooling dT_N	1.5 °C	84
Standard deviation of nucleation dT_σ	1.0 °C	

3.1.4 Governing Equations

The liquid and solid in the model are each treated as separate phases with their own conductivity, effective specific heat, location and concentration of species [79]. The temperature in each control volume is uniform.

3.1.4.1 Growth velocity of the dendrite tip

The model employs finite difference procedure. Assuming that the rate of advance of the dendrite tips is equal to the equilibrium liquidus isotherm. The growth velocity of a growing dendrite tip was determined by a local undercooling. When the undercooling of a liquid unit is greater than what is necessary for nucleation, the liquid unit changes from liquid to solid. The growth velocity of both columnar and equiaxed growth can be obtained from the diffusion equation and the marginal stability [79]:

$$V = \frac{\Delta T_0 k P_c^2 D}{\pi^2 \Gamma (1 - I(P_c) p)} \tag{3.1}$$

$$\Delta T_o = \frac{-mC_o(1-k)}{k} \tag{3.2}$$

$$P_c = \frac{RV}{2D} = \frac{R}{\delta_c} \tag{3.3}$$

Where:

V - growth velocity of dendrite tip, m/s;

ΔT_0 - difference between liquidus and solidus at C_0, °C;

k - distribution coefficient for a given alloy;

P_c - the solute Peclet number;

D - the diffusion coefficient in liquid, m^2/s;

Γ - the Gibbs-Thomson coefficient ;

p - a complemented distribution coefficient , $p=1-k$;

C_0 - initial alloy concentration;

R - the dendrite tip radius, m;

δ_c - solute boundary layer thickness in liquid

and $I(P_c)$ is the Ivansou function. Assuming that the dendrite tip always has a hemispherical shape, e.g. $I(P_c) = P_c = \Omega$, the dendrite tip growth velocity can be expressed by:

$$V = \frac{\Omega^2 D}{\pi^2 \Gamma} \cdot \frac{\Delta T_o k}{1 - \Omega(1-k)} \tag{3.4}$$

The supersaturation Ω of the liquid represents the diving force for solute diffusion at the dendrite tip in an alloy is related to the tip undercooling ΔT_o and the concentration undercooling ΔT_c:

$$\Omega = \frac{\Delta C}{\Delta C^*} = \frac{C_l^* - C_o}{C_l^*(1-k)} = \frac{C_l^* - C_o}{C_e p} \tag{3.5}$$

$$C_l^* = \frac{C_o}{1 - \Omega p} \tag{3.6}$$

where, ΔC and ΔC^* are the changes of solute concentration and the concentration at the solid/liquid interface respectively, C_e is eutectic concentration, T_l is the temperature of liquidus and T^* is the dendrite tip temperature.

From the definition we have:

$$\Delta T_c = T_l - T^* = \frac{\Omega}{1 - \Omega p} \Delta T_o k \tag{3.7}$$

Therefore Ω can be defined as:

$$\Omega = \frac{\Delta T_c}{\Delta T_c(1-k) + \Delta T_o k} \tag{3.8}$$

The dendrite tip radius is:

$$R_{tip} = \frac{2\Omega D}{V} \tag{3.9}$$

3.1.4.2 Evolution of fraction solid

The fraction solid characterizes the extent of solidification anywhere in the mushy zone. The influence of latent heat released during the solidification process is considered by calculating the change of fraction solid, which increases from zero to one when the metal becomes completely solid. It depends on the temperature and on the solidification kinetics, where involve different growth modes. As previously mentioned, fraction solid is a key term in microstructure modelling, which is first calculated to solve the heat balance equation to obtain the temperature distribution in each time step.

Level rule

To compare, the simple method to calculate fraction solid is to use the *Lever rule*:

$$f_s = \frac{T_l - T^*}{T_l - T_s} \tag{3.10}$$

where, T_l, T_s and T^* are the temperatures of liquidus, solid/liquid interface and solidus, respectively.

This is based on the hypothesis that the diffusion is rapid enough to give an almost uniform composition in the solid and in the liquid. The material parameters are assumed to be constant with the temperature.

Columnar growth

A theoretical relationship of velocity dependent dendrite tip undercooling and a columnar front tracking procedure were incorporated in the model of columnar growth. In columnar growth, solidification starts from the cooling surface and advances towards the center. In this modeling, the dendrite growth front was tracked while the control volume grids were kept fixed. The columnar dendrites front velocity was given in Equation 3.4. The front undercooling in each time step was calculated with the temperature field from the last time step. The faction solid was obtained from new temperature field and the front undercooling by using the truncated Scheil's Equation, which closely approximate the macroscopic freeing pattern of columnar structures:

$$f_s = 1 - \left(\frac{T_m - T^*}{T_m - T_l}\right)^{-\frac{1}{k-1}} \tag{3.11}$$

where, T_m and k are the melt temperature of alloy and the partition coefficient, respectively.

The derivation of the Scheil equation assumes complete mixing in the liquid and no diffusion in the solid.

Equiaxed growth

In equiaxed growth, solidification initiates from the nuclei in bulk liquid, and does not start at the cooling surface. The equiaxed structure modelling is complex, because the nucleation and growth of the grains occurs in the supercooled liquid, and the local fraction solid, as a function of time, will be dependent on the nucleation and growth characteristics, which are a function of undercooling.

a) Nucleation

The nucleation rate plays more important role in the final equiaxed-growth microstructure. In the microstructural model, the nucleation rate $\dot{n}(t)$ relies on undercooling and on the total number of nuclei. It can be calculated with the statistic nucleation distribution:

$$\dot{n} = \frac{dn}{dt} = \frac{n_0}{\sqrt{2\pi}\Delta T_\sigma}\exp\left[-\frac{(\Delta T - \Delta T_N)^2}{2(\Delta T_\sigma)^2}\right] \tag{3.12}$$

where, n_0 is the initial nucleation site density, ΔT_σ is the standard deviation of nucleation and ΔT_N is the average nucleation undercooling.

b) Dendrite growth

i) Calculation of mean grain size

Assuming $n(t)$ grains nucleated with mean radius $\bar{R}(t)$ at time t, after a time step Δt, the grain number becomes $n(t+\Delta t)$ and the mean radius becomes $\bar{R}(t+\Delta t)$:

$$n(t+\Delta t) = n(t) + \int_t^{t+\Delta t} \dot{n}(t)dt \tag{3.13}$$

$n(t)$ is the number of grains at time t;

$\overline{R}$ is mean grain size at time t, $\bar{R} = \frac{1}{n}\sum_{i=1}^{n} R_i$ and $\bar{R}^{\prime}$ is mean grain size at time $t+\Delta t$.

Supposing that all the grains created after a time step Δt (with the number being $\int_t^{t+\Delta t} \dot{n}(t)dt$) are nucleated at the start of the time step. The mean grain size changes from $\bar{R}(t)$ before nucleation to $\bar{R}'(t)$ after nucleation.

$$n(t+\Delta t)\,\bar{R}'^{3}(t) = n(t)\,\bar{R}^{3}(t)$$
$$or$$
$$\bar{R}'(t) = \sqrt[3]{\frac{n(t)}{n(t+\Delta t)}}\,\bar{R}(t) \tag{3.14}$$

ii) Calculation of fraction solid change

Unlikely using the tip velocity method for columnar dendrite growth, in which the fraction solid related to temperature by Scheil model, the equiaxed growth uses the volume averaged dendrite method. The dendrite tip growth velocity of equiaxed grains obtained was the same as that of columnar, but the fraction solid became related to the grain fraction f_g and to the internal fraction solid f_i, as shown in Figure 2.15. The equivalent dendrite volume in the sphere was in the same order as that of the solid dendrite.

Consider a unit volume element of uniform temperature $T(t)$ containing a solidifying melt. The growing equiaxed grain and its surrounding liquid was divided into three regions: solid (1), inter-dendrite liquid (2) and outside liquid (3) [15]. The standard fraction solid f_s was related to grain fraction f_g and internal fraction solid f_i as:

$$f_s = f_g f_i \tag{3.15}$$

and it derived:

$$\frac{df_s}{dt} = \frac{df_g}{dt} f_i + f_g \frac{df_i}{dt} \tag{3.16}$$

The f_i is a function of the supersaturation (Ω) and the Peclet number Pe_g. By assuming the grains grow as a spheroid, f_i is equal to 1 and $f_s = f_g$.

When the total grain number is n(t) and the mean grain size is $\bar{R}(t)$, then the volumetric grain fraction f_g is :

$$f_g = n(t)\frac{4}{3}\pi \bar{R}^3(t) \tag{3.17}$$

And from equation (3.15), we have:

$$\frac{df_s}{dt} = \frac{df_g}{dt} = n(t)4\pi \bar{R}^2(t)V(t) \tag{3.18}$$

where, $V(t) = \frac{d\bar{R}(t)}{dt}$ is the mean growth rate of the grains.

Columnar to equiaxed transition (CET)

It is essential that the model deals with mixed columnar/equiaxed structure. The columnar to equiaxed transition depends on the undercooled region, found between the columnar dendrite tips and liquidus isotherm. If the equiaxed nucleation undercooling is smaller than that of the columnar undercooling, and the undercooled region ahead of the columnar front is relatively large, then the equiaxed grains may have enough time to reach a sufficiently high volume fraction to block the advancing columnar dendrite, causing CET to take place.

The transition would depend on the combination effects of several factors, such as the undercooling, the dendrite growth rate, the thermal gradient, *etc.* In this model, solidification from the cooling surface and from nuclei in the bulk liquid are allowed. The local undercooling was a key condition in determining whether columnar or equiaxed growth could take place (especially at the very beginning of the solidification process). After each time step, the growth velocity of the columnar front was determined. The new radius of the equiaxed grains was then calculated, and the appropriate amount of latent heat release corresponding with the change in the volume fraction solid shared by all the sites ahead of the columnar front. This procedure was continued until the volume fraction of equiaxed grains, immediately ahead of columnar dendrite front, reached a value of approximately 0.49 (according to J. Hunt [7]), when the columnar growth was considered terminated. In the next equiaxed growth step, the grains growth was assumed to a volume fraction of 1.0 at the same location. Subsequently, the final structure is determined by the competition between the two growth modes.

Eutectic reaction

The liquidus temperature T_l decreases until reaches eutectic temperature T_e, when solute concentration, influenced by temperature and fraction solid, is increased. The fraction solid in eutectic reaction is determined by the truncated Scheil equation for either columnar growth or equiaxed growth. In this case, the eutectic volume fraction solid f_e can be written as:

$$f_e = 1 - f_s \tag{3.19}$$

3.1.4.3 Heat balance equation

Once the volume fraction solid was obtained from the micro-model calculation, the dynamic temperature distribution was acquired by combining the macro-model. Despite the convection effect, the thermal evaluation within the computation domain is solved by using heat-conduction equations:

$$\rho C_p \frac{\partial T}{\partial t} - div(\kappa \cdot gradT) = 0 \tag{3.20}$$

where, ρ is the density of alloy, κ is the thermal conductivity and T is the temperature field. C_p is the equivalent specific heat, which includes the latent heat that released during solidification [83, 85].

Considering the heat balance in each volume element as described in Figure 2.8 and Equation 2.7, the temperature change $\Delta T\{=T(t+\Delta t)\}$ in each volume unit at each time step Δt and temperature field at any time can be obtained by solving inversed conductivity matrix [***K***] [25]:

$$T=[K]^{-1}b \tag{3.21}$$

where, ***b*** is non-zero RHS terms vector coming from the boundary conditions, ***T*** is the matrix of nodal temperature, [k_{ij}] is the equivalent conductivity coefficient for an internal node.

3.1.5 Error Estimation

To keep the numerical solution stable, it was necessary to iterate the micro and macro model at each time step level, as much smaller time step was applied for both calculations. The iteration was continued until the maximum alteration in the temperature field was less than a prescribed value, or when a maximum number of iteration was reached. In this project, both were used and given as 0.5 x 10^{-6} and 200, respectively.

3.1.6 Numerical Procedure

The microstructural model was run to obtain a result at each time-step, and the interactions with an updating of the variables were calculated. The fraction solid did not change in the first macro iterations, so the calculated temperatures were used to estimate the fraction solid in the micro model. When the temperature cooled down below liquidus, the non-zero value of fraction solid would affect the new temperature field, until the pre-set tolerances were reached. An explicit integration scheme was used and the typical time step remained 0.1-0.25 seconds. At each time step and the mesh node, the variations of temperature, the volume fraction solid, and the average solute concentration in the liquid/solid interface were computed by a successive solution of the above equations. The resulting computation time was about 20 workstation-hours for a 2-D domain including 45 x 50 nodes for specimen, and 45 x 15 nodes for cooling plate. The flowchart of the model is shown in Figure 3.9.

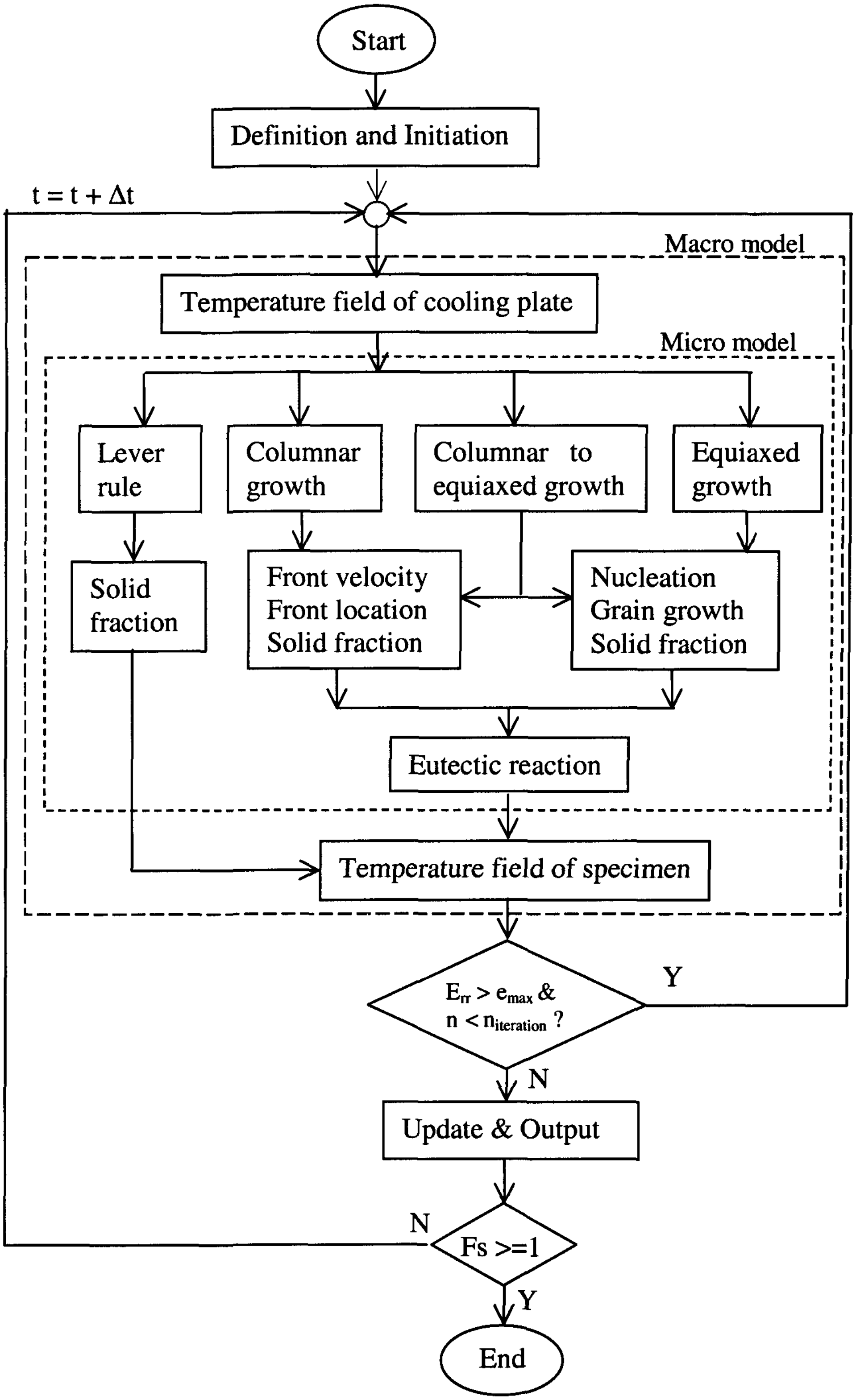

Figure 3.9 The flowchart of the microstructural model

3.2 HOT TEARING MODULES

Two hot tearing criteria, namely LB criterion and RDG criterion, were incorporated into the microstructural model. The critical conditions causing hot tearing, such as the location of hot spots, critical strain and stress, and the decisive pressure drop, were investigated by coupling the mechanical properties with the microstructural model. The calculated results, like temperature distribution, microstructure morphology, grain size, and the fraction solid change through mushy zone, were used to solve the relationship between stresses and strains that develops in the specimen during thermal contraction. The hot tearing modeling began at a relatively later stage of solidification when a considerable amount of solid had already formed in the mushy zone and the density of the metal was supposed to be constant. Furthermore, the liquid metal was assumed incompressible and the fluid motion is neglected. Figure 3.10 shows the flowchart of the coupled microstructural – hot tearing model.

3.2.1 LB Criterion Module

Since hot tearing mostly occurred in the shell zone of DC-Cast ingots [57, 80, 86], this criterion was employed to depict the hot tearing tendency in the region near the cooling surface.

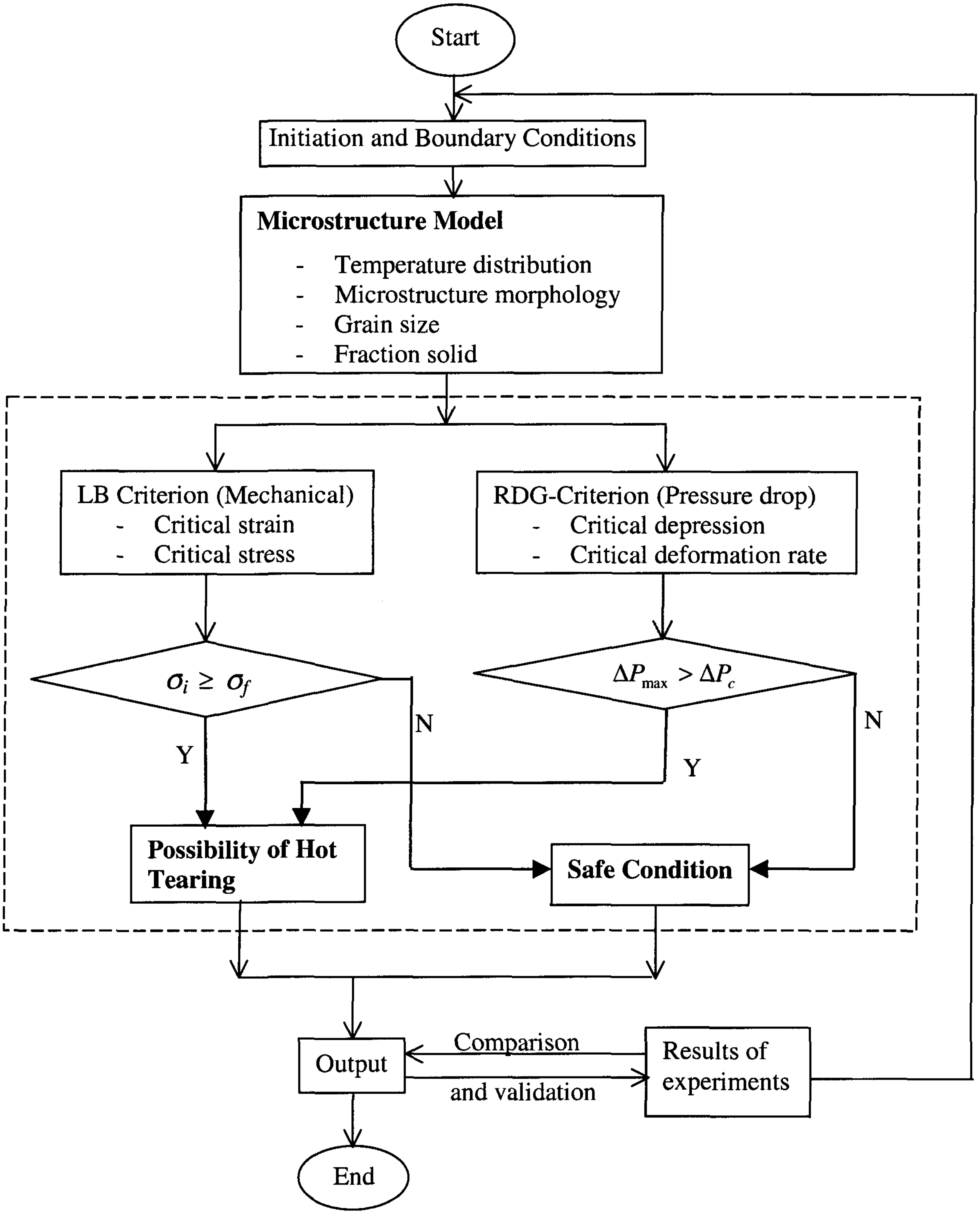

Figure 3.10 The flowchart of the complete microstructural - hot tearing model

3.2.1.1 Description

D. J. Lahaie and M. Bouchard modified and adapted an existing mechanical criterion for hot tearing of the semi-solid body to the deformation mechanisms [64]. As proposed by some researchers [40, 87], the solid grains of the semi-solid body in liquid film stage were idealized as an aggregate of regular hexagons for each grain, as shown in Figure 3.11. Assuming that the liquid and the solid grains in the later stage of solidification process are incompressible, the body will be thus subjected to a constant tensile strain rate $\dot{\varepsilon}$, if the feeding is not possible from outside to the liquid channel. Figure 3.12 shows the effect of the imposed deformation. The stress resisting deformation is thus a function of the total strain ε.

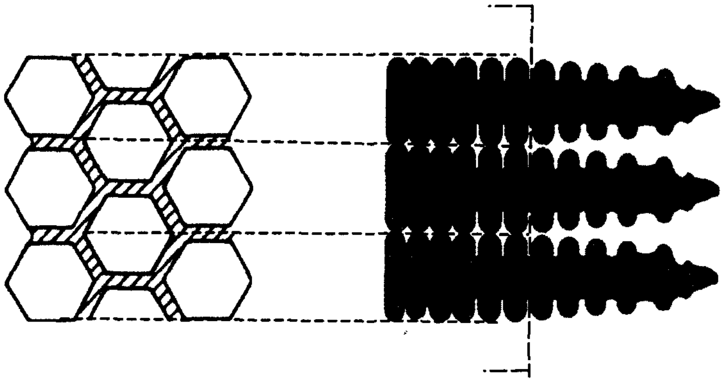

Figure 3.11 Schematic view of the idealized microstructure for a semi - solid and the constrained liquid film stage in later mushy zone

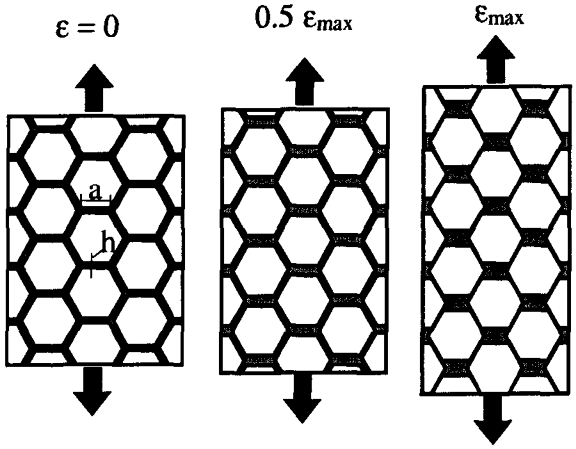

Figure 3.12 Schematic diagram of the deformation of a semi-solid body due to a constant applied strain rate, for various total strains [64]

3.2.1.2 Applied parameters

The parameters of the thermo-mechanical properties used to evaluate the tendency of hot tearing sensibility are shown in Table 3.3 (If not specific, all the parameters used are taken from reference [64]).

Table 3.3 The thermo-mechanical parameters used in the model

Description	**Value**
Viscosity of liquid metal (μ)	$1.0*10^{-3}$ (kg/m*s or Pa*s)
Strain rate ($\dot{\varepsilon}$)	$1.0*10^{-4}$ (1/s)
Surface energy ($\gamma_{l/g}$)	1.0 (J/m^2)
Isothermal compressibility (*Isoc*)	$4.13*10^{10}$ (Pa)
Limiting thickness on inclined channel (h_i)	$1.0*10^{-9}$ (m)
Initial liquid film thickness (h_o)	$4.8*10^{-7}$ (m)

3.2.1.3 Governing equations

Due to thermal concentration, the initiated and accumulated stress in the semi-solid body can be written as [64]:

$$\sigma = \frac{\mu\dot{\varepsilon}}{\sqrt{3}}\left(\frac{a}{h}\right)^3\left[\left(1-\left(\sqrt{3}/2\right)(a/h)\varepsilon\right)^{-3}+2\left(1+\sqrt{3}(a/h)\varepsilon\right)^{-3}\right] \tag{3.22}$$

Shown in Figure 3.13, in this constitutional law, *h* is the liquid film thickness before deformation and *a* is a side length of the hexagons, which can be replaced with grain size d:

$$a = (\pi^2/108)^{1/4} d \tag{3.23}$$

The relationship between *h* and *a* can be represented with fraction solid f_s as:

$$\frac{h}{a} = \sqrt{3}\left[\frac{1-f_s^m}{f_s^m}\right] \tag{3.24}$$

Therefore the constitutive expression of the internal generated stress in the body can be calculated as:

$$\sigma_i = \frac{\mu\dot{\varepsilon}}{9}\left[\frac{f_s^m}{1-f_s^m}\right]^3\left[\left[1-1/2\left[\frac{f_s^m}{1-f_s^m}\right]\varepsilon\right]^{-3}+2\left[1+\left[\frac{f_s^m}{1-f_s^m}\right]\varepsilon\right]^{-3}\right] \tag{3.25}$$

where, μ and $\dot{\varepsilon}$ are as shown in Table 3.1. *m* is the parameter of grain shape, which was ½ for columnar and 1/3 for equiaxed respectively [64].

Assuming that the semi-solid body of the specimen has a uniform tensile strain, and the hot tearing fracture surface is intergranular, the tear will initiate at the solid/liquid interface near the surface. Thus the fracture stress σ_f can be expressed as:

$$\sigma_f = \frac{4\gamma_{l/g}}{3h} * \frac{1}{\{1 + [\frac{f_s^m}{1 - f_s^m}]\varepsilon\}} \qquad (3.26)$$

where, $\gamma_{l/g}$ is the surface energy; ε is the total strain on the semi-solid body, and h is the film thickness. Wherever the internal stress σ_i is greater than the fracture stress σ_f, hot tears may occur.

3.2.1.4 Simulation procedure

This mechanical criterion was numerically simulated, based on the results from the microstructural model. The coherency temperature corresponds to a fraction solid was considered greater than 0.4 (depending on the chosen alloy), at which point the dendrites began to impinge upon each other and the stress generated by thermal contraction started to increase [72]. The microstructural parameters used in equation (3.23) to (3.25), such as fraction solid f_s, microstructure morphology m and grain size d were taken from the calculated results from microstructural model. Others, which kept constant during modeling, such as liquid viscosity, surface energy of liquid/gas and strain rate, were the same as those in reference [64].

Assuming that hot tearing primarily forms at the surface in DCSS cooling conditions, the initial stress in the semi-solid body (which had accumulated when strain was imposed to the specimen), and the fracture stress were calculated within the first 20 mm of the chill surface. In this zone, the grain sizes were about 100 – 200 μm for equiaxed structure (calculated by microstructural model) and 100 μm for columnar structure [64].

Combining the simulation of the solidification process and the stress/strain analysis of a solidifying specimen, the appropriate conditions for hot tearing development can be identified. Figure 3.13 shows the flowchart of this module for each time step and mesh.

3.2.2 RDG Criterion Module

In order to compare the different hot tearing mechanisms, another hot tearing criterion, from M. Rappaz, J. –M. Drezet and M. Gremaud [72, 73] was incorporated into the microstructural model. This criterion took both the solidification shrinkage and the thermal deformation into account as hot tearing behaviors.

3.2.2.1 Description

The RDG criterion calculates the pressure drop in the mushy zone due to shrinkage and the imposed thermal strain. When fraction solid reaches a certain value, the grains start to impinge on each other and begin forming a coherent network. As temperature continuous to decrease, the solid skeleton resistance to thermally induced deformation increases. It opens more easily as long as the network is still weak and the dendrite arms are still separated by liquid film when uniaxial tensile stresses are applied. At this point, the pressure in the dendrite decreases causing by solidification shrinkage and thermal deformation. If this depression exceeds a critical cavitation pressure P_c, hot tearing can initiate and propagate from an existing voids or air bubbles at the roots of the dendrites. Figure 3.14 shows a schematic formation and the interdendritic pressure change between columnar dendrites a), and equiaxed dendrites b), respectively.

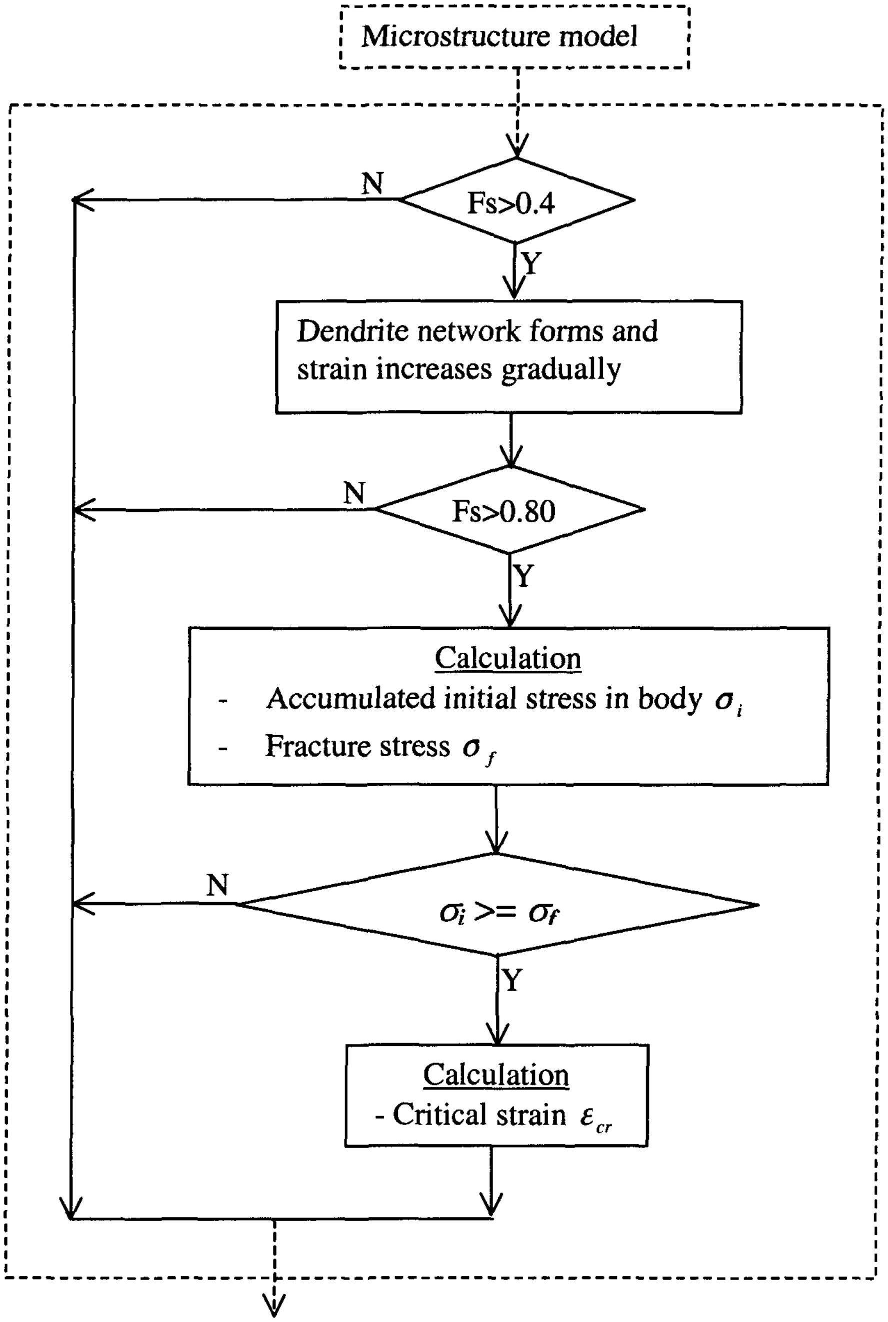

Figure 3.13 The flowchart of the module for LB criterion

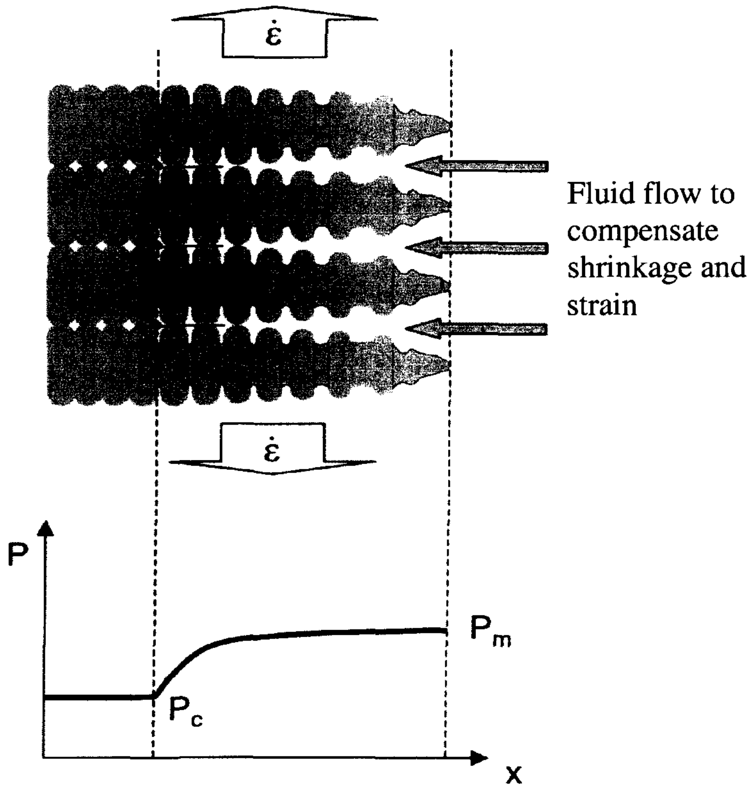

a) Depression in columnar structure

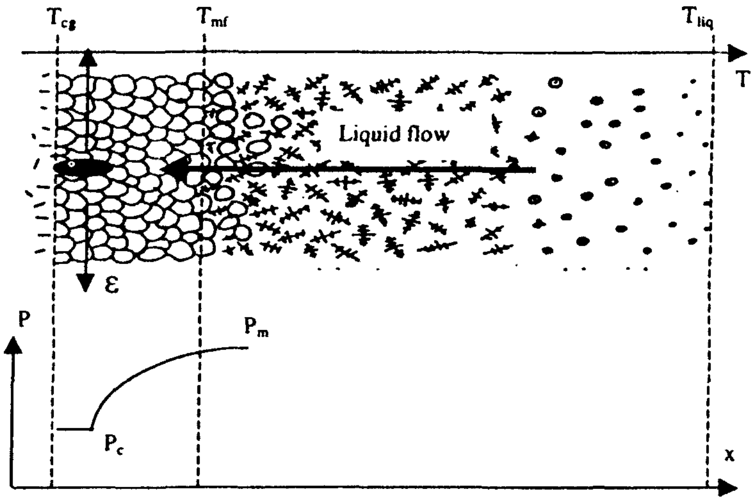

b) Depression in equiaxed structure

Figure 3.14 Schematic formation of hot tearing, proposed by Rappaz, Drezet and Gremaud [72, 73].

3.2.2.2 Applied parameters

The parameters of the thermo-mechanical properties used to evaluate the tendency for hot tearing sensibility in the RDG criterion module are shown in Table 3.4.

Table 3.4 The parameters of RDG hot tearing criterion [72]

Description	**Value**
Viscosity (μ)	10^{-3} (Pa*s)
Strain rate ($\dot{\varepsilon}$)	10^{-4} (1/s)
Velocity of the isotherms (v_T)*	10^{-4} (m/s)
Cavitation depression (dP_c)	2.0 *10^3 (Pa)
Shrinkage factor (β)	0.06

* Or calculated from microstructural model

3.2.2.3 Governing equations

The maximum pressure drop $\Delta P_{\max}$ is defined as the difference between the metallostatic pressure ΔP_m near the dendrite tips and the cavitations pressure ΔP_c:

$$\Delta P_{\max} = \Delta P_m - \Delta P_c \tag{3.27}$$

It can be described as the pressure drop caused by shrinkage ΔP_{sh} and deformation ΔP_{ε}:

$$\Delta P_{\max} = \Delta P_{sh} + \Delta P_{\varepsilon} \tag{3.28}$$

Where,

$$\Delta P_{sh} = v_T \beta\mu \int_0^L \frac{1-f_s}{k} dx \tag{3.29}$$

$$\Delta P_{\varepsilon} = (1+\beta)\mu\int_{0}^{L}\frac{E(x)}{k}dx \tag{3.30}$$

μ, v_T and β are shown in Table 3.4. $E(x)$ is the integral of deformation times the volume fraction solid between the solidifying tip and the dendrite root. K is the permeability, which was given by the Kozeny-Carman relationship:

$$E(x) = \int f_s \dot{\varepsilon}\, dx \tag{3.31}$$

$$k = C\cdot\frac{d^2\cdot(1-f_s)^3}{f_s^2} \tag{3.32}$$

where, C is a constant, and d is a characteristic dimension. For columnar structure, the liquid flow is interdendritic, so d is usually related to the primary or secondary dendrite arm spacing. On the other hand, liquid flow is often assumed to be intergranular in the equiaxed structure; d is therefore chosen the grain diameter or secondary dendrite arm spacing.

Equations 3.29 and 3.30 can be rewritten as the function of temperature:

$$\Delta P_{sh} = \frac{v_T\mu\beta}{G}\int_{T_s}^{T_l}\frac{(1-f_s)}{k}dT \tag{3.33}$$

$$\Delta P_{\varepsilon} = \frac{\Delta T(1+\beta)\mu\dot{\varepsilon}}{G}\int_{T_s}^{T_l}\frac{F(T)}{k}dT \tag{3.34}$$

G is thermal gradient and $F(T)$ is the cumulated deformation rate through the mushy zone.

$$F(T) = \frac{1}{G}\int_{T_s}^{T_l} f_s(T)dT \tag{3.35}$$

As shown in Figure 3.14, above the mass feeding temperature T_{mf}, the dendrite skeleton had already begun to develop, but the grains could still move freely. Below the temperature of coalescence T_{cg}, all the grains formed coherent solid network, which transmitted the thermal stresses induced by cooling. Both temperatures T_{mf} and T_{cg} were considered the same as in the LB criterion, when the local volume fraction solid reached 0.4 and 0.99 respectively.

From the microstructure modelling results, the fraction solid, the solidification front and root locations can be obtained at any time. The thermal gradient *G*, the secondary dendrite arm spacing, and the solidification time for each position can also be deduced. The secondary dendrite arm spacing λ_2 for equiaxed structure, and the primary dendrite arm spacing λ_1 for columnar structure in the permeability *K* calculation, are both provided by Equation 3.36 [12] and 3.37 [2], respectively:

$$\lambda_2 = 7.5 {t_f}^{0.39} \tag{3.36}$$

$$\lambda_1 = \frac{4.3 D^{0.25} \Gamma^{0.25} {dT_o}^{0.25}}{V^{0.25} G^{0.25} k^{0.25}} \tag{3.37}$$

For Equation 3.37, the Equation 3.32 is accordingly changed [74] to:

$$k = \frac{\lambda_1^2}{5000(1-f_s)(2f_s-1)} \tag{3.38}$$

The flowchart for the RDG criterion module is shown in Figure 3.15.

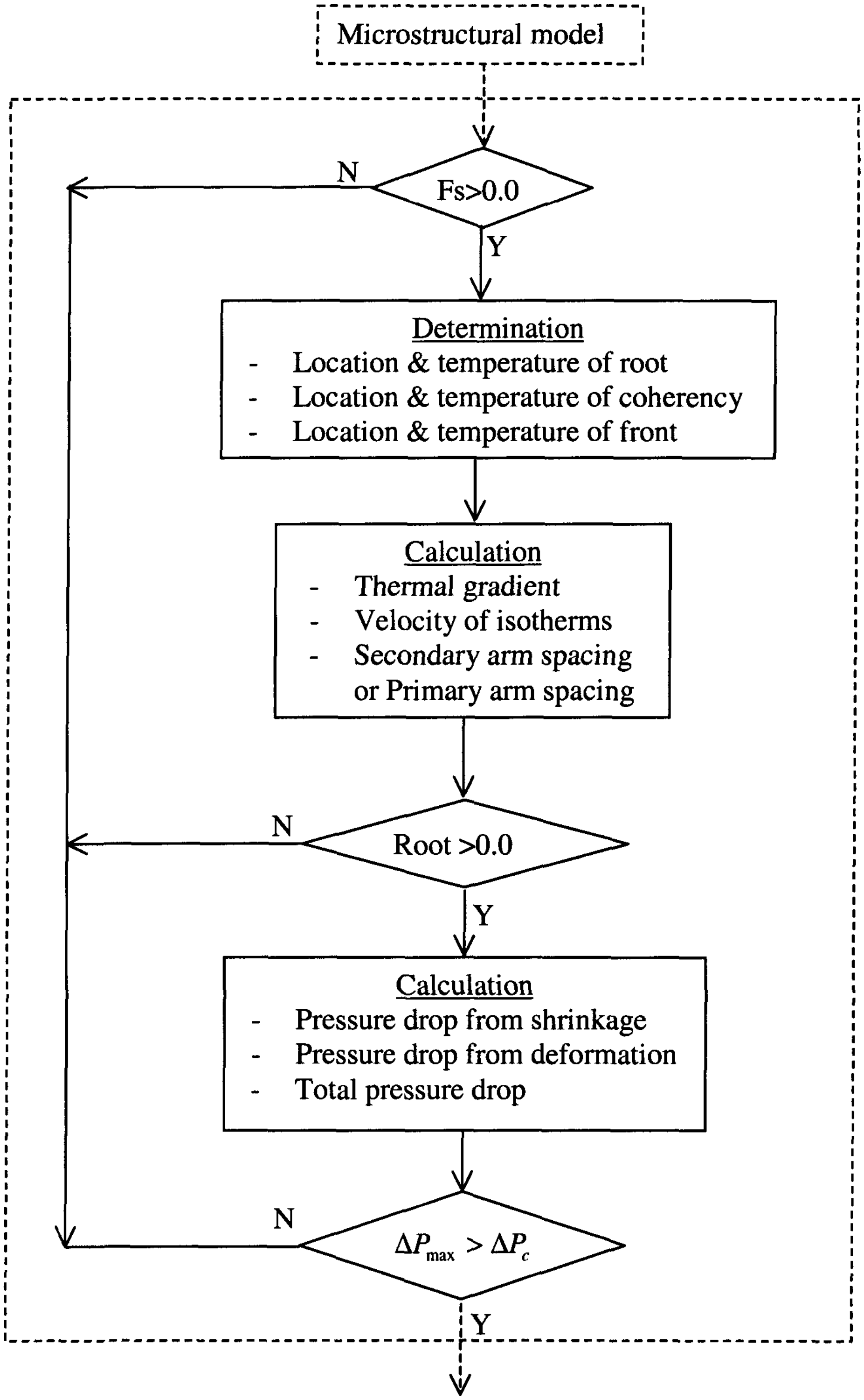

Figure 3.15 The flowchart of the DRG criterion module

CHAPTER 4

MODELLING RESULTS

CHAPTER 4

MODELLING RESULTS

4.1 MICROSTRUCTRAL MODEL

The numerical simulation of the microstructural model provides basic information, such as temperature distribution, microstructure morphology and fraction solid evolution through the mushy zone, which is essential to produce further simulation of hot tearing occurrences.

4.1.1 Temperature Distribution

The temperature distribution can be obtained at any time from the microstructural model as shown in Figure 4.1 (unless otherwise stated, all the modeling are based on Al-4.5%Cu alloy). As mentioned in section 3.1.4, the calculation of the temperature field is under four different modes: *Lever rule*, *Columnar growth*, *Equiaxed growth* and *Columnar to equiaxed growth* (see Figure 3.9), Figure 4.2 gives the cooling curves at 10 mm from the surface and at 50 mm from the center based on these modes. The results obtained from the modes are very similar, except for the *Lever rule*.

Since the cooling condition of the Direct-Chill Casting Surface Simulator is unidirectional from the surface towards the center, the cooling curve differences only depend on the heat transfer coefficient, corresponding to the boundary condition between the specimen surface and the cooling plate. Figure 4.3 illustrates the influence of the heat transfer coefficient on the cooling curves. All the curves are at the same location (10 mm below the surface), but are calculated by different growth modes, and using different heat transfer coefficients. The small heat transfer coefficient (400 W/m^2·K) represents the slow cooling condition and the large one (3000 W/m^2·K) reflects the fast cooling condition, respectively. Most of the simulations were carried out with the slow cooling condition, which is close to the experimental conditions of the DCSS specimens.

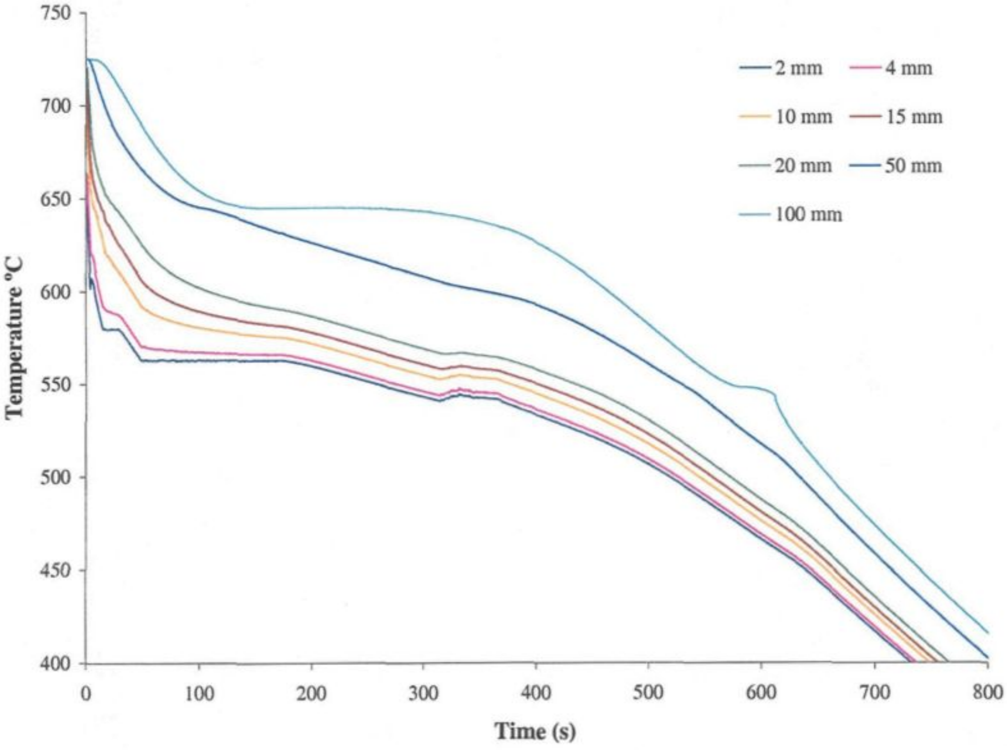

Figure 4.1 The temperature distribution against time at different locations from cooling surface calculated by the microstructural model

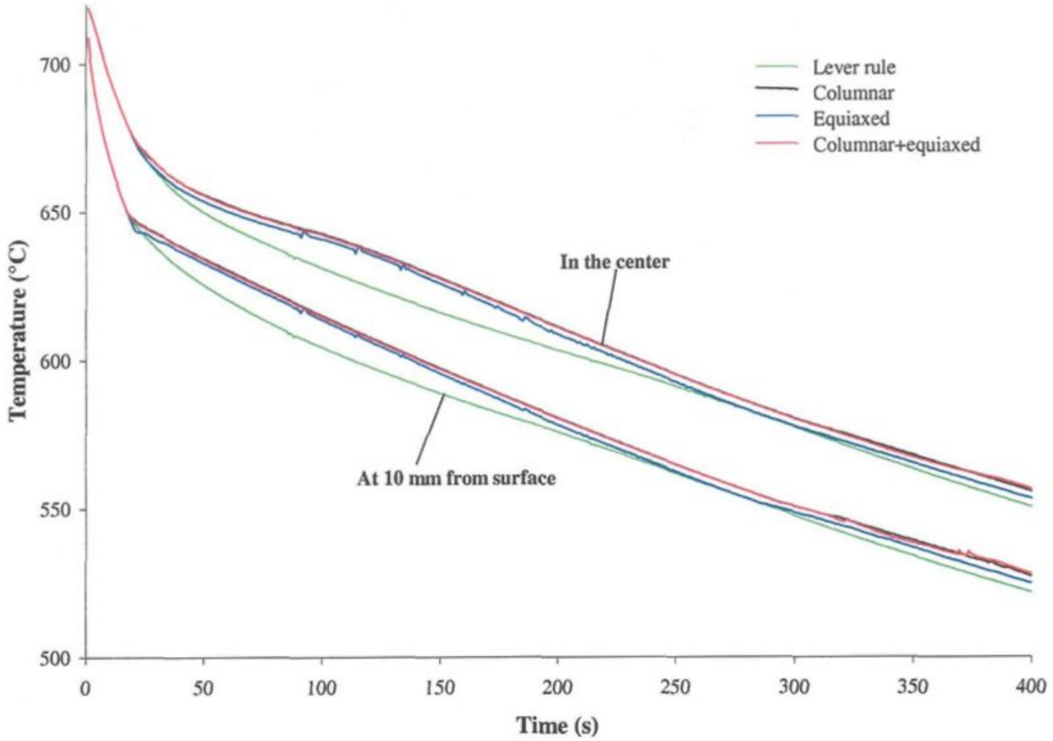

Figure 4.2 The temperature *vs.* time under different growth modes, HTC=400 W/m^2·K

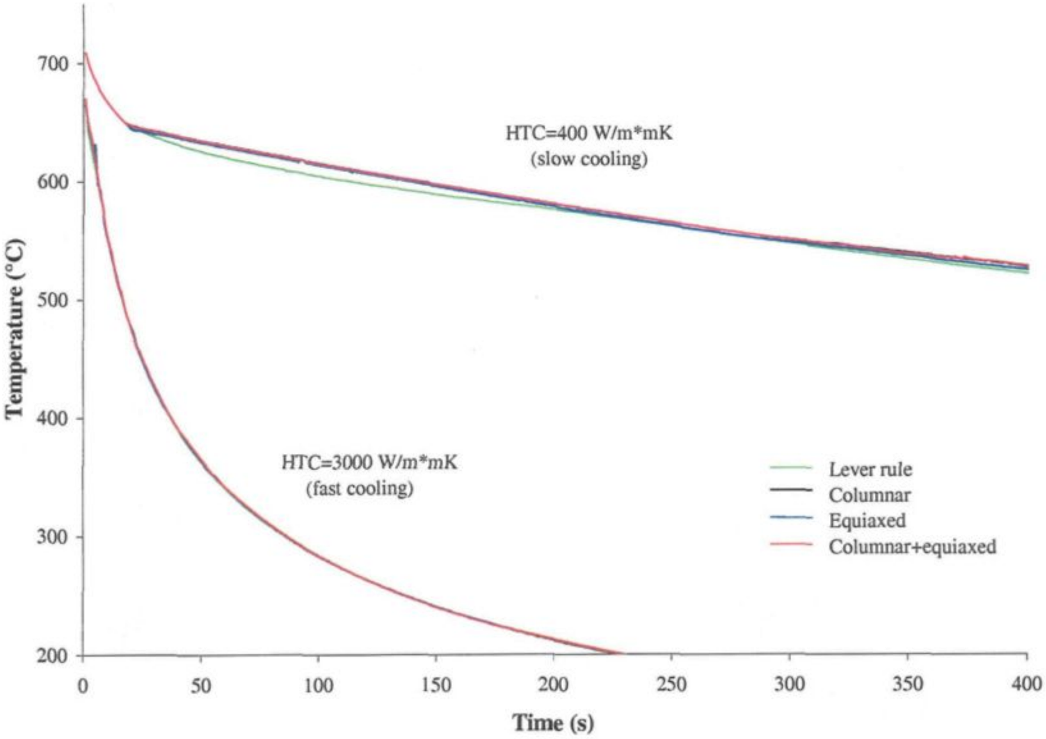

Figure 4.3 The influence of the heat transfer coefficient on the cooling curves, at 10 mm from the cooling surface

4.1.2 Fraction solid

To predict hot tearing, it is necessary to know the fraction solid. The microstructure model determines the increments of the volume fraction solid, liquid and solid concentrations evolutions during solidification. In the mushy zone, heat is released by the nucleating and growing solid. Hence a latent heat enthalpy formulation is used to evaluate the fraction solid versus temperature with respect to the computational mesh.

Based on different modes of calculation, the advance of fraction solid from the start to finish of each time step is shown in Figures 4.4 to 4.7. It indicated that within the first 4 mm from the cooling surface, the metal solidified very fast, regardless of which mode was used. The different dendrite growth modes were also distinguishable in this area. Over time, the solid fractions became linear at different positions by using the Lever rule. The development of fraction solid in columnar or equiaxed growth is different at the location near the cooling surface. The CET mode shows that near the cooling surface, the development of fraction solid is comparable to that of columnar growth. Towards the centre, the solid fractions are the same as those of equiaxed growth, which corresponds with the transition of microstructure in the specimen. It also shows that the solidification lasts relatively long under slow cooling conditions for all the modes. It took between 600 to 700 seconds before the body of the specimen was completely solidified.

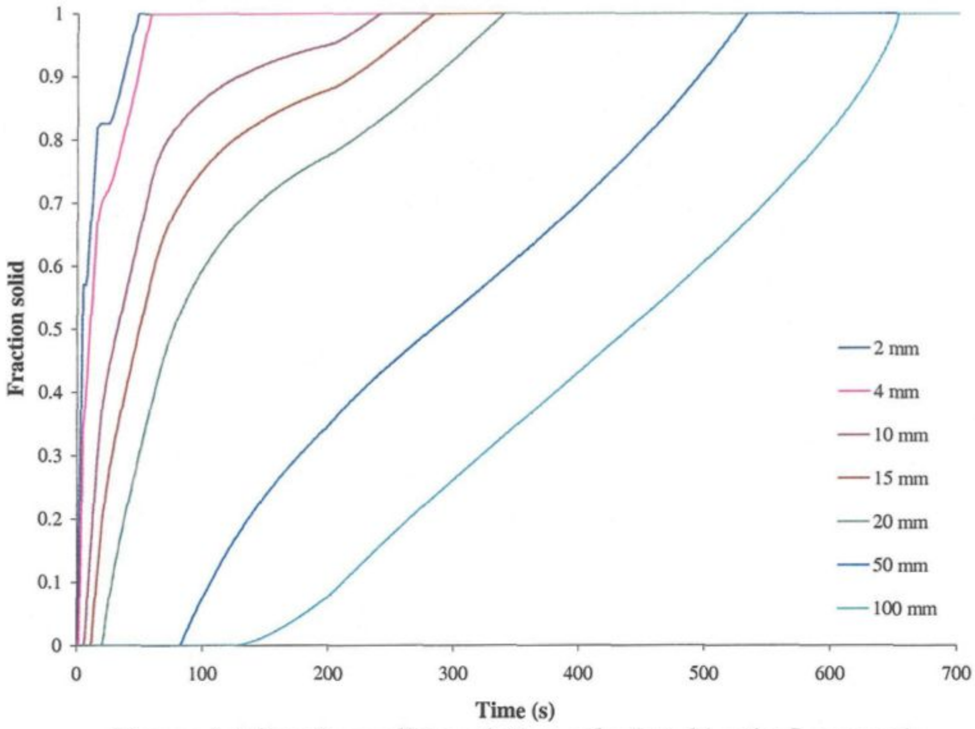

Figure 4.4 Fraction solid evolution calculated by the Lever rule

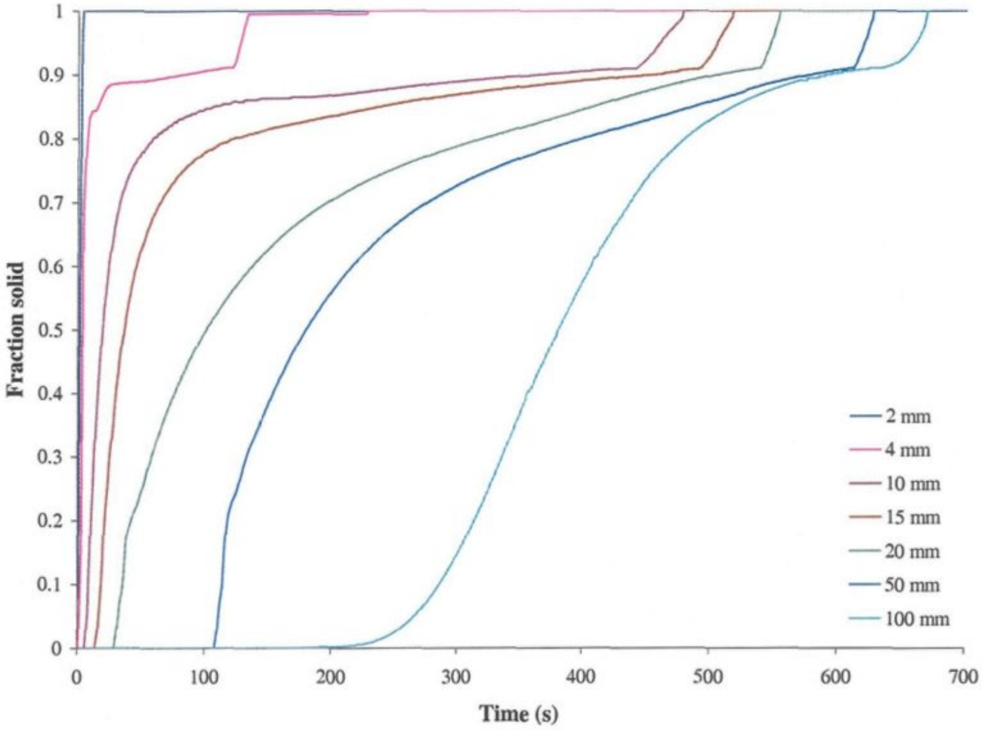

Figure 4.5 Fraction solid evolution calculated by columnar growth mode

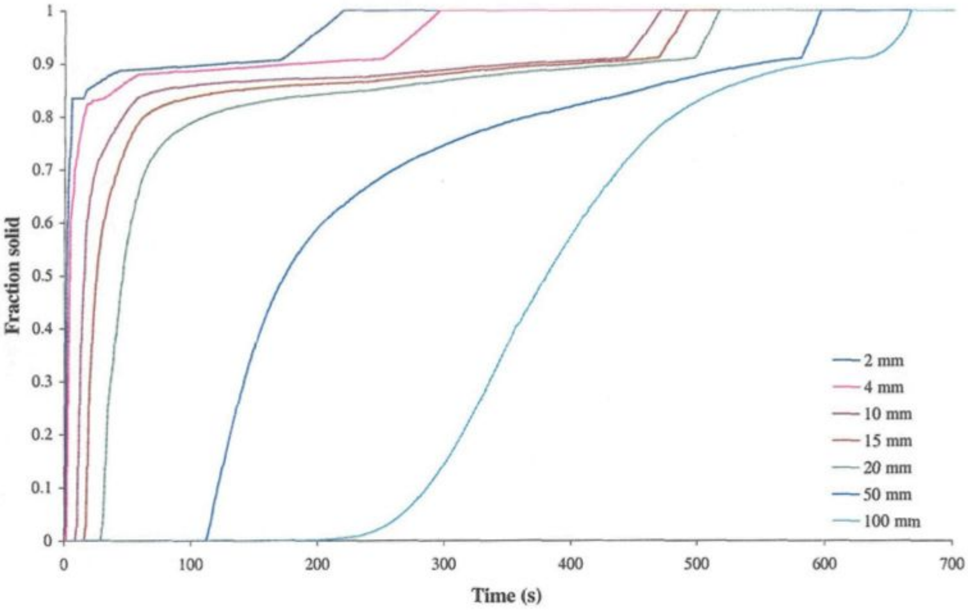

Figure 4.6 Fraction solid evolution calculated by equiaxed growth mode

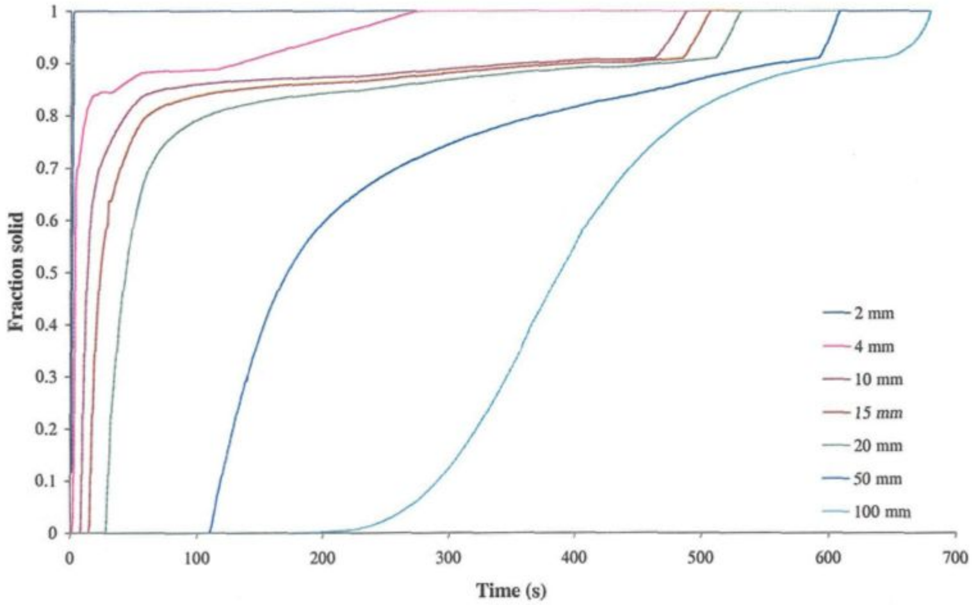

Figure 4.7 Fraction solid evolution calculated by CET growth mode

4.1.3 Temperature and Fraction Solid Profile

The temperature and fraction solid profiles were plotted against the distance from the cooling surface in Figures 4.8 and 4.9, respectively. Only twenty seconds after the solidification began, the surface region had already formed a dendritic network ($fs > 0.8$). After 700 seconds, the whole body of the specimen was completely solid.

4.1.4 Critical Solidification Range

As shown in Figure 4.10, the critical solidification range is defined as the interval, where the values of fraction solid are larger than 0.85 within the 4 mm from the cooling surface. This corresponds to a temperature ranging between 560 °C and 586 °C.

4.1.5 Microstructure Morphology

It is well known that the alloy's performance depends greatly on its microstructure. The evolution of microstructure during its solidification and final morphology can predict the properties of casting products. For a given alloy, its microstructure is affected by the cooling conditions. Figure 4.11 schematically represents the microstructures obtained under different cooling conditions, based on the columnar-to-equiaxed transit-growth mode. When the cooling rate was higher, the columnar grains dominated the microstructure. When the cooling rate was decreased, the proportion of equiaxed grains obviously enlarged. At a low cooling rate, the equiaxed grains dominated the microstructure.

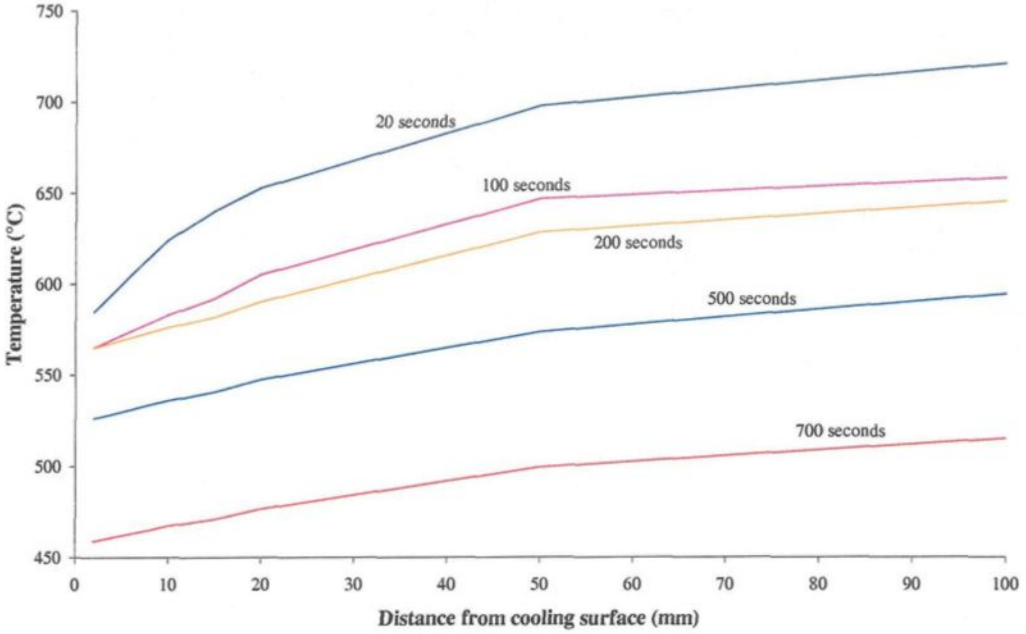

Figure 4.8 The temperature profile from the microstructural model

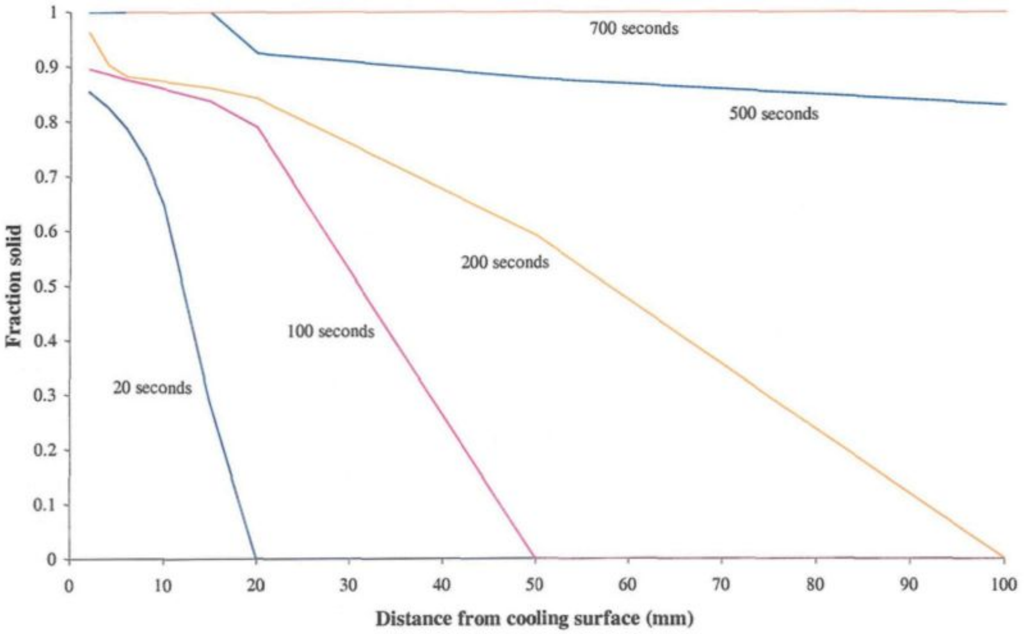

Figure 4.9 The fraction solid profile from the microstructural model

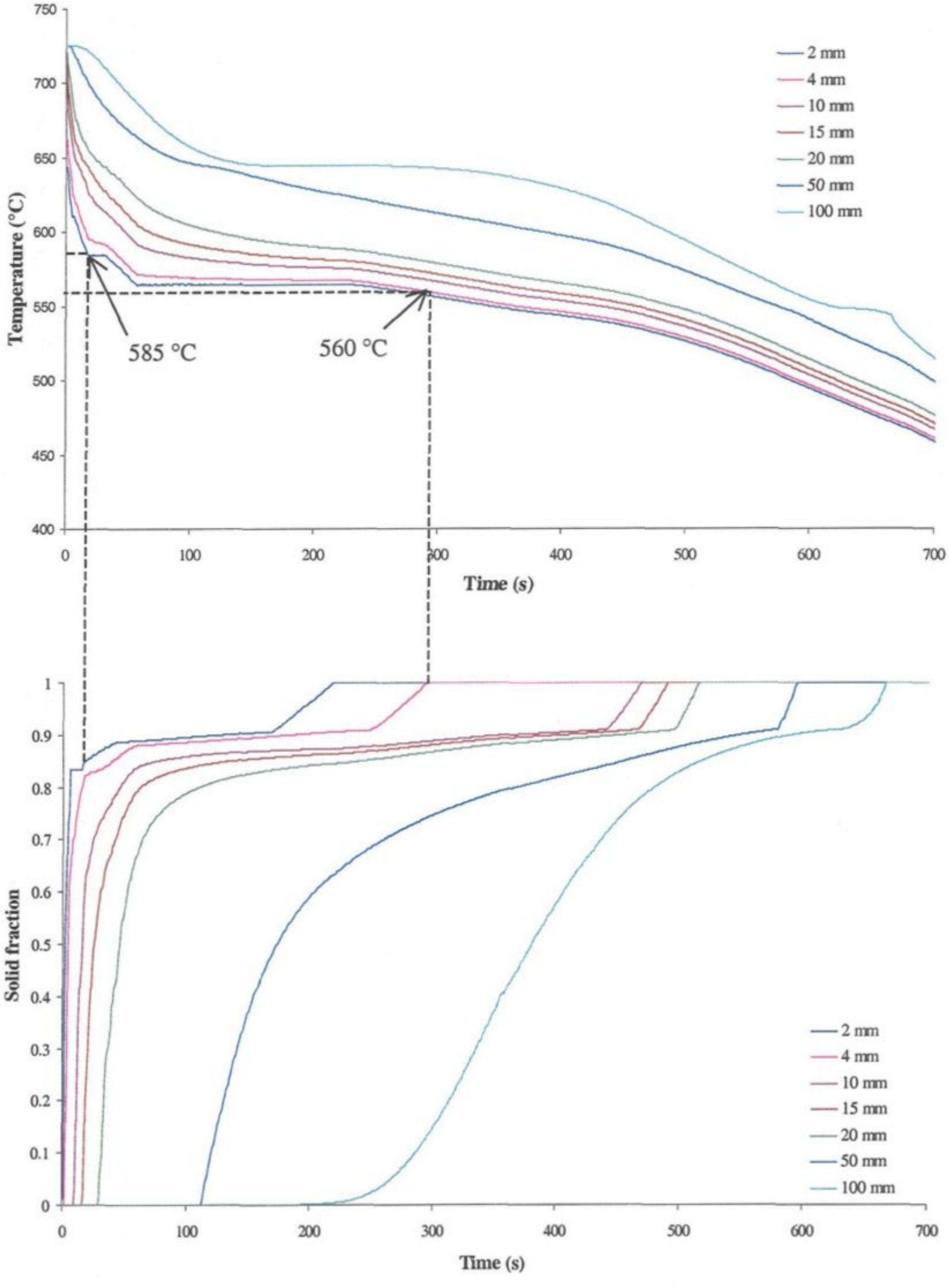

Figure 4.10 The critical solidification range for the distance within 4 mm from the cooling surface in equiaxed microstructure

```
Cooling surface (0 mm)          Center (50 mm)          End (100 mm)
**____**_________________________________________**********
**__*_**_________________________________________**********
**_______________________________________________**********
**____*__________________________________________**********
**____**_________________________________________**********
**____**_________________________________________**********
**____*_________________________________________***********
**__*_*__________________________________________**********
**_**_*__________________________________________**********
**_**_*__________________________________________**********
**_**_*__________________________________________**********
```

(a) higher cooling rate (average 4.9 °C/sec)

```
__________***___*******************************************
____********__*********************************************
___********__**********************************************
____********____*******************************************
____*******************************************************
____*********_*********************************************
____*******__**********************************************
______*****__**********************************************
____*******__**********************************************
____*******__**********************************************
______*****__**********************************************
```

(b) intermediate cooling rate (average 2.5 °C/sec)

```
_**********************************************************
_*_********************************************************
_**********************************************************
_**_*******************************************************
_**********************************************************
_**********************************************************
_**********************************************************
_**********************************************************
_**********************************************************
_**********************************************************
_**_*******************************************************
```

(c) lower cooling rate (average 1.1 °C/sec)

- columnar structure *equiaxed structure

Figure 4.11 Microstructures under influence of cooling condition: (a) columnar structure at a higher cooling rate, (b) columnar and equiaxed structures at an intermediate cooling rate and (c) equiaxed structure at a lower cooling rate.

4.2 HOT TEARING MODEL

To investigate how different conditions and mechanical properties influence the hot tearing tendency of binary aluminium alloys castings, two criteria, namely LB and RDG criteria, were added to the microstructural model (refer to Figure 3.10).

4.2.1 LB Criterion

As described in Chapter 3.2.1, this criterion concentrates on the mechanical response of the semi-solid body. A fracture stress and an accumulated initial stress in the semi-solid body are calculated separately under the same condition to find a critical point. This provides the critical strain reference indicating when and where hot tearing will occur.

4.2.1.1 Definition of critical strain ε_{cr}

Hot tearing appears when the semi-solid body cannot be compensated and cannot support the tensile stress induced by the thermal contraction. It loses its strength and ductility under a certain critical amount of strain [34-37].

The critical strain in this project was defined as a value that corresponds to the intersection of two linear body stress curve extensions (Figure 4.12). It shows that when the critical strain is reached, the stress in the semi-solid body rapidly exceeds the fracture stress, which is the maximum stress that the body can suffer.

Note that the hot tearing susceptibility, which is often referred in the literature, can be defined as an inverse of the critical strain.

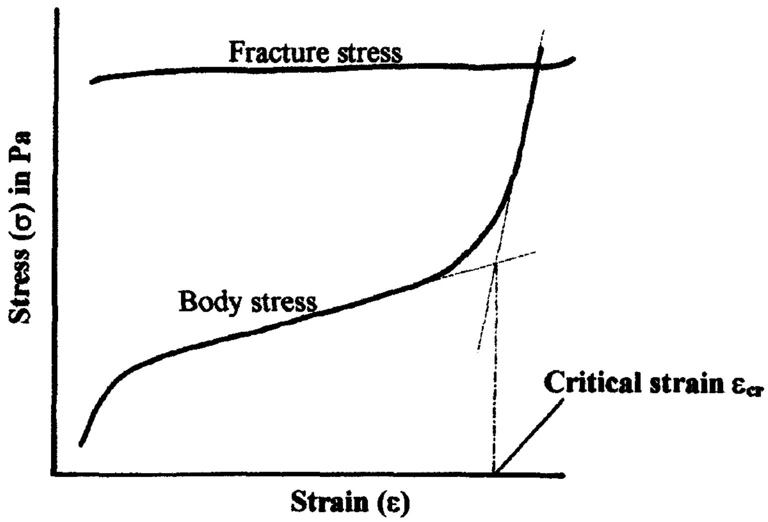

Figure 4.12 Schematic description of the definition of critical strain

4.2.1.2 Analysis results of LB criterion

For a general knowledge of LB criterion, Equations 3.25 and 3.26 were first statically analyzed, and the results were summarized in Figure 4.13. To calculate the accumulated body stress and fracture stress in these two equations, parameters such as strain rate, liquid viscosity, surface energy and grain shape, were kept fixed [64], while the fraction solid was gradually increased. It was obvious that the critical strain, which could mean the appearance of hot tearing, strongly depended on the fraction solid values. As the fraction solid varied from 0.85 to 0.99, the critical strain could overreach up to 100 times.

The strain rate influence was also investigated. Figure 4.14 shows the identical trend in the columnar and equiaxed structures. This means a higher strain rate will result in a higher fracture stress under the same critical strain when the fraction solid is increased from 0.85 to 0.99.

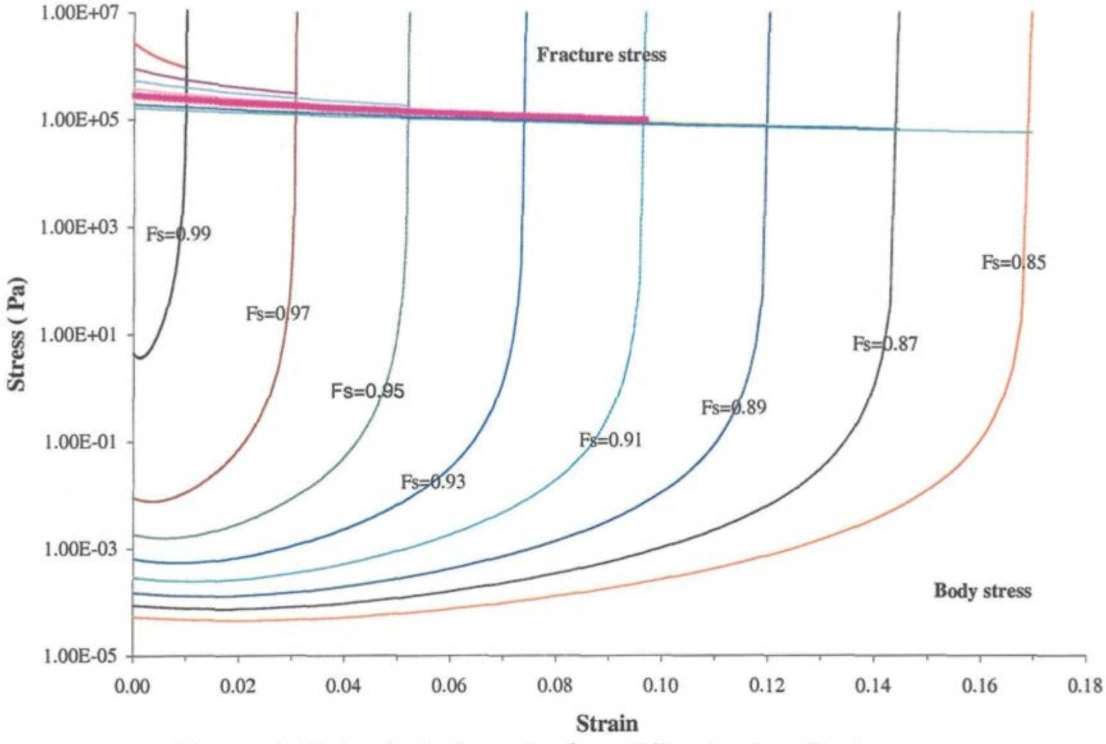

Figure 4.13 Analytical results from LB criterion. Body stresses and fracture stresses at given solid fractions in function of strains

4.2.1.3 Modeling results using LB criterion

Figure 4.15 shows a typical modelling result at different locations for Al-4.5%Cu alloy. The stress-strain curves in Figure 4.13 and 4.15 are based on the same equations; but in this modelling, the fraction solid is tightly subjected to the temperature and time of the DCSS specimen. These typical tensile stress-strain curves for a semi-solid body are identical with those from Fig.8 (in reference [64]). They were obtained by parameter testing, showing near zero strength for most of the deformation range, until suddenly increasing at the fracture point.

To find out the relationship between the forms of stress – strain curves and their influencing conditions, some features were investigated.

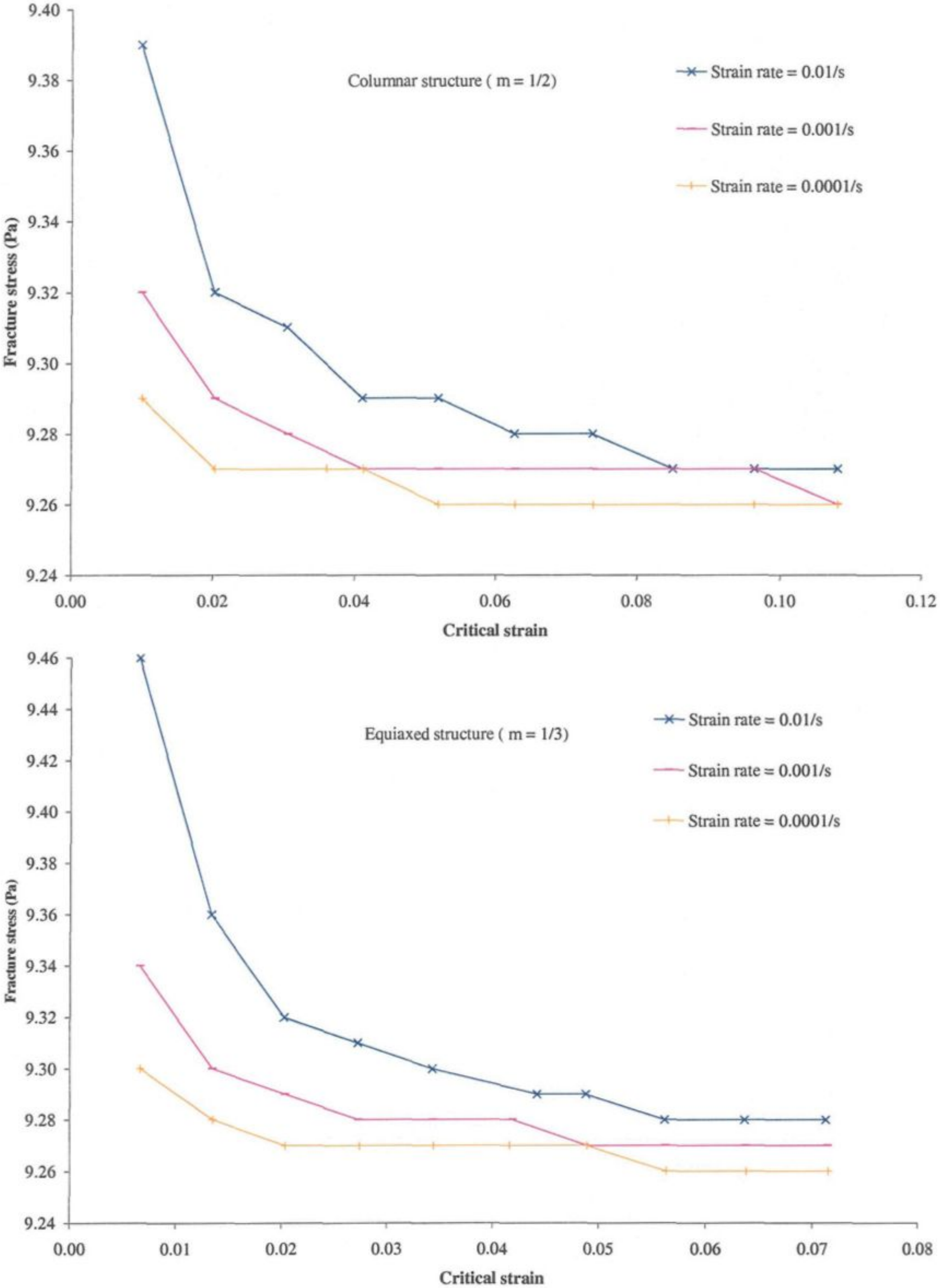

Figure 4.14 The influence of strain rate in different microstructures

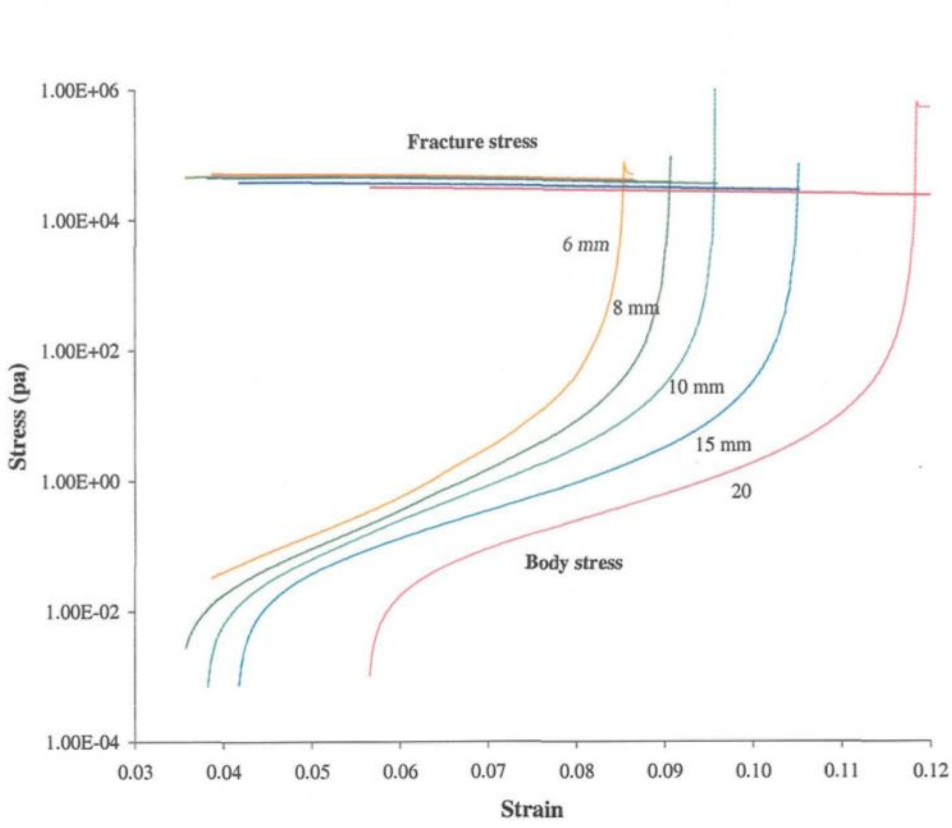

Figure 4.15 Numerical results. Body stress and fracture stress at different distances from the surface as function of strain. Parameters used for these calculations: strain rate = 10^{-3} s^{-1}, surface energy of liquid = 1 Jm^{-2} and viscosity = 1cP

i) Influence of strain rate

Figure 4.16 presents the stresses subjected to strain rates over time. It indicates that the body stress curves are strongly influenced by the strain rate. At lower strain rates, the accumulation of body stress takes a much longer time to reach the critical point, corresponding to the critical strain in the stress-strain curve. At higher strain rates, the body stress increases rapidly; then quickly passes the critical point to attain fracture stress. The critical point is not as clearly defined as it is at lower strain rates.

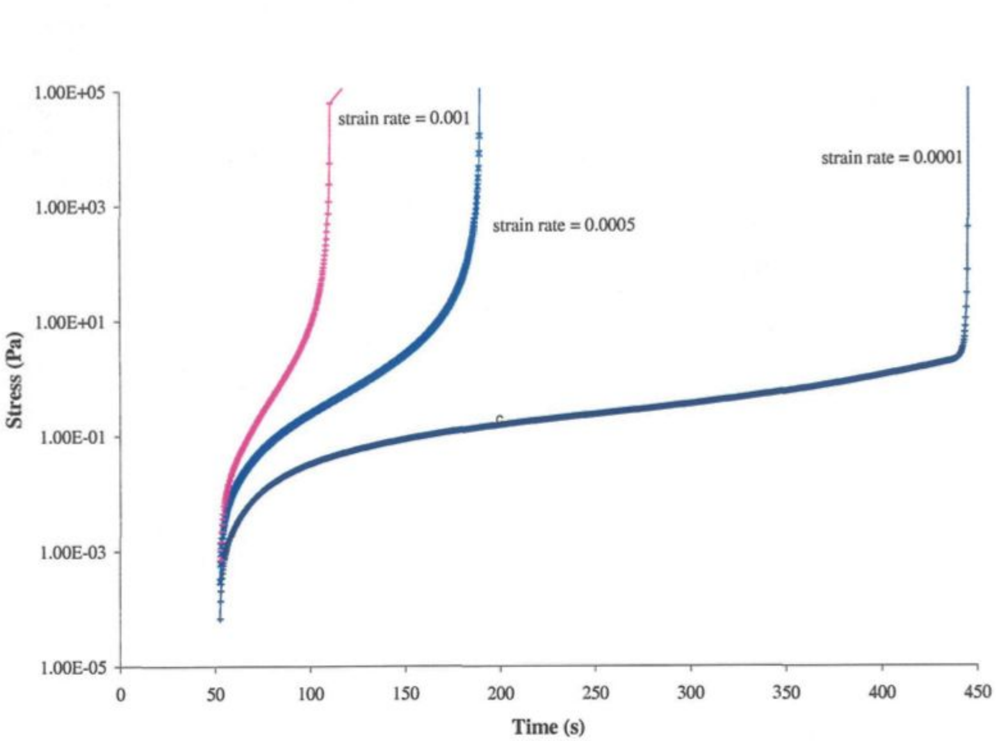

Figure 4.16 Influence of different strain rates for Al-4.5%Cu alloy

ii) Influence of cooling condition

According to the boundary conditions in the modelling, the cooling change depends only on the heat transfer coefficient of the cooling side. When varying the heat transfer coefficient, the fracture stress remains almost at the same level, but the critical strain changes a lot. The locations where stress-strain curves appeared are very different. Figure 4.17 indicates that the critical strain was much smaller at the higher cooling rate (A), than at the lower cooling rate (B); thus, the fracture stress was reached earlier in case (A). Figure 4.18 provides the corresponding cooling conditions for both cases, A and B.

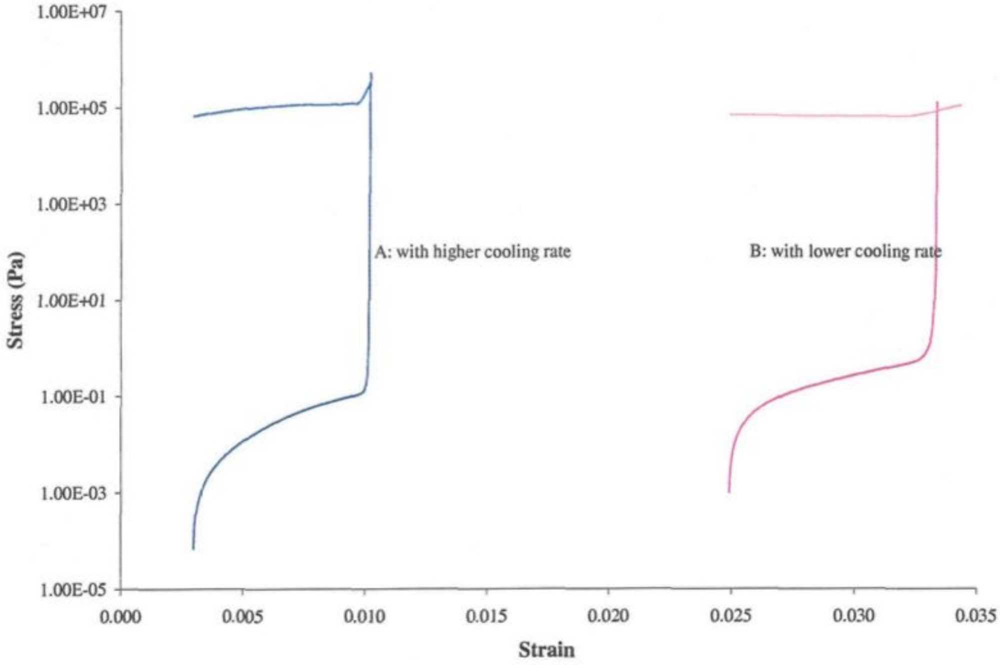

Figure 4.17 The influence of cooling condition

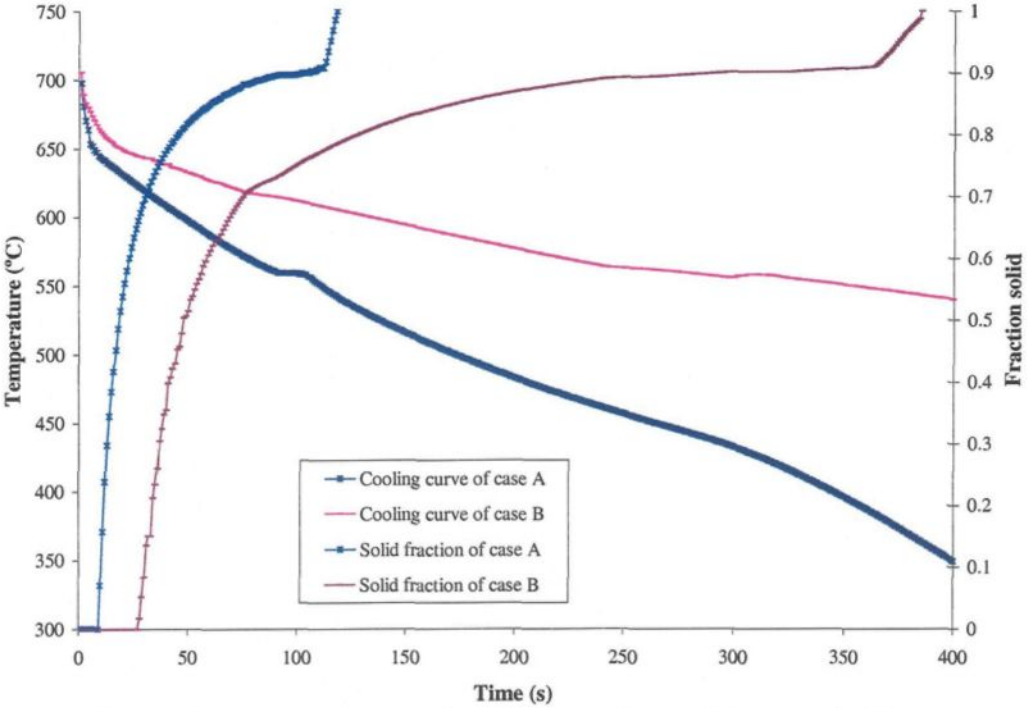

Figure 4.18 The correspond cooling conditions in Figure 4.17 The heat transfer coefficients of case A and B are 4250 W/m^2·K and 2500 W/m^2·K respectively

iii) Influence of microstructure

Because hot tearing is mainly initiated and developed in the mushy zone, it is very much related to the morphological features of the microstructure, which affects hot tearing even more than the alloy composition [45]. Figure 4.19 and 4.20 show the relationship between stress and strain under different microstructures. The strain reached the critical point much more quickly in an area dominated by columnar structure within 4 mm of the surface (Figure 4.20), whereas in equiaxed structure, the strain moved more slowly to attain the critical point at the same position. In both cases, the structures from 6mm and after were the same as those of equiaxed structures. This clearly shows that equiaxed structure is more resistant to hot tearing than columnar, which corroborates with our general knowledge.

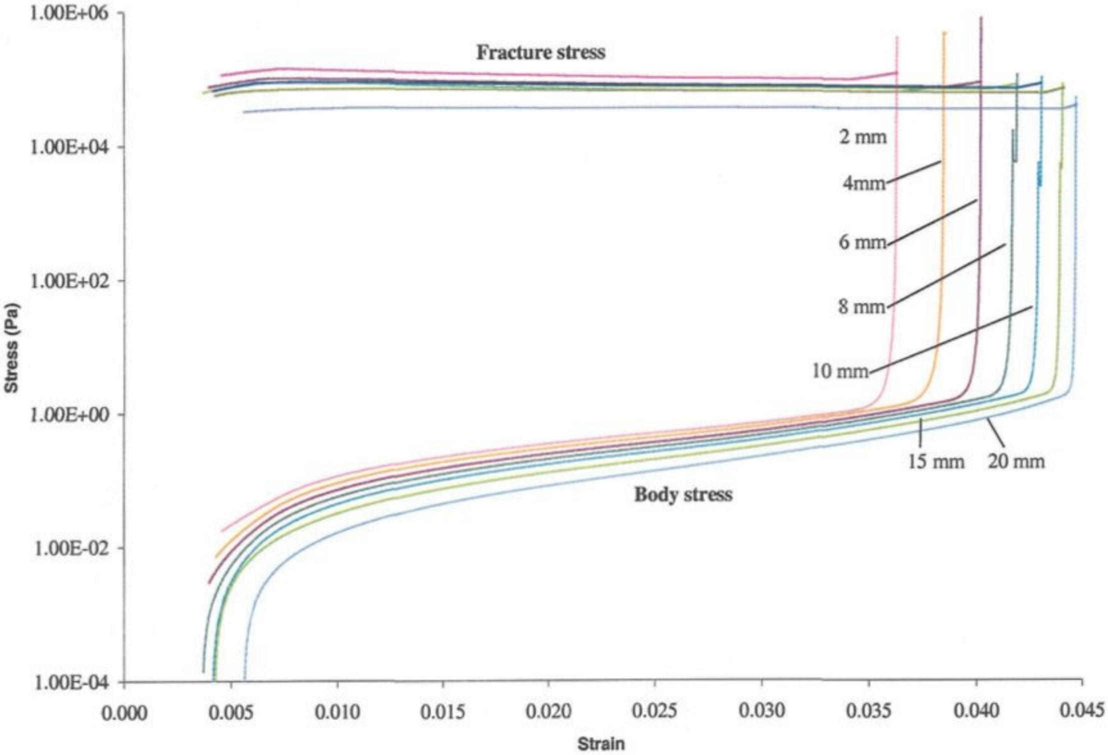

Figure 4.19 Modeling results for body stress and fracture stress at different distances from the surface as function of strain in a full equiaxed structure

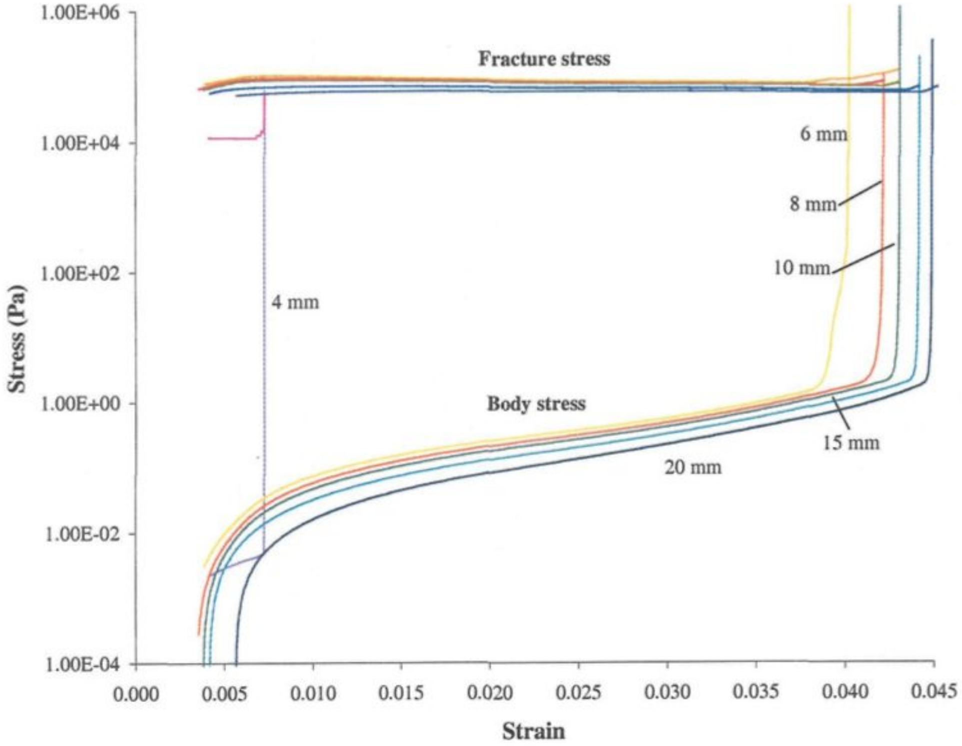

Figure 4.20 Modeling results for body stress and fracture stress at different distances from the surface as function of strain in the columnar to equiaxed transit structure, within 4-6 mm of the chill surface

iv) Influence of composition

The composition of alloy relates to its solidification interval, which is a hot-tearing cause factor [5]. Figures 4.21 to 4.23 provide the modelling results for different compositions of an A1-Cu binary system. The percentage of copper was varied, leading to different forms of stress-strain curves. Hot tearing susceptibility, also defined as the inverse of the critical strain, was plotted versus the copper content in Figure 4.24. The 1.4%Cu alloy was found to have a much greater hot tearing susceptibility than the other two alloys at the same distance from the cooling surface. This result seems agree to the results obtained by Campbell [5] and Rappaz [72], which were pointed out that the same composition gives a maximum solidification interval and the feeding difficulties.

4.2.1.4 Discussion of modelling results

The modelling results of the DCSS sample using LB criterion provide an overall hot tearing indicator. It shows whether hot tearing occurs when the body strain exceeds a critical value at a given time and location. The stress – strain curves of the solidifying body generally have the following features:

The stresses initiated in the semi-solid body accumulate slowly with the increased strain before attaining the critical strain;

Around this critical point, a slightly change of strain value makes a sharp increasing of the body stresses to exceed the fracture stress, which lead to hot tearing;

Under same conditions, the critical strains at the surface region are always smaller than those found at the center of the body.

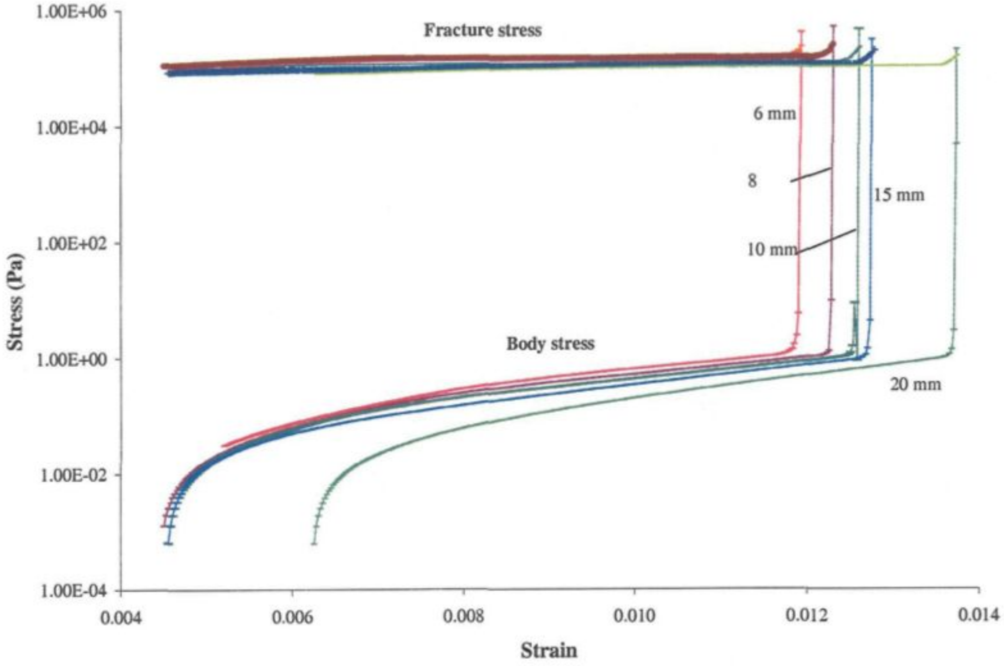

Figure 4.21 The stress – strain curve forAl-1.4%Cu alloy

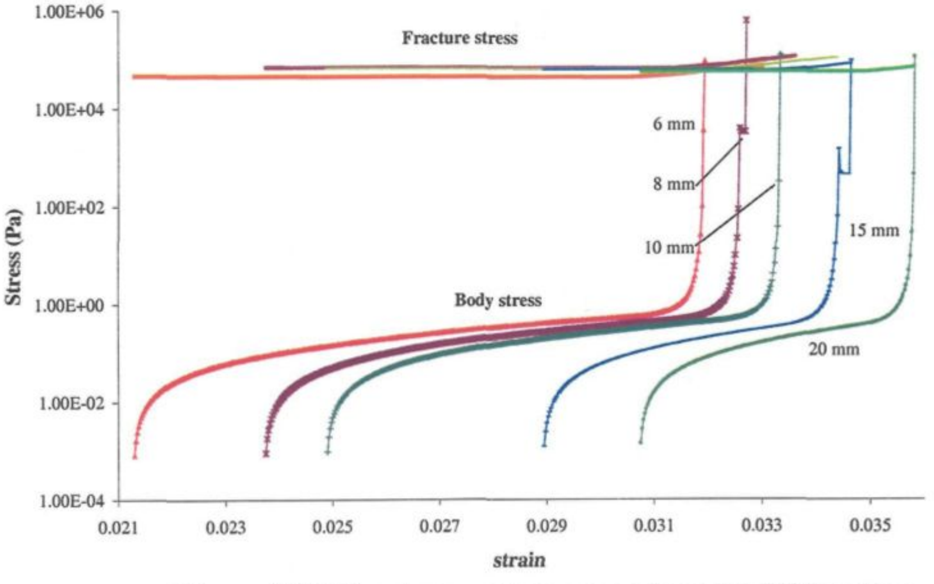

Figure 4.22 The stress- -strain curve for Al-4.5%Cu alloy

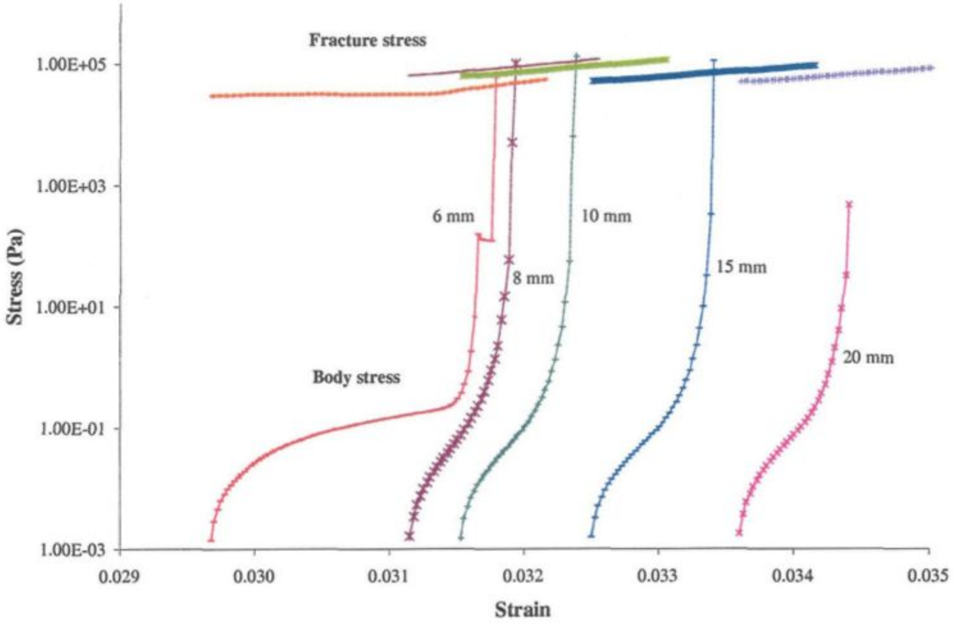

Figure 4.23 The stress – strain curve for Al-5.7%Cu alloy

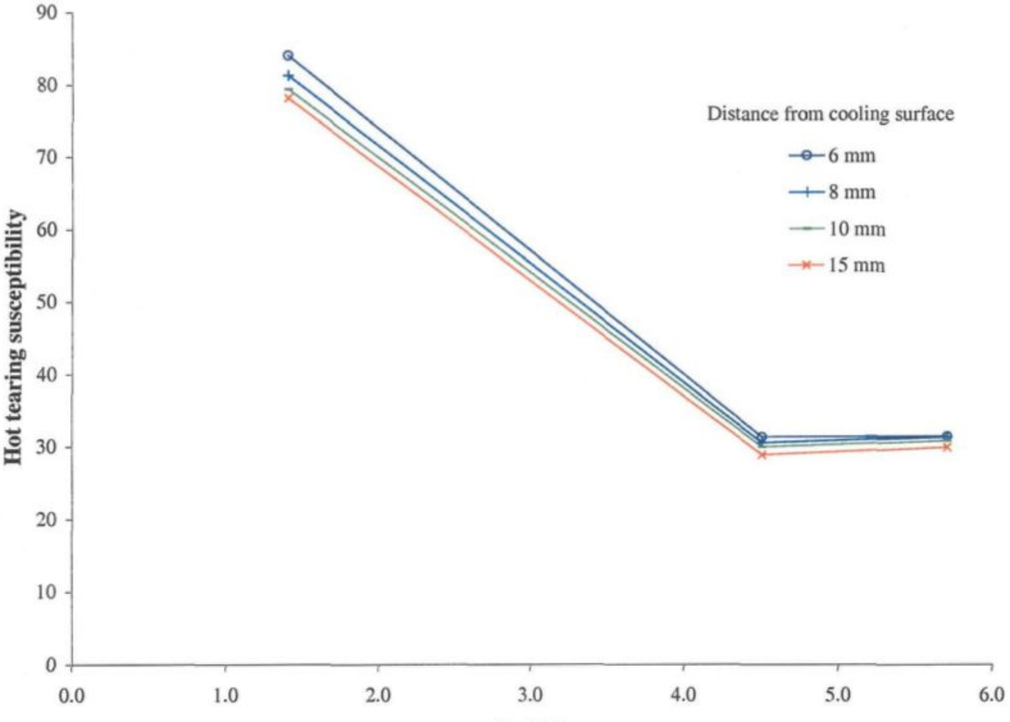

Figure 4.24 The effect of Cu content in Al-Cu alloy on the hot tearing susceptibility

Figure 4.25 shows the critical strain as a function of the distance from the cooling surface. It is obvious that the surface region is at lower temperature and higher fraction solid than the locations towards center at any time. The critical strain at surface, shown in stress – strain curve, is smaller and fracture stress is higher, as illustrated in Figures 4.26 to 4.28. It indicates the tensile strength of the body increases with the decrease in temperature, and the critical strain diminishes. This means the surface region of DCSS body has much higher hot tearing tendency. In fact, the hot tearing in DCSS samples was similar to that of DC cast ingots, often initiates at the surface and propagating towards the center. The predicted modelling results correspond well with the reality.

In general, the modelling results show that the LB criterion can qualitatively reflect how characteristics, such as cooling conditions, microstructure, alloy composition, and strain rate, influence hot tearing susceptibility. The critical point corresponds a fraction solid range from 0.85 to 0.97. This range is consistent with the hot tearing theory, which means hot tearing occurs only at higher fraction solid and with a liquid phase presence [88].

Note that the critical strain is a maximum value, a condition that must be endured before hot tearing can occur in any given material. If the strain is below this value anywhere in the body before solidification is complete, hot tearing cannot occur. Even if a stress-related strain is released in an area adjacent to a fully formed tear, a second tear cannot form.

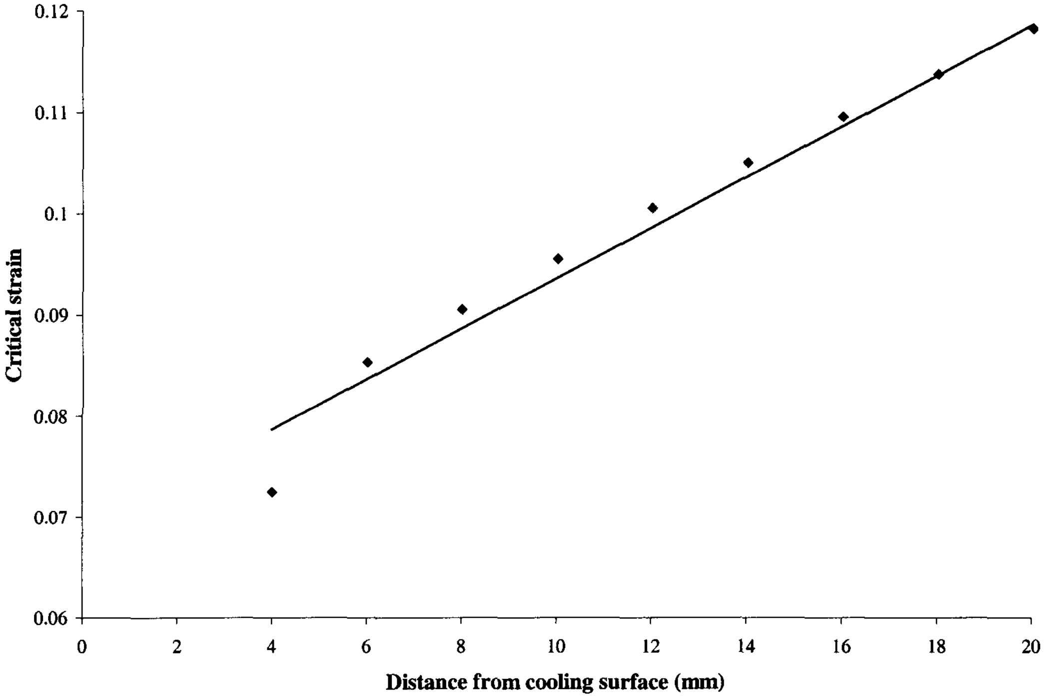

Figure 4.25 Critical strain as a function of distance from cooling surface

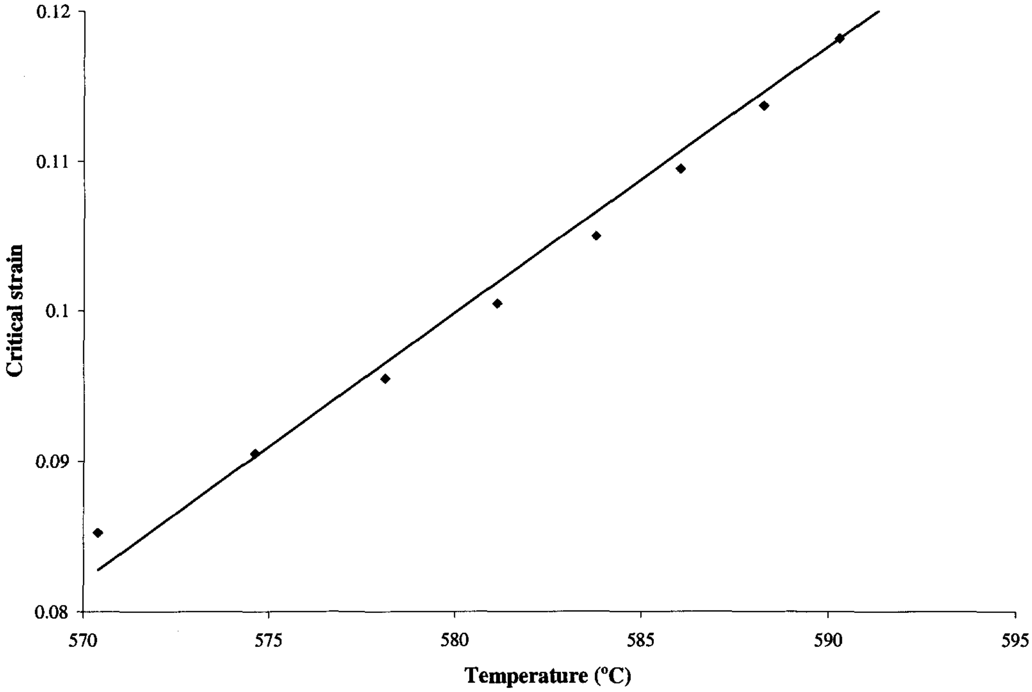

Figure 4.26 Critical strain as a function of temperature

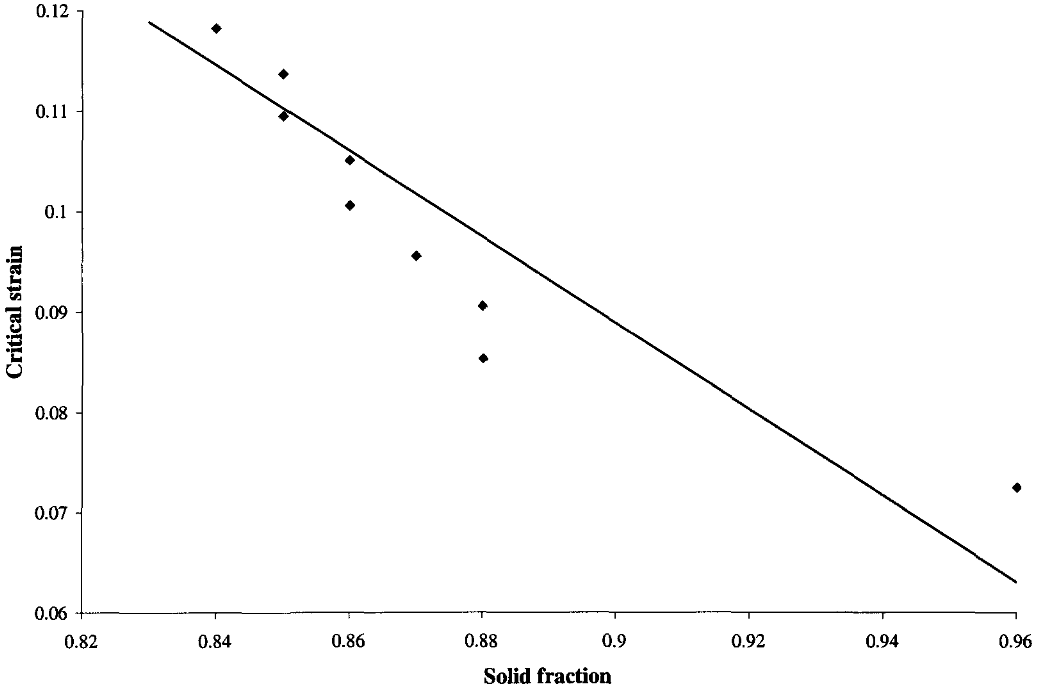

Figure 4.27 Critical strain as a function of fraction solid

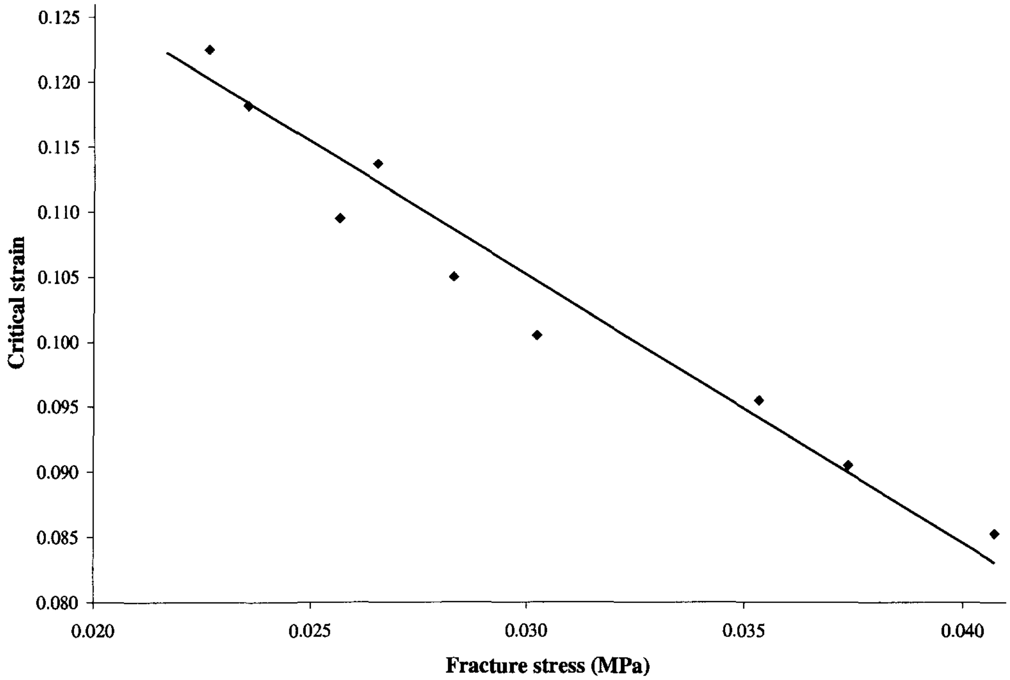

Figure 4.28 Critical strain as a function of fracture stress

The calculation of this criterion is very sensible regarding the strain rate, the modelling time interval and the mesh size, especially around the point of critical stain at the surface. For example, the applied strain rate should range from 0.001 to 0.01 for commercial castings [88], but it is sometimes difficult to obtain an accurate result from present modeling, when the strain rate is greater than 0.001. In fact, the constitutive law of the LB criterion is limited by certain strain value, beyond it the governing mechanisms for the deformation changes and the accommodation of the applied deformation is not possible by viscous flow in the liquid [64]. In this case the strain accumulated very fast under higher strain rate and easier passed the maximum limit causing the viscous description invalid.

4.2.2 RDG Criterion

RDG criterion is based on a mass balance performed over the liquid and solid phases. This criterion accounts for the deformation of the solid skeleton and for the feeding of the interdendritic liquid. A depression in the liquid at the roots of the dendrites is evaluated. If the pressure drop is greater than a given cavitation pressure, hot tearing will initiate and propagate from that position.

4.2.2.1 Modelling results

Figures 4.29 and 4.30 are the modelling results using RDG criterion for two different grain structures. The calculation of the shrinkage pressure drop dP_{sh}, and the deformation pressure drop dP_{mec} caused by thermal contraction, as well as the maximum pressure drop $dP_{\max}$ are based on the equations 3.28 to 3.30. The difference between two grain structures lies in the integration ranges. The integration is derived from the roots of the dendrites to

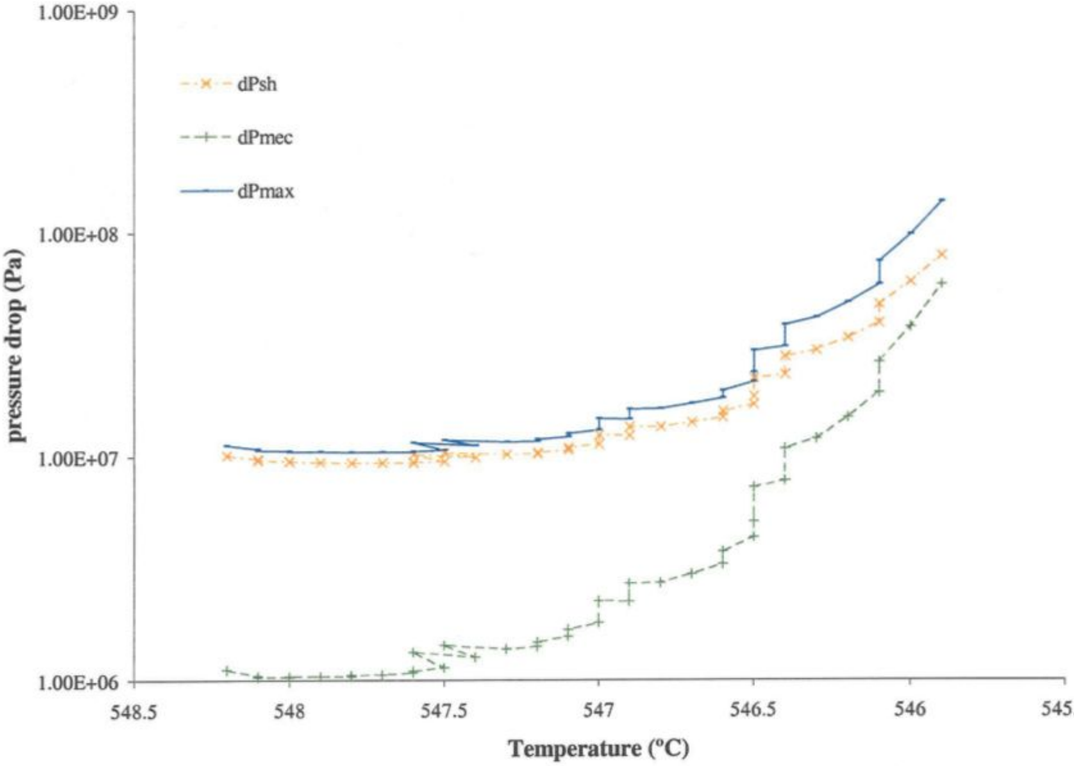

Figure 4.29 Modeling Results of RDG Criterion for columnar structure at 5 mm from the cooling surface

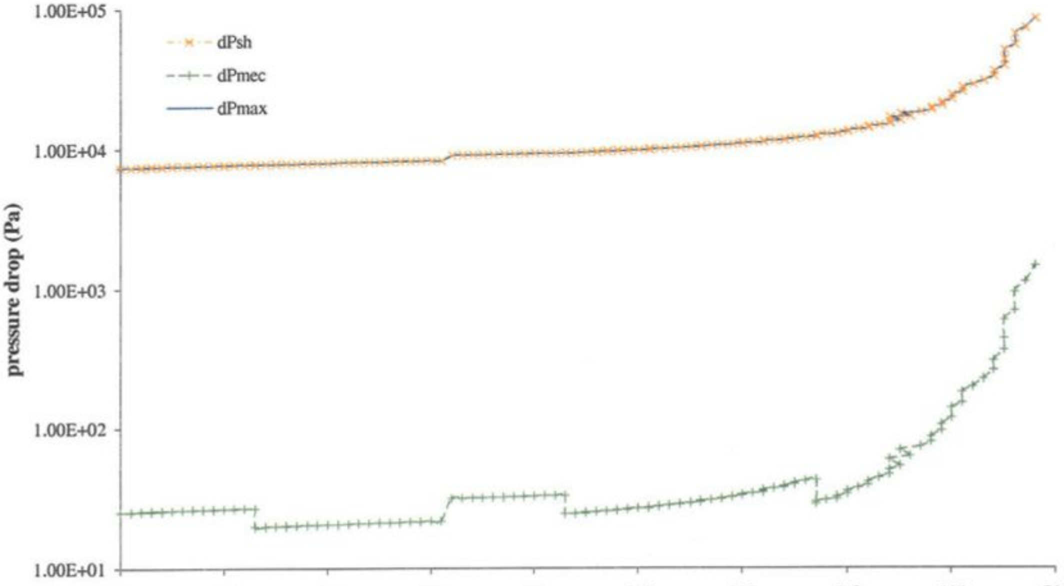

Figure 4.30 Modeling Results of RDG Criterion for equiaxed structure at 10 mm from the cooling surface

their tips; and for equiaxed structure, it runs from dendrite roots to dendrite coherent point, as shown in Figure 3.14. The modeling results show that the pressure drop from the columnar structure is much higher and increases more quickly than the equiaxed one. That means the columnar grain structure has a higher hot tearing susceptibility than the equiaxed grain structure, which is consistent with the experiment observation.

The maximum pressure drops against temperature at different locations are illustrated in Figure 4.31, which shows how, at the same temperature, the depression in the center is higher than at the surface.

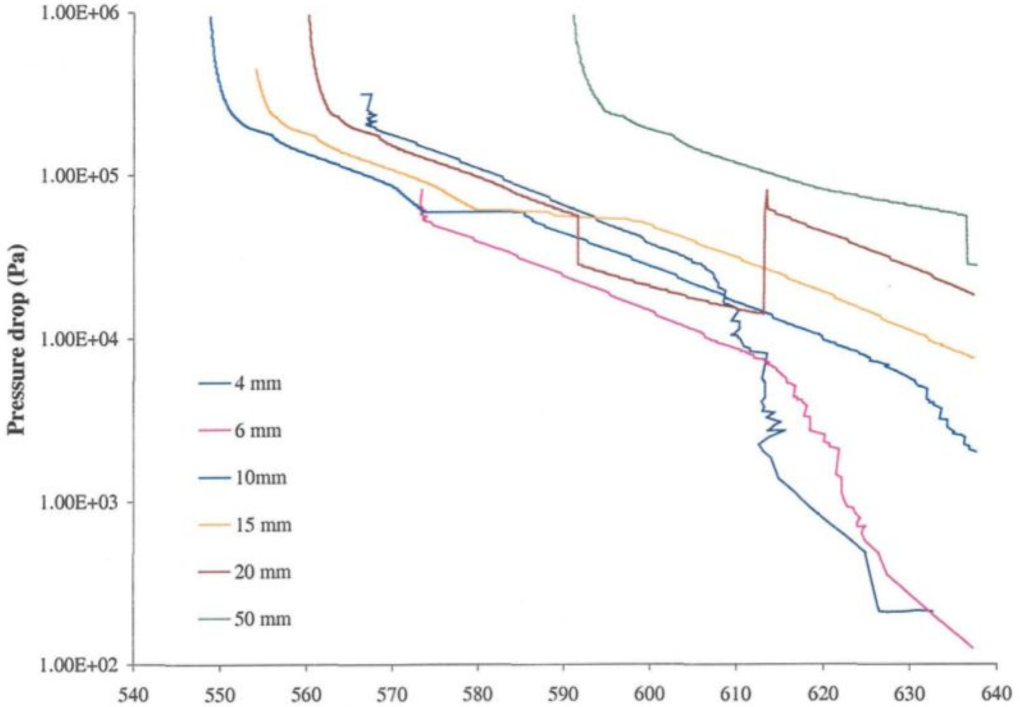

Figure 4.31 The maximum pressure drops against temperature at different location from surface

4.2.2.2 Discussion

As the modelling results were closely examined, some questions arose:

First, Figure 4.31 indicates that when the distance between the surface and the centre increased, the depression progressively increased as well in all temperature ranges. Therefore, the depression in the centre was much higher than at the surface; results show that the hot tearing initiated at the centre. In DC cast billets, the tearing seemed to occur only at the centre, usually called *central tearing*. However, in DC cast sheet ingots, hot tearing initiated mostly from the surface region. The modelling results using the RDG criterion seemed to match more closely to central tearing.

Second, according to the result from [72], the depressions caused by shrinkage and thermal deformation should be at the same magnitude. However, Figures 4.29 and 4.30 show the influence of shrinkage, (dP_{sh}), is 2 – 3 order of magnitudes higher than that of thermal deformation, (dP_{ε}). All of the modeling cases using RDG criterion obtained the same result, i.e. the maximum depression heavily depends on the shrinkage alone, which will rather lead to porosity [5]. Without the contribution of thermo-mechanical deformation, it is somehow contradictory to our general understanding of hot tearing mechanisms.

The third point is the role of fraction solid in hot tearing tendency. Figure 4.32 shows that, when the pressure drop exceeds the cavitation pressure, the corresponding fraction solid surpassed 40%, which is almost equal to the assumed coherency point. It is also paradoxical to the generally accepted theory that hot tearing occurs during the later stage of solidification, when the fraction solid is close to one.

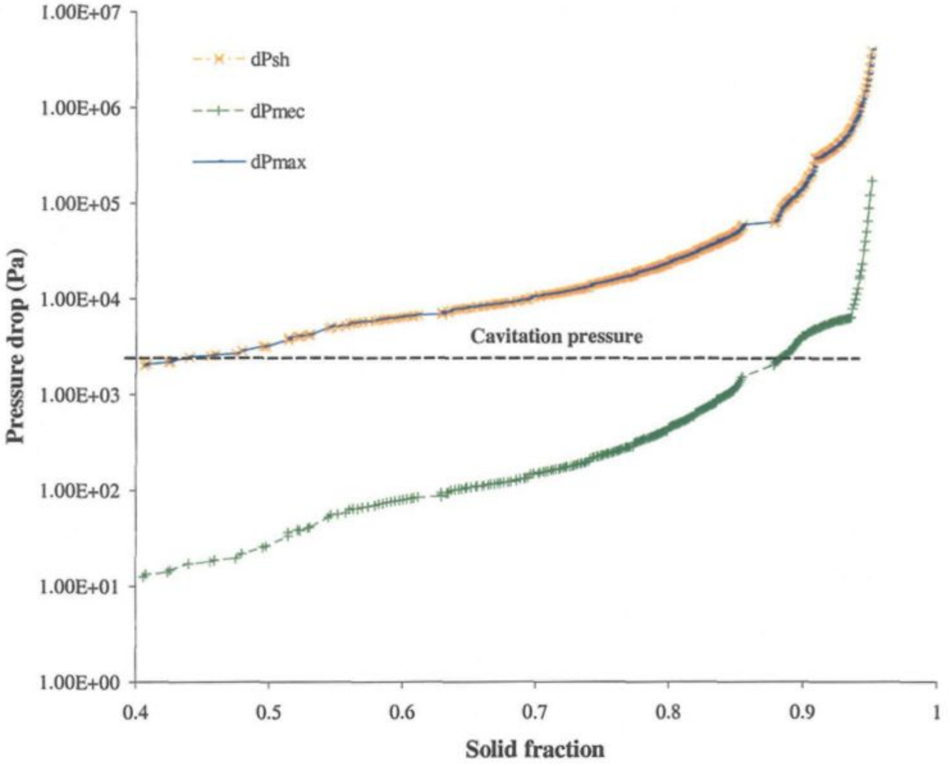

Figure 4.32 The pressure drop versus solid fraction at 10 mm from cooling surface

These concerns may be caused by the following reasons:

Until now the RDG criterion was used to predict central hot tearing in cast billets [72, 73], and in the horizontal magnesium-casting ingot [74]. Whether this criterion is also suitable to predict the surface hot tearing of DC cast sheet ingots would require further study.

When the RDG criterion module was integrated into the microstructural model, the unstable modeling result of columnar structure in the shell zone might affect the determination of the dendrite root, coherency point and solidification front locations. That could lead to inaccurate results.

The limitations of the PC based microstructural model, (such as the mesh size and time step) affecting the calculation of the pressure drop may play a role in the inaccuracy of the results.

As a matter of fact, the RDG hot tearing criterion is not emphasized in this project. Therefore, a future study of microstructural–hot tearing models using the RDG criterion would need to be improved. Further investigation is also needed to better understand the ranges and limits applicable to the RDG hot tearing criterion.

CHAPTER 5

EXPERIMENTAL RESULTS

CHAPTER 5

EXPERIMENTAL RESULTS

5.1 EXPERIMENTAL PROCEDURE

In order to validate the microstructural-hot tearing model using LB criterion, some experiments were carried out with Al-4.5%Cu alloy on the DC Casting Surface Simulator, which measures mechanical properties during solidification [80].

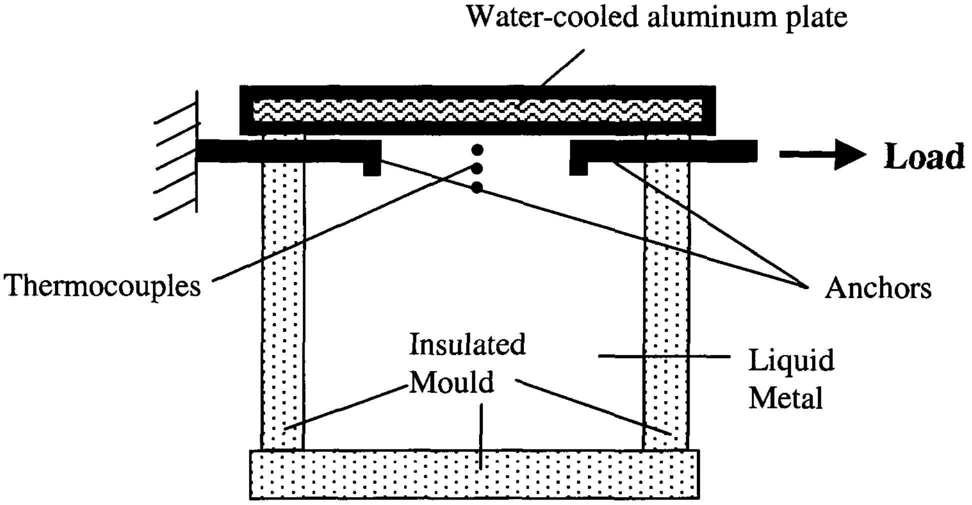

Figure 5.1 Schematic description of the experimental set-up

Figure 5.1 schematically shows the experimental set-up and Table 5.1 gives the conditions used in the experiments. The melt was poured into a refractory mold, which was preheated at 730 – 740 °C, at a temperature about 750 °C. Two anchors were put into the specimen at both sides. Three thermocouples at 5, 10 and 15 mm from the cooling surface were inserted to record the thermal history through the solidification. The grain refiner (one

Table 5.1 General experimental conditions

Specimen material	Al-4.5%Cu
Grain refiner	Al-5%Ti-1%B
Liquid temperature	~ 750 °C
Pouring temperature	>740 °C
Preheated temperature of mould	730-740 °C
Displacement speed of anchor (mm/s)	0.016 - 0.1
Average strain rate (s^{-1})[*1]	0.0017
Triggering beginning temperature (°C)[*2]	560 - 585
Triggering beginning time (s)[*3]	110-160
Fraction solid [*4]	0.85 – 0.92*

*1: Calculated.

*2, *3: The reference location is always at 10 mm from cooling surface.

*4: Fraction solid values were estimated from microstructural model at the correspondent temperature and at 10 mm from chill surface.

ppm of Al-5%Ti-1%B) was directly added into the mold just before the melt was poured in. Each test began when the melt temperature at 10 mm from the chilled surface cooled down to about 725°C. When it reached the target temperature, a unidirectional tensile load was perpendicularly applied at a predetermined rate (speed of displacement) until the specimen fractured or until time ran out. At the same time the deformation of the specimen was measured by an extensometer, which was placed on the chill surface of the specimen immediately after the desired temperature was reached.

The main parameters measured or calculated in each test were as follows:

- Load (applied to the specimen)
- Stress (calculated from load and effective cross-section of fracture area)
- Displacement (measured value by an extensometer)
- Strain (calculated from recorded deformation and the distance between the two clips of the extensometer)
- Strain rate (calculated from strain and duration of tensile testing)

5.2 EXPERIMENTAL RESULTS

The experimental results are shown in Figure 5.2. The marks indicate the location of the tears, and whether or not the hot tearing occurred at surface during the solidification. Although the experimental data is limited and the controlled experimental conditions not always identical, the risk of hot tearing seems to be lower when higher triggering temperatures and lower displacement speeds are used. When hot tearing occurred, the tears come up at different positions in the center of the cooling surface or at the sides, close to the anchors. The depths and widths of the tears are different, ranging from 3 - 10 millimeters, or right through the cross section. Figure 5.3 shows the specimens with tears at the center, or tears at the center and sides.

The relationship between measured deformation and the applied tensile load from the experiments is shown in Figure 5.4. Table 5.2 gives the details of the experimental conditions.

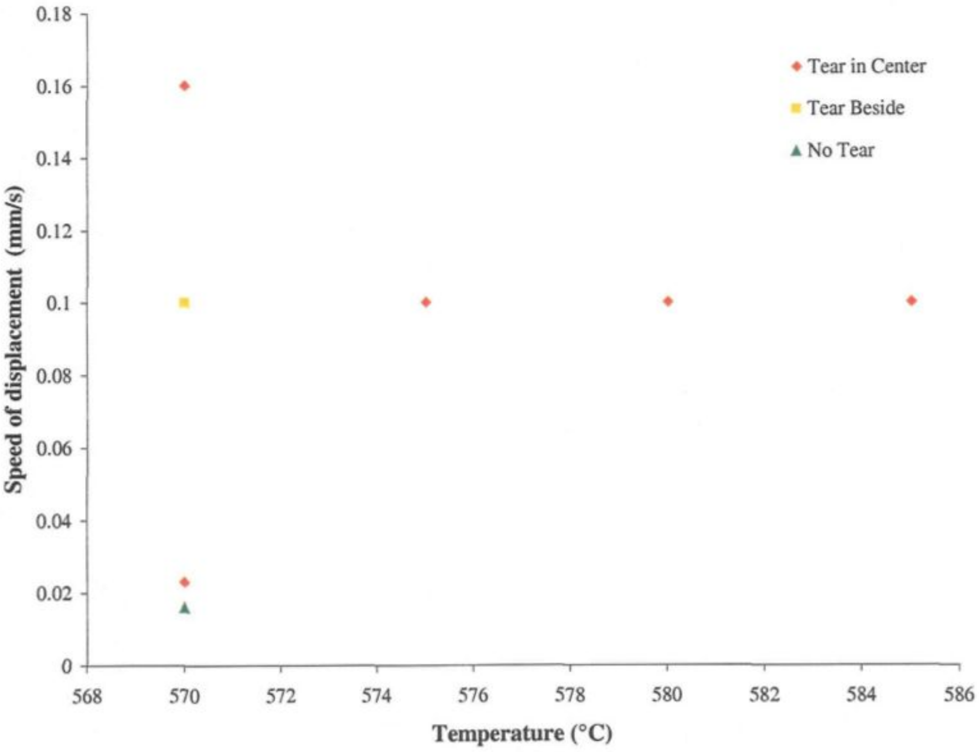

Figure 5.2 An overview of the experimental results. The marks indicated whether hot tearing occurred or not, and the location of tears

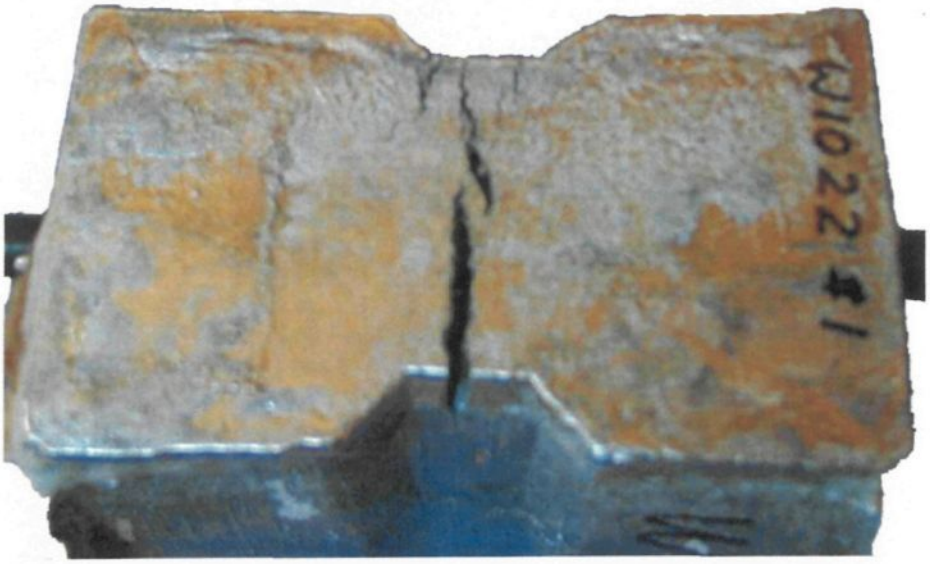

a) A tear in center

b) The tears in center and nearby the an anchor

Figure 5.3 The specimens with different tear location

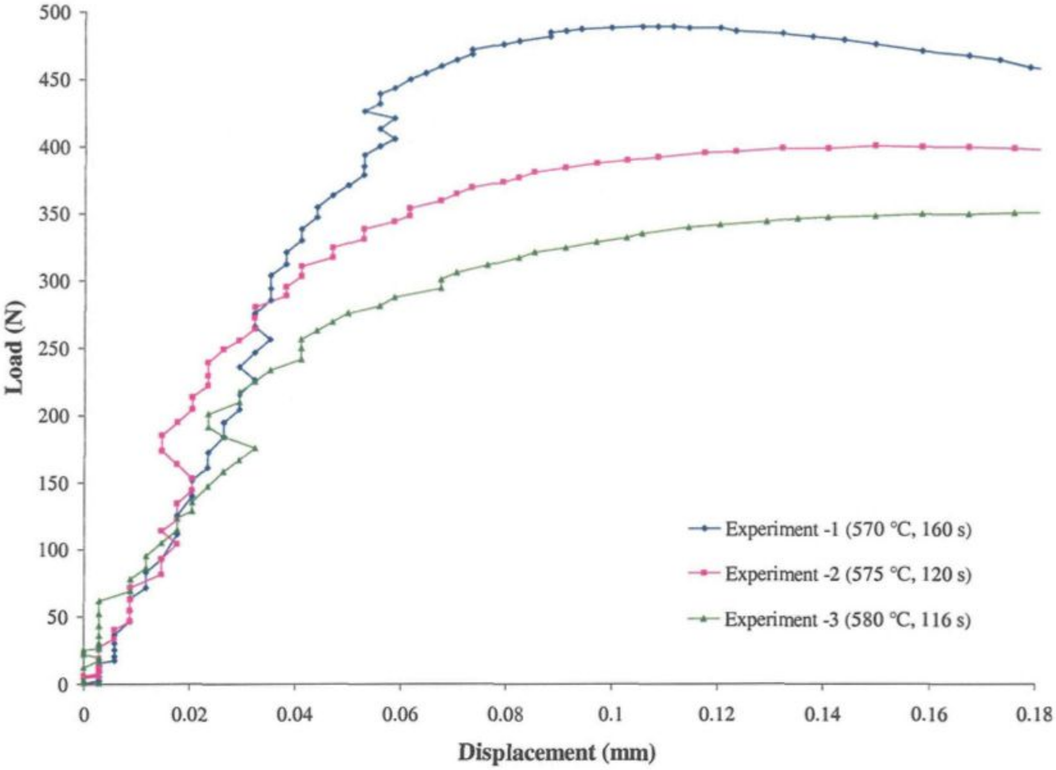

Figure 5.4 The relationship between measured deformation at the surface and applied tensile load of experiments

Table 5.2 Experimental conditions to Figure 5.4

	Experiment - 1	Experiment - 2	Experiment - 3
Speed of displacement (mm/s)	0.1	0.1	0.1
Average strain rate (s^{-1})	0.0017	0.0017	0.0017
Triggering beginning temperature (°C)[*1]	570	575	580
Triggering beginning time (s)[*2]	160	120	116

*1, *2 The reference location is at 10 mm from chill surface.

5.3 RESULTS ANALYSIS

As shown in Figure 5.4, the tensile loads versus deformation of the specimens in all three experiments are very similar in the beginning. However, the lower the triggered temperature is, the higher the applied maximum load must be to get the same deformation results.

5.3.1 Stress – Strain Curves

Figure 5.5 presents the temperature curves of three experiments with different triggering start-time and temperatures. Depending on the cooling conditions, the time from the beginning of the experiment to the triggering temperatures (570 – 580 °C) is about 116 – 160 seconds. The temperature-jump in these cooling curves was due to the change in the cooling conditions of the measured area, being suddenly switched from forced-cooling with a water-cooled plate to air-cooling, when the triggering temperature was reached.

To determine the effect hot tearing had on the area, the specimens were mechanically separated into two parts along the central fracture position, as seen in Figure 5.6. The hot tearing boundaries were first drawn based on the difference of the fractural appearance on both parts. The fractured section of each specimen was divided into several smaller units at 5 mm interval to measure the average tear depth. The hot tearing effective area was then calculated. The maximum stress was obtained by dividing the maximum tensile load by the effective area from. Figure 5.7 shows the relationship between the stresses and strains of the experiments and Table 5.3 provides more details for each experiment.

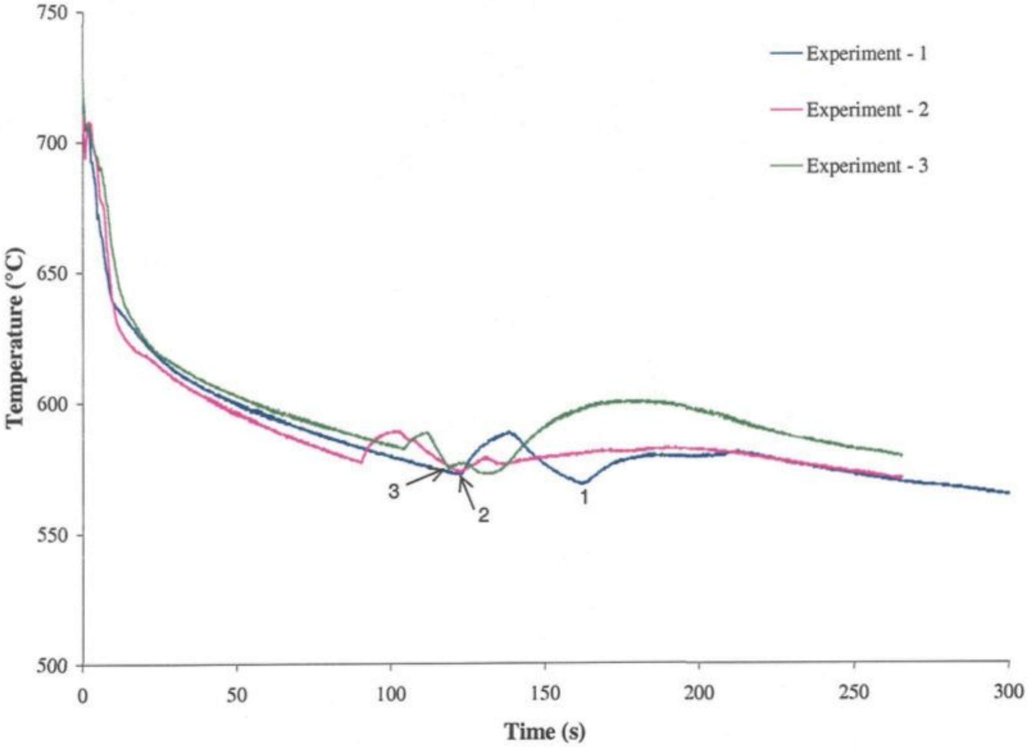

Figure 5.5 The cooling curves from the experiments. The different time points (1: 160 s; 2: 120 s; 3: 116 s) corresponding to the triggering temperatures of applied tensile load.

Figure 5.6 A cross-section view of a tear from a specimen

Note that Figure 5.7 demonstrates the same relationship trend between stresses and strains as the relationship between the tensile loads and the deformations when compared with Figure 5.4. The only difference was caused by a variation of experimental conditions – the stress was greater in Experiment 3, having a triggered temperature of 580°C, than that of Experiment 2, with a lower triggered temperature of 575°C.

Figure 5.8 presents the stress and strain versus time. It shows that when the tensile load was applied, stress and strain rose synchronously. It is believed that the hot tearing initiated the moment the stress reached its maximum value, although the strain was still increasing. This phenomenon was explained by Liangyi Zhao et al [66], who suggested the maximum strain occurs after hot tearing and the stress related to the maximum strain causes hot tearing, is extensive in the solid state.

A microscopic examination revealed no major differences between the specimens when the tensile load was applied at different temperatures.

Table 5.3 Calculated hot tearing areas and maximum stresses of each experiment

	Experiment - 1	Experiment - 2	Experiment - 3
Average tear depth (mm)	10	10	7.1
Average tear area (mm^2)	400	400	284
Maximum applied load (N)	488.57	399.93	350
Deformation at maximum load (mm)	0.105	0.15	0.176
Strain at maximum load (%)	0.46	0.65	0.76
Stress at maximum load (N/mm^2)[*1]	1.22	1.0	1.23
Fraction solid at cooling surface[*2]	~ 1	~ 1	~ 1
Fraction solid at 5 mm from cooling surface[*3]	> 0.98	> 0.95	> 0.95
Fraction solid at 10 mm from cooling surface[*3]	0.873	0.868	0.867

*1 Maximum load divided by the average of the effective tearing area of the test specimen.

*2 Fraction solid values were estimated from the microstructural model at a corresponding temperature.

*3 Fraction solid values were calculated from the microstructural model at a corresponding temperature.

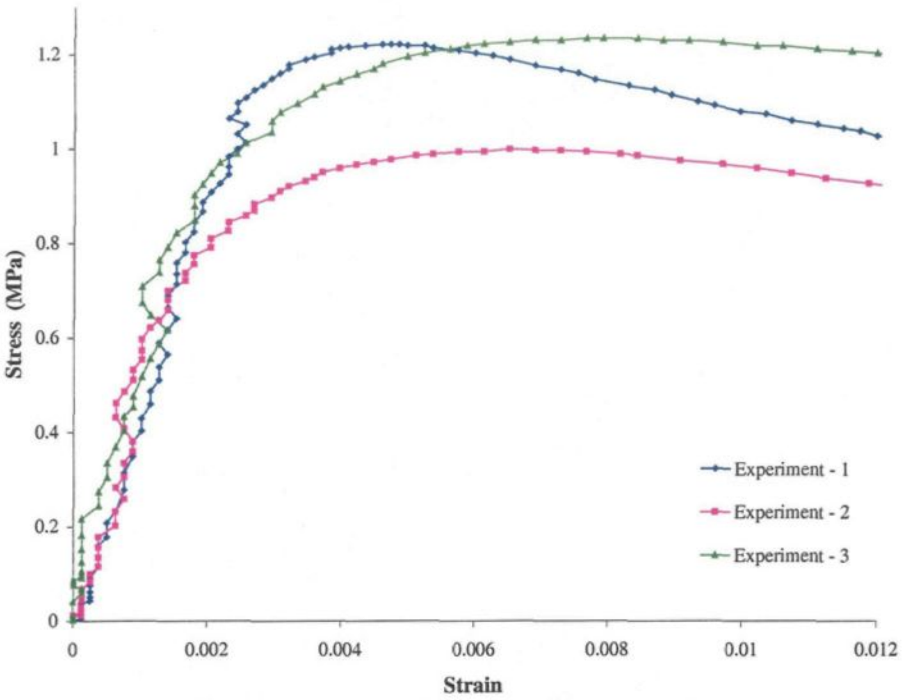

Figure 5.7 The stress-strain curves from experimental results

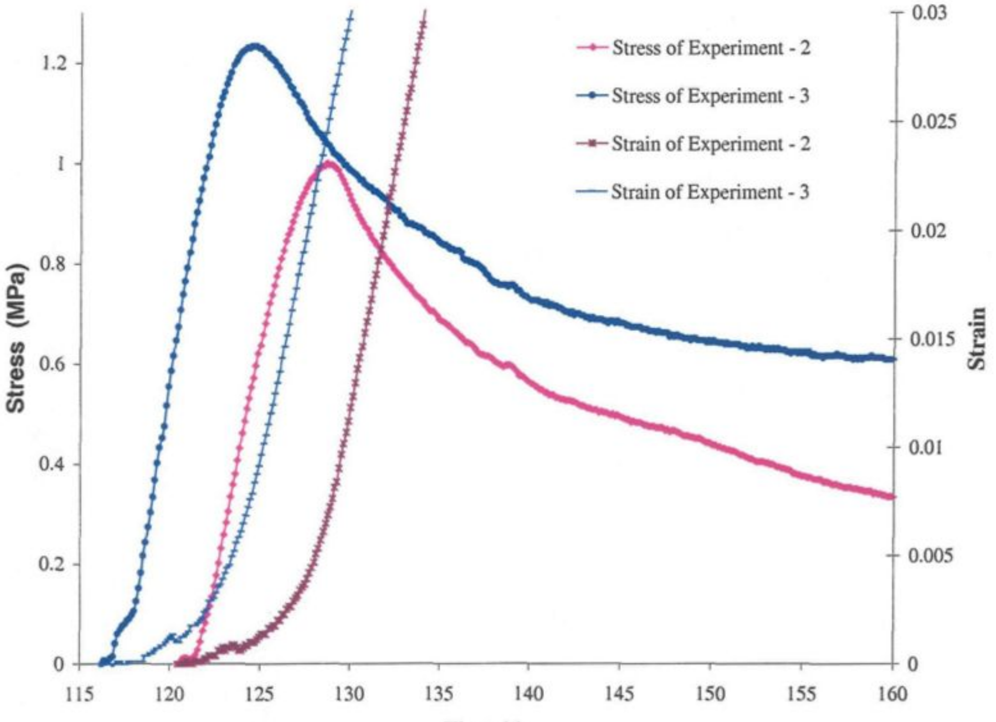

Figure 5.8 The relationship of stress and strain *vs*. time from the experimental results

5.3.2 Experimental Results from Experiments

Based on the tensile test observations on the Al-Cu alloys, the theoretical analysis gives a global relationship between stress, strain, strain rate and temperature, which involves both rheological and mechanical behaviors, and generally follows a power law [57, 66, 67, 68, 89, 90, 91]:

In the present experiments, the results until the maximum tensile loads were regressed by:

$$\sigma = k \dot{\varepsilon}^{n} \exp(\frac{Q}{RT}) \tag{5.1}$$

where, k is the pre-exponential factor, which directly relates to the deformation resistance, n is stress sensitivity constant, Q is the apparent creep activation energy and R is the universal gas constant, which is 8.3143 J/mole*k [92].

Figure 5.9 to 5.11 show the regression results of the three experiments by using the least square method. Table 5.4 summarized the regression results through the rheological analysis.

The regression results in Table 5.4 indicate that the value of the stress sensitivity constant n is contrary to the triggered temperatures. The lower triggered temperature means a higher fraction solid in the semi-solid body, and a more developed dendrite network, hence the stress rises. The pre-exponential factor k changes in proportion with the stress, if other parameters in equation 5.1 do not change.

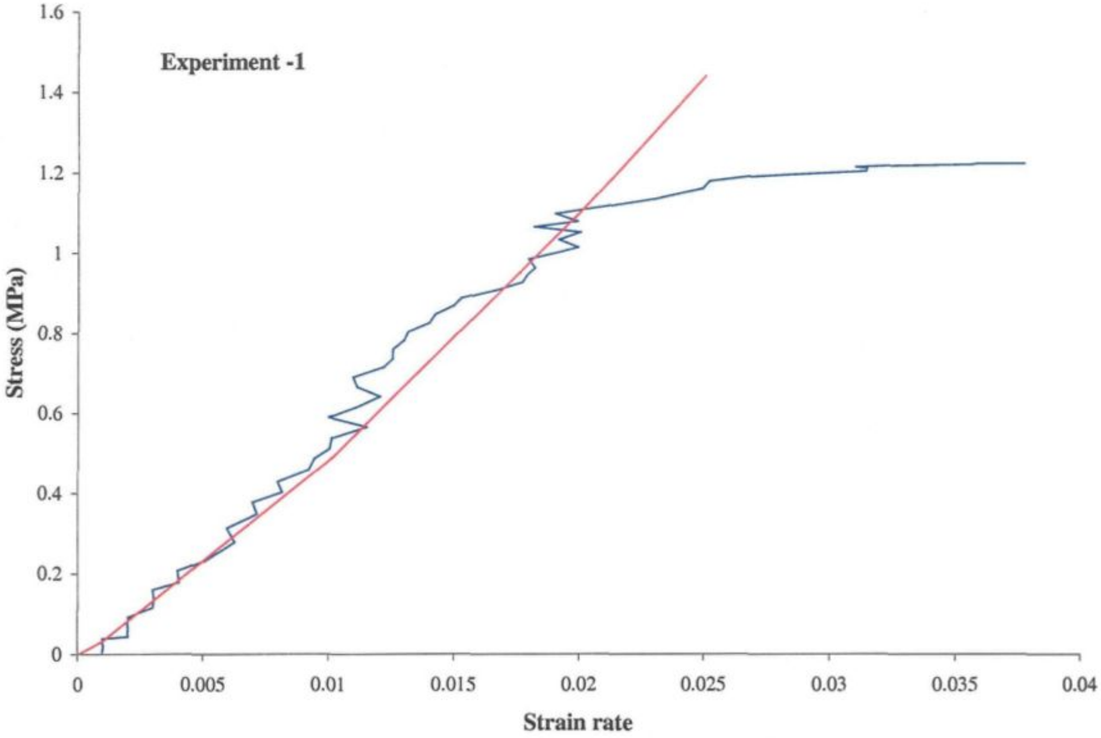

Figure 5.9 Regression result for experiment - 1

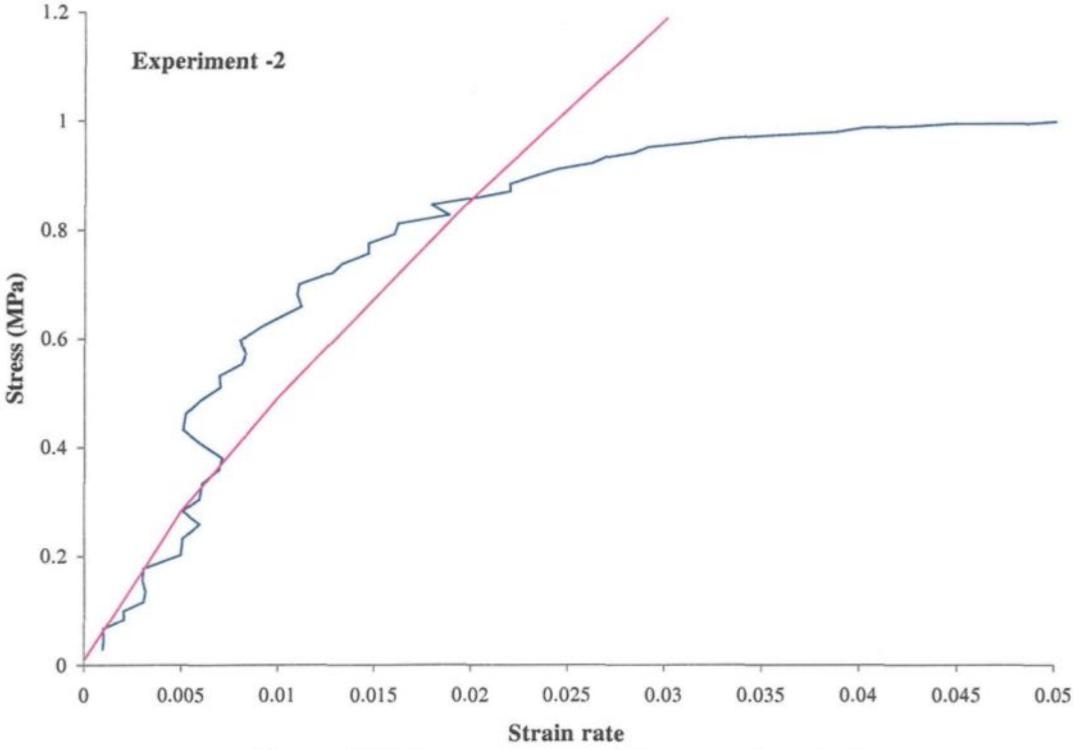

Figure 5.10 Regression result for experiment - 2

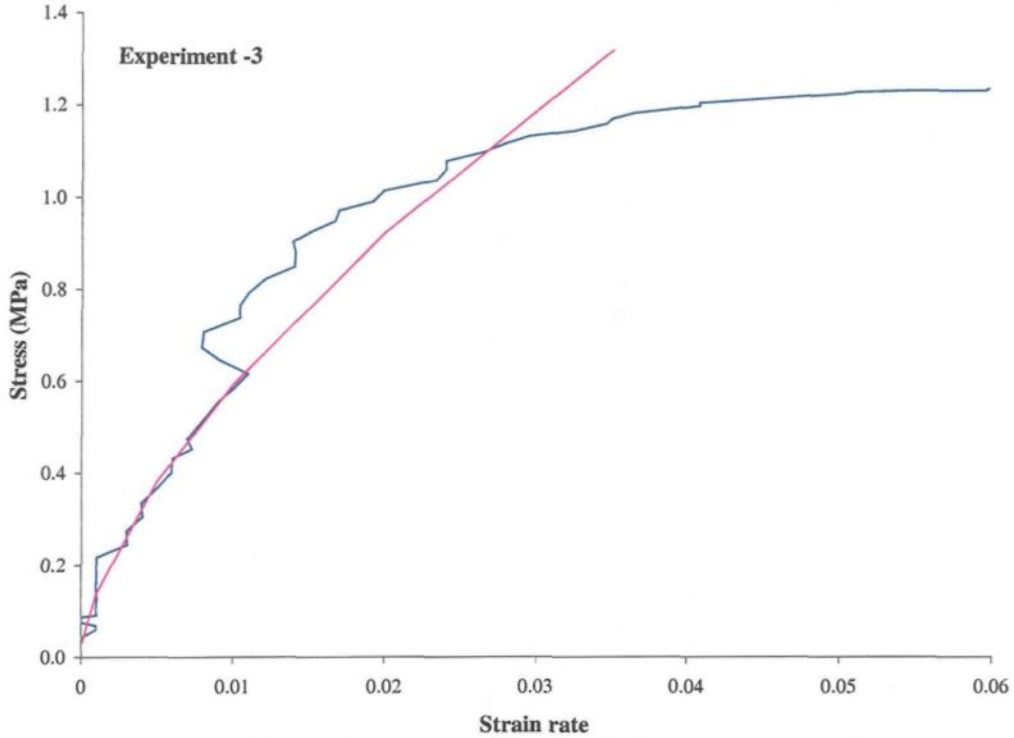

Figure 5.11 Regression result for experiment - 3

Table 5.4 The summary of regression results

	Experiment - 1	Experiment - 2	Experiment - 3
T (ºC)	570	575	580
k	0.306	0.398	0.818
n	1.194	0.802	0.636
Q/*R*	4959	3253	2174
r	0.974	0.934	0.959

k: Pre-exponential factor

n: Stress sensitivity constant

Q: Active energy, KJ/mole

R: Universal gas constant

r: Regression coefficient

5.4 COMPARISON BETWEEN THE RESULTS OF MODELLING AND EXPERIMENTS

In order to validate the combined microstructural – hot tearing (LB criterion) model, the modelling results were compared with the experimental data.

5.4.1 Temperature Field

Because the cooling conditions can influence the behaviors of the semi-solid body in the mushy zone and further the hot tearing tendency, the first thing to do is to get the temperature curves of the experiment to be as close as possible to those of the modelling during solidification. The heat transfer coefficient in the model was adjusted accordingly. Figures 5.12 and 5.13 provide simulated cooling curves to compare with the experimental ones at distances of 5mm and 10mm from the cooling surface. Table 5.5 gives the corresponding cooling rates for both curves. The heat transfer coefficient values between the specimens and the cooling plates were chosen to achieve a better temperature match between the experiments and modeling, see Fig 5.14.

5.4.2 Microstructure

At this cooling condition, the simulation results show that at a distance from the cooling surface, the structure was dominated by columnar dendrites before becoming full of equiaxed dendrites. Figures 5.15 and 5.16 are the modelling and the experimental results, respectively. The microstructure of the cast specimen shows that columnar grains are within 5-7mm from the cooling surface, which corroborates well with the predicted modelling results.

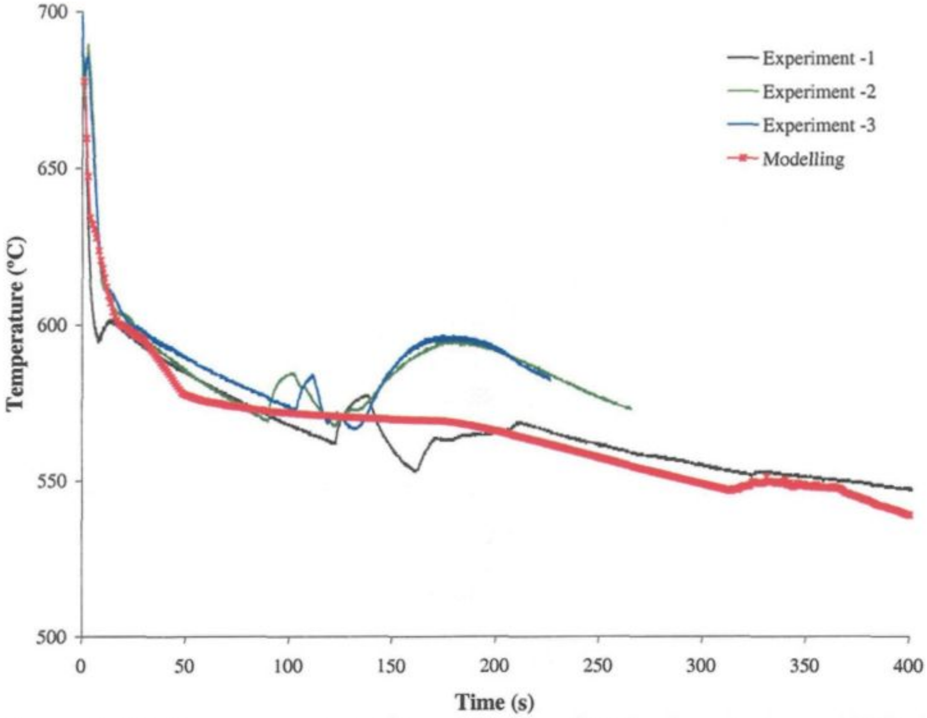

Figure 5.12 The comparison of temperature distribution during solidification srocess between modeling and experiments at 5 mm distance from the surface

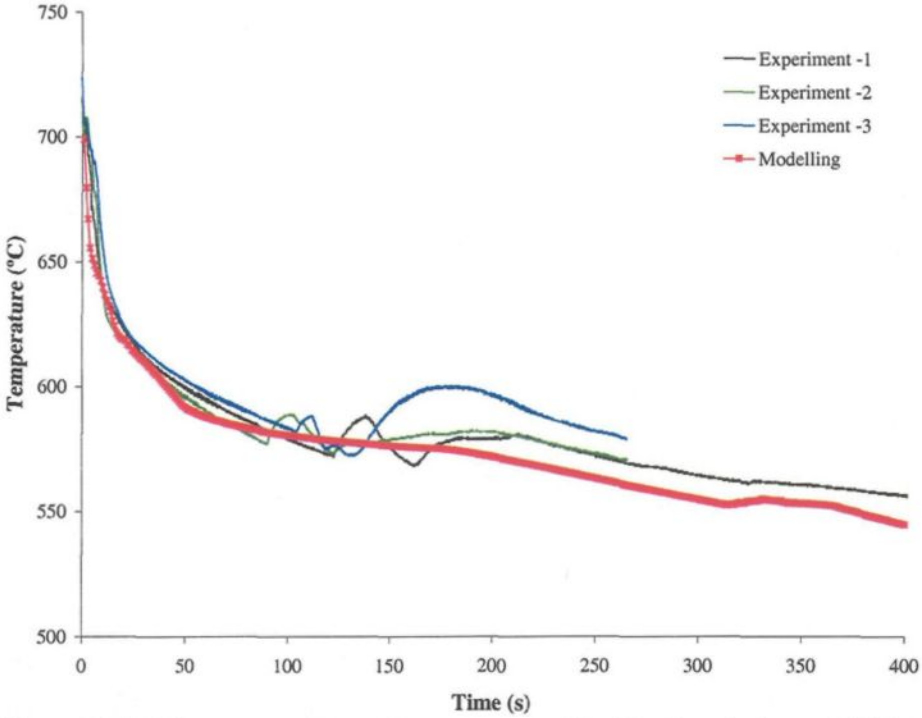

Figure 5.13 The comparison of temperature distribution during solidification process between modeling and experiments at 10 mm distance from the surface

Table 5.5 The cooling rates for experiments and modeling at 5 mm and 10 mm from surface, according Figure 5.12 and 5.13

	Cooling rate before liquidus (°C /s)		Cooling rate after liquidus (°C /s)	
	5 mm	10 mm	5 mm	10 mm
Experiment - 1	3.88	4.29	0.22	0.29
Experiment - 2	3.80	5.24	0.20	0.35
Experiment - 3	4.29	4.45	0.22	0.26
Modelling	4.5	4.20	0.24	0.34

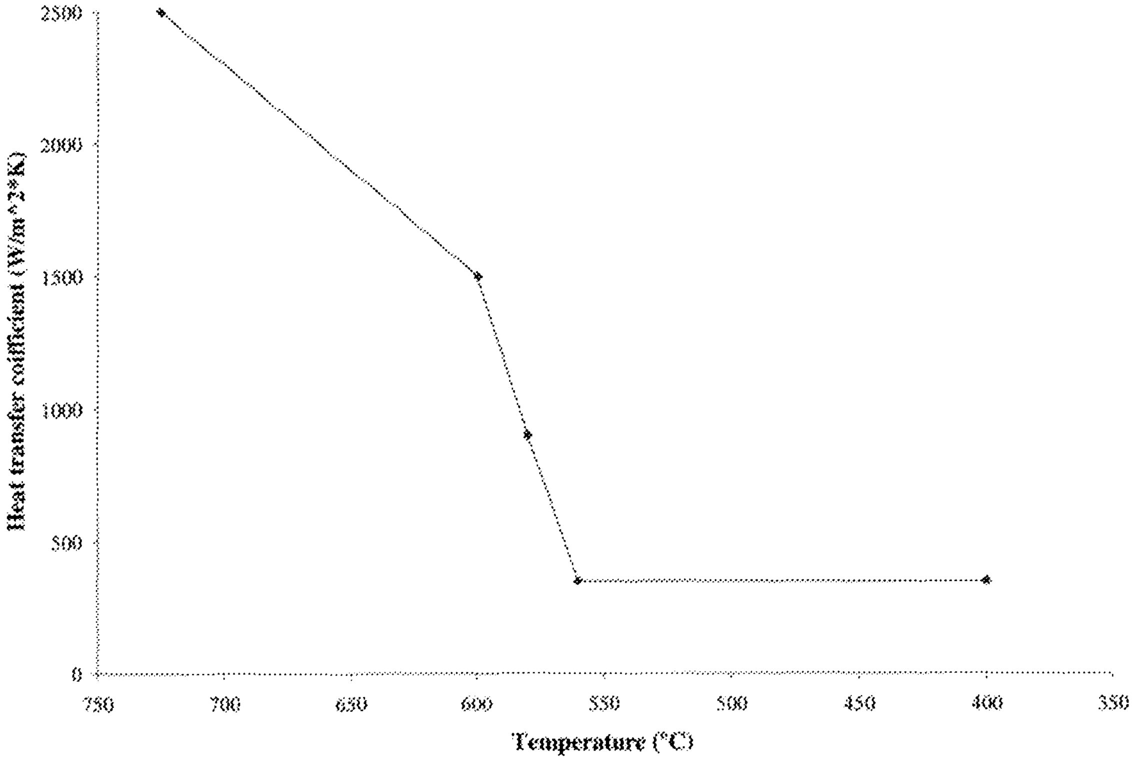

Fig 5.14 Heat transfer coefficient as a function of the temperature used in microstructural modeling (adjusted by the experimental results)

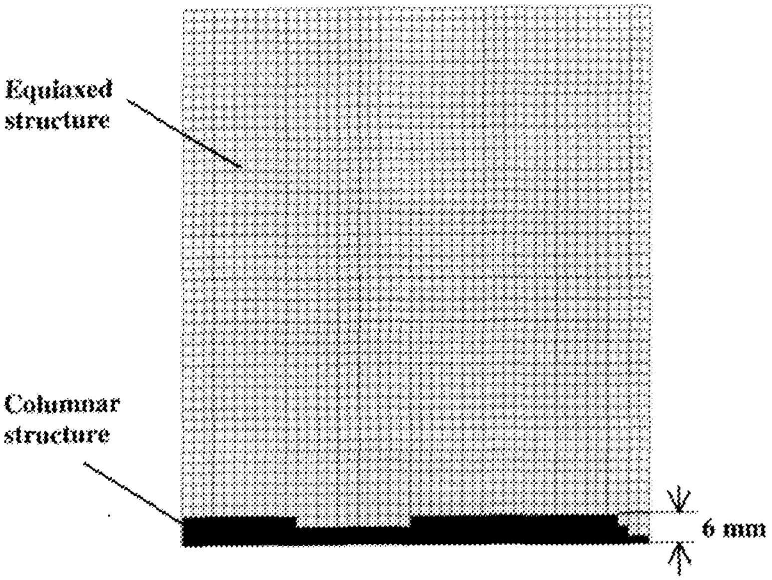

Figure 5.15 The microstructure from the modeling

5.4.4 Stress – Strain curves

Figure 5.17 gives the modeling results of the relationship between stress and strain under conditions similar (strain rate = 0.001) to the experiment (average strain rate = 0.0017). When one compares Figure 5.17 with Figure 5.7, the fracture stresses are almost at the same level (about 1 MPa). But there is also a discrepancy between the modeling results and the experiments. The critical strain from the modeling (i.e. it ranges from 0.07 to 0.095) is one order of magnitude greater than of the strain under the maximum stress in the experiments (from 0.004 to 0.008).

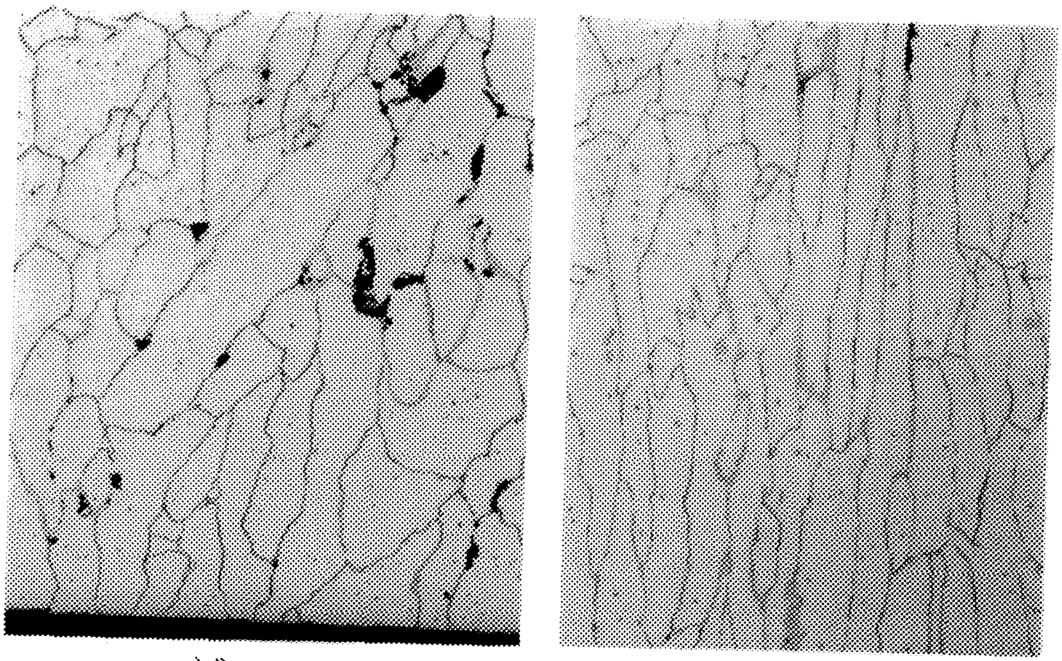

a) 0 mm

b) 5 mm

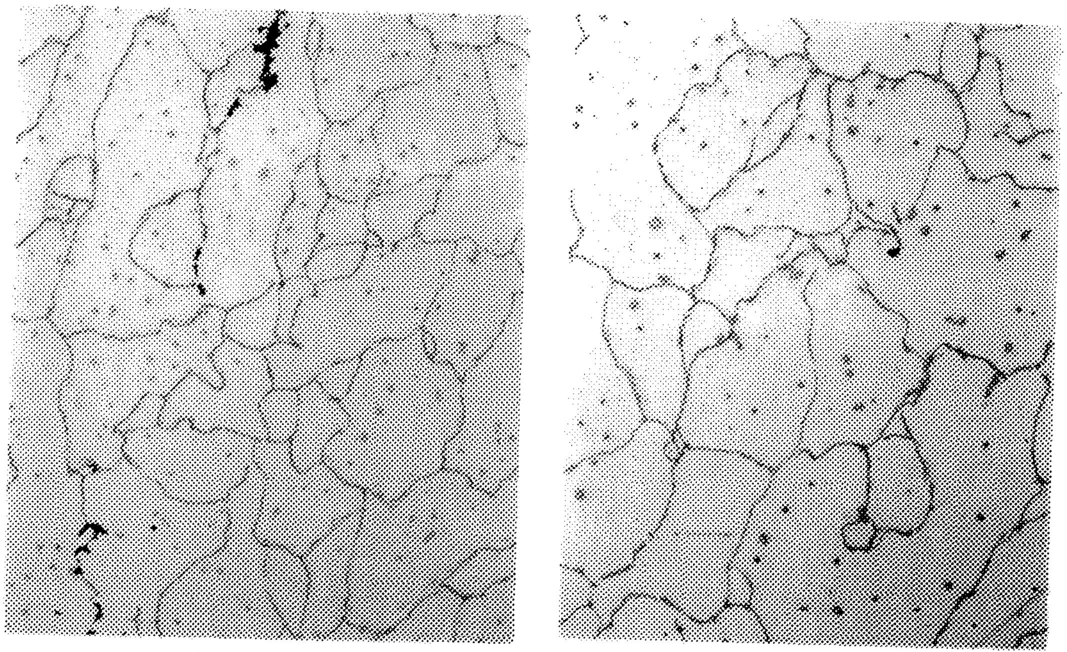

c) 10 mm

d) 30 mm

Figure 5.16 Microstructures from the experimental specimen at different locations (from surface towards center), 100x

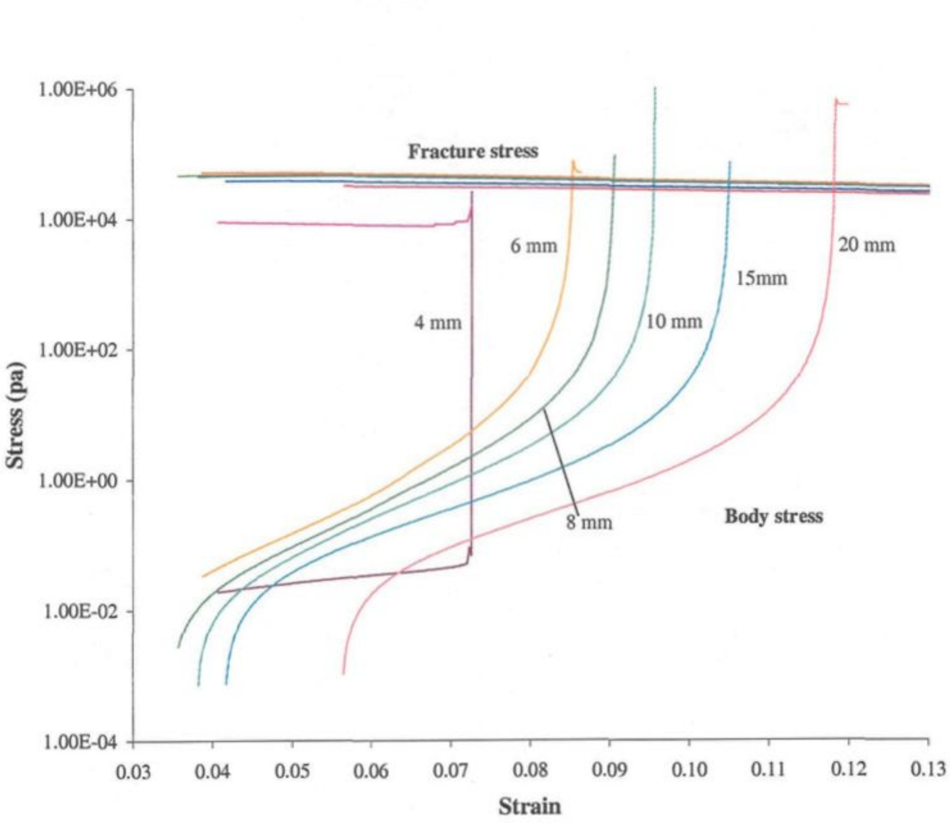

Figure 5.17 Modeling results of the relationship between stresses–strains under similar conditions with experiment, strain rate = 0.001

5.5 ANALYSIS AND DISCUSSION

Note that the modelling results, such as the temperature distribution during solidification, the final microstructure, as well as the fracture stress range, coincide well with those of the experiment by comparing the results between the complete microstructure-hot-tearing model (using the LB criterion) and the experiments. However, there is the discrepancy of the critical strain value between the modelling and the experimental data. First, the critical strain in modeling is far larger than experimental one. Second, the deformation process, which the modeling described, is completely disagreed by the experimental results, as shown in Figure 5.18. In the following section, some aspects are considered and the possible reasons are analyzed.

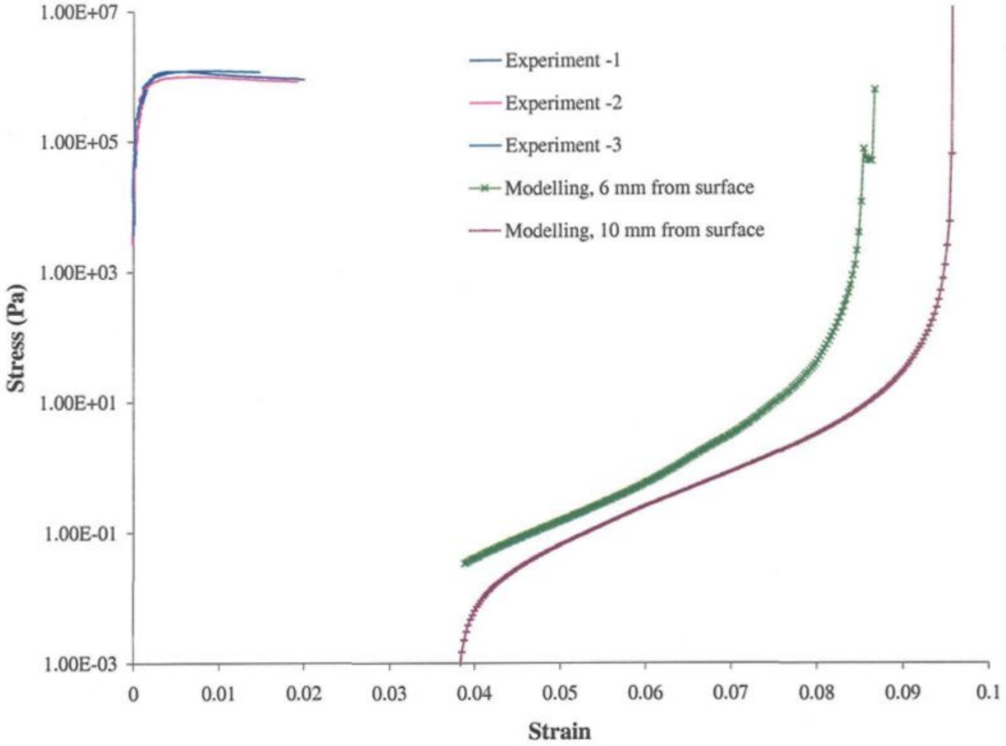

Figure 5.18 The comparison of the stress – strain curves between modeling and experiment

5.5.1 Assumption in LB Criterion

It is generally accepted that the hot tearing mostly occurs when the boundary of grains is surrounded by a thin liquid film. The separation stress, causing hot tearing, depends on the thickness of the liquid film at a later solidification stage, especially if it is very thin, as shown in Figure 5.19. The LB criterion is based on a simplified hexagon form, the grains are idealized and the liquid film is considered uniform. In reality, the liquid film is always non-uniform; the weakest point determines the critical limit, which is certainly smaller than the ideal case. Thus, the critical strain could be overestimated in the modeling.

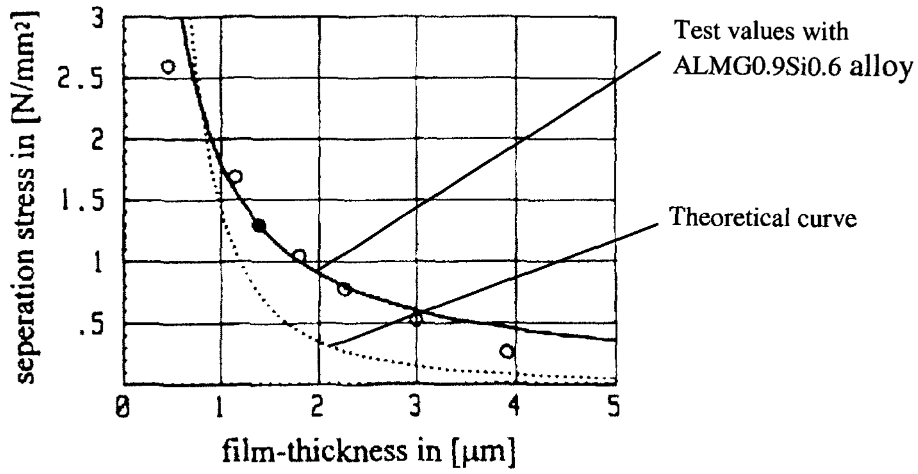

Figure 5.19 The relationship between the separation stress and film-thickness [36]

On other hand, the viscosity mechanism using in [64], which considered dominating the whole deformation process before hot tearing appeared, cannot adequately describe the actual deformation process occurring in reality. After the dendrite network formed in the mushy zone, the solid skeleton transmits the thermally induced stress and supports the deformation with the presence of a continuous liquid film surrounding the grains. In this case, the semi-solid body exhibits rather a viscoelastic behavior than the viscous one and should follow a creep law, which can better describe the mechanical response in semi-solid state [91,93].

To remedy the above-mentioned weakness of the model, D. Larouche recently developed a new constitutive model for tensile deformation of binary aluminum alloy within mushy zone [94]. This model is based on a less idealized microstructure, the average stress depends on the non-uniformed liquid channels surrounding the grains, as shown in Figure 5.20.

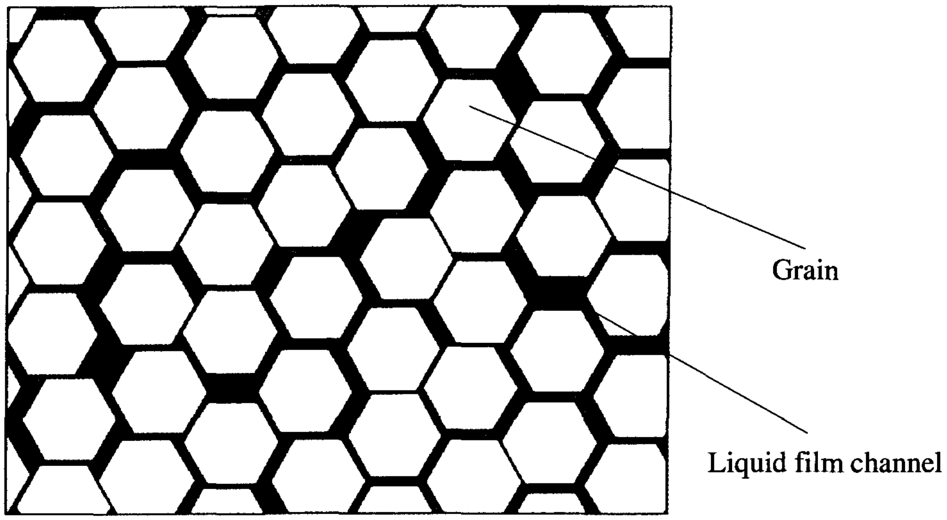

Figure 5.20 Schematic description of a less idealized microstructure [94]

In this modified model, the probability density of liquid channel thickness follows a lognormal distribution and a transit liquid channel thickness h_{trans} is considered. If the local liquid channel thickness is below h_{trans}, the deformation presents a creep behavior. Otherwise, viscous mechanism dominates deformation process. Thus, the average stress $\langle\sigma\rangle$ is consisted of two parts: creep mechanisms related stress $\langle\sigma_{creep}\rangle$ and viscosity mechanisms dependable stress $\langle\sigma_{visc}\rangle$. Figure 5.21 shows the calculated results of the modified LB model [94]. It can be seen that this model gives a fairly good agreement with the experimental results with a microstructure relevant geometric standard deviation $\phi_g = 4.2$. The description of this constitutive model for tensile deformation can be found in Appendix.

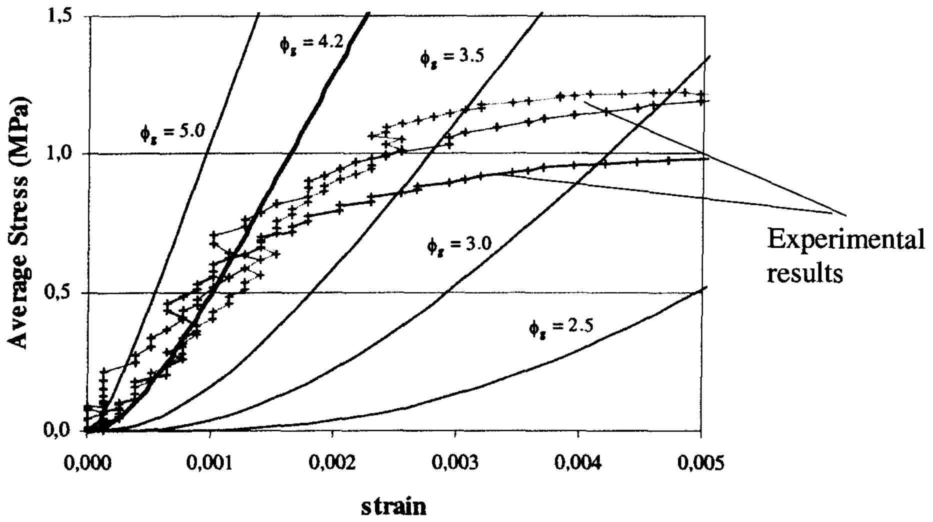

Figure 5.21 Comparison between the theoretical stress-strain curves and the experimental data [94]

5.5.2 Strain Rate

Strain rate influences the behavior of the stress at the shell zone [36, 71, 95]. Its variation could result from the difference in the temperature field and cause a non-uniform deformation [57]. At high temperature, all alloys exhibit creep even if the stresses are small and the variation of strain rate should be considered in the creep effect [4]. Figure 5.22 shows how the change of strain rate could affect the stress – strain curve. At the same strain level, a greater strain rate results higher stress. On the other hand, under same stress, the greater strain rate will reduce the critical strain limit. In the present model, the system is assumed to be submitted to a constant strain rate generated by the contraction during solidification. This assumption could also affect the modeling results.

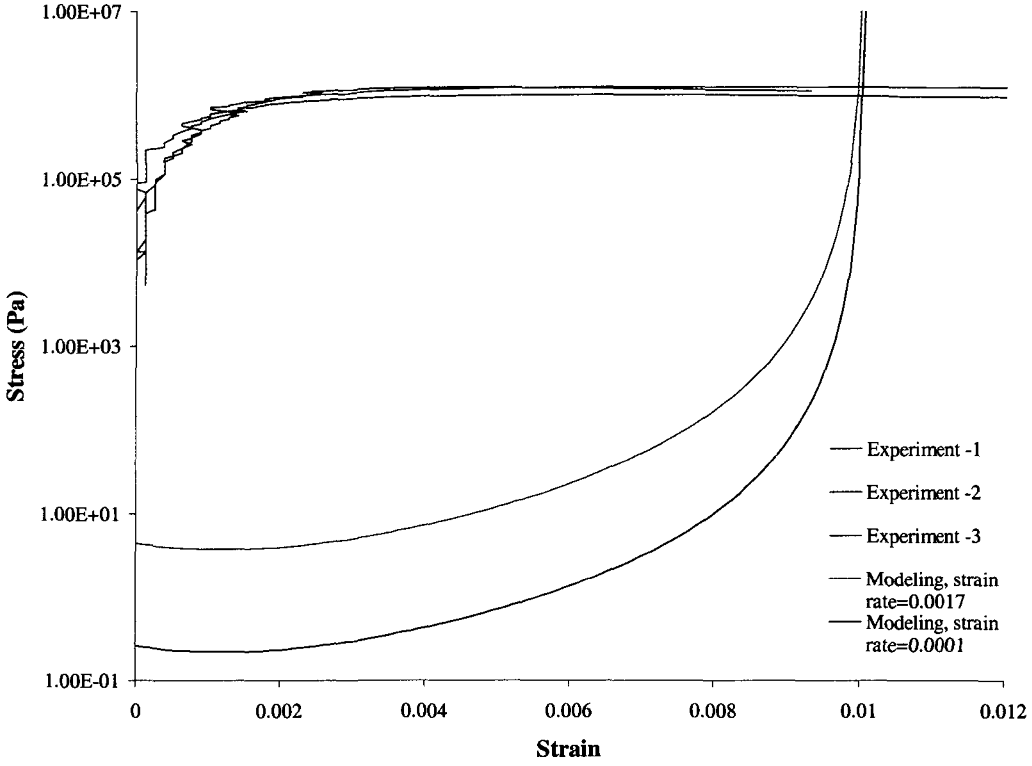

Figure 5.22 The influence of strain rate on the stress – strain curves
Strain rate is 0.0017 for experiments

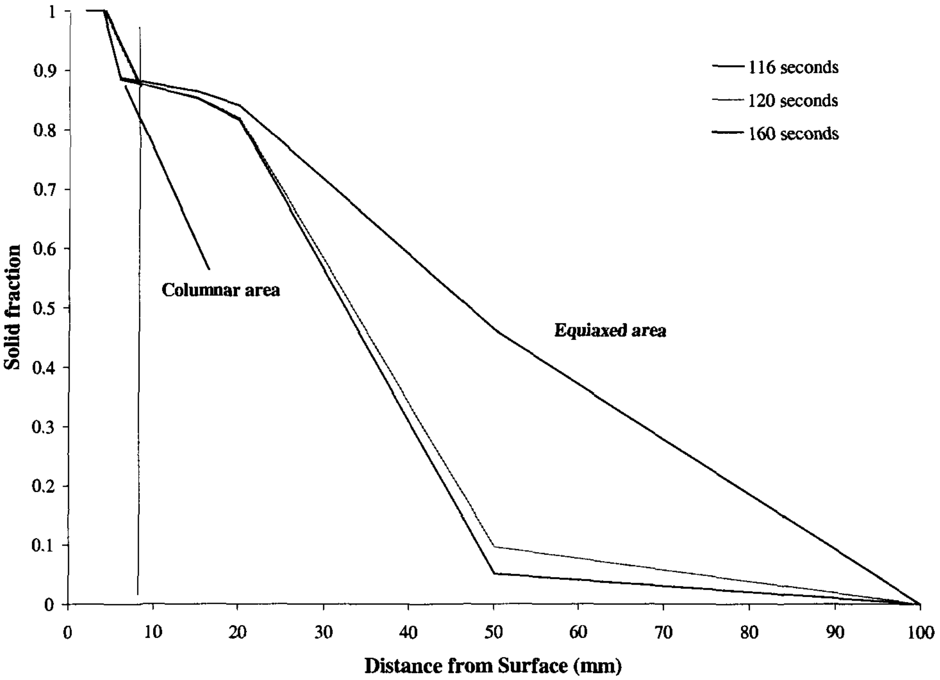

Figure 5.23 Fraction solid at a distance from the surface towards the center at a corresponding experimental triggering time, calculated from the model.

5.5.3 Influence of Fraction solid

As previously mentioned (Figure 4.27), the higher is the fraction solid, the smaller the critical strain. Figure 5.17 gives the stress – strain relationship beginning at 4 mm away from the chill (cooling) plate by modeling under the same conditions as in the experiment. However, in the present modeling, it is hard to know the exact fraction solid at the very surface close to the cooling plate. There, the solidification is very fast, but the mesh size and computational time step is not fine enough to describe it due to the limited capacity of the computer that was used. Certainly, the fraction solid is greater at the very surface than somewhere else at any time point, as shown in Figure 5.23. Considering this factor, the calculated results of the critical strain from the modeling would be more closely to the experimental results, as shown in Figure 5.24.

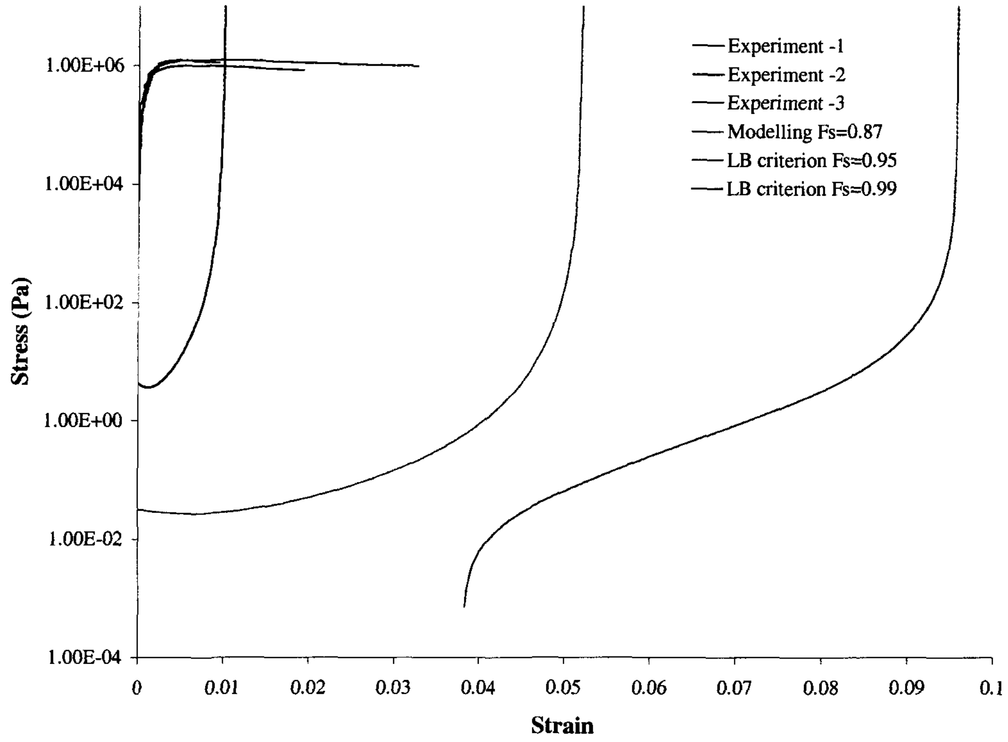

Figure 5.24 The influence of solid fraction on the critical strain

5.5.4 Difference of the Concept

There is another point that is considered to mention. The modeling condition of the present model emphasizes a natural solidification process. With temperature decreasing, a thermal contraction induced stress begins acting on the dendrite network after the coherency point. Simultaneously, the thermal strain cumulates gradually with the progress assumed to be submitted to a constant strain rate generated by the contraction during solidification. This assumption could also affect the modeling results.

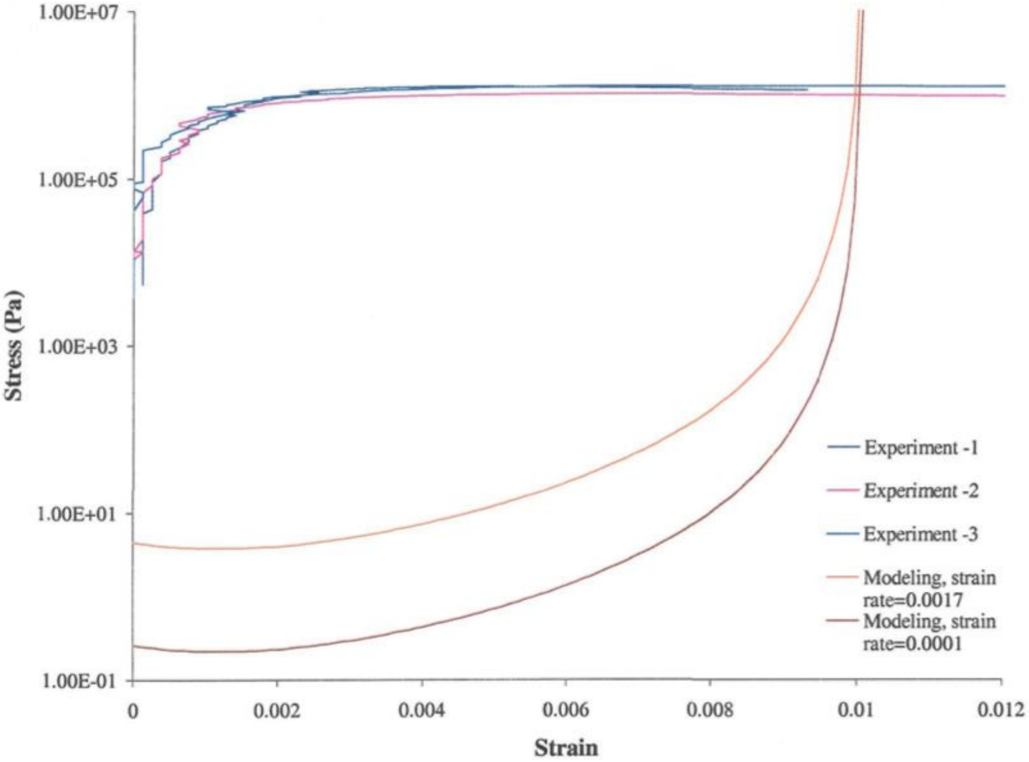

Figure 5.22 The influence of strain rate on the stress – strain curves
Strain rate is 0.0017 for experiments

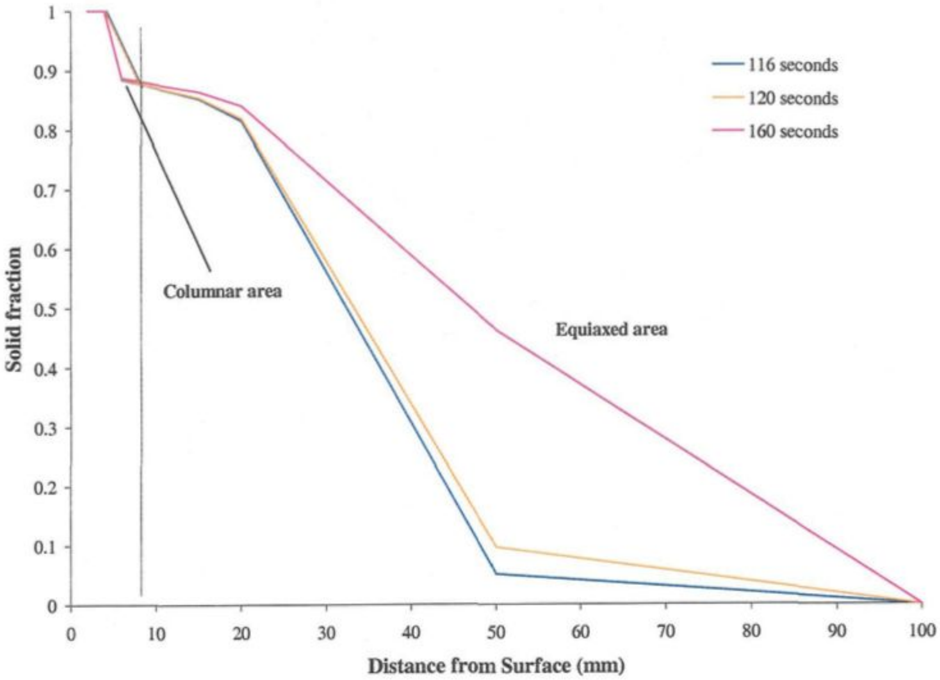

Figure 5.23 Fraction solid at a distance from the surface towards the center at a corresponding experimental triggering time, calculated from the model.

5.5.3 Influence of Fraction solid

As previously mentioned (Figure 4.27), the higher is the fraction solid, the smaller the critical strain. Figure 5.17 gives the stress – strain relationship beginning at 4 mm away from the chill (cooling) plate by modeling under the same conditions as in the experiment. However, in the present modeling, it is hard to know the exact fraction solid at the very surface close to the cooling plate. There, the solidification is very fast, but the mesh size and computational time step is not fine enough to describe it due to the limited capacity of the computer that was used. Certainly, the fraction solid is greater at the very surface than somewhere else at any time point, as shown in Figure 5.23. Considering this factor, the calculated results of the critical strain from the modeling would be more closely to the experimental results, as shown in Figure 5.24.

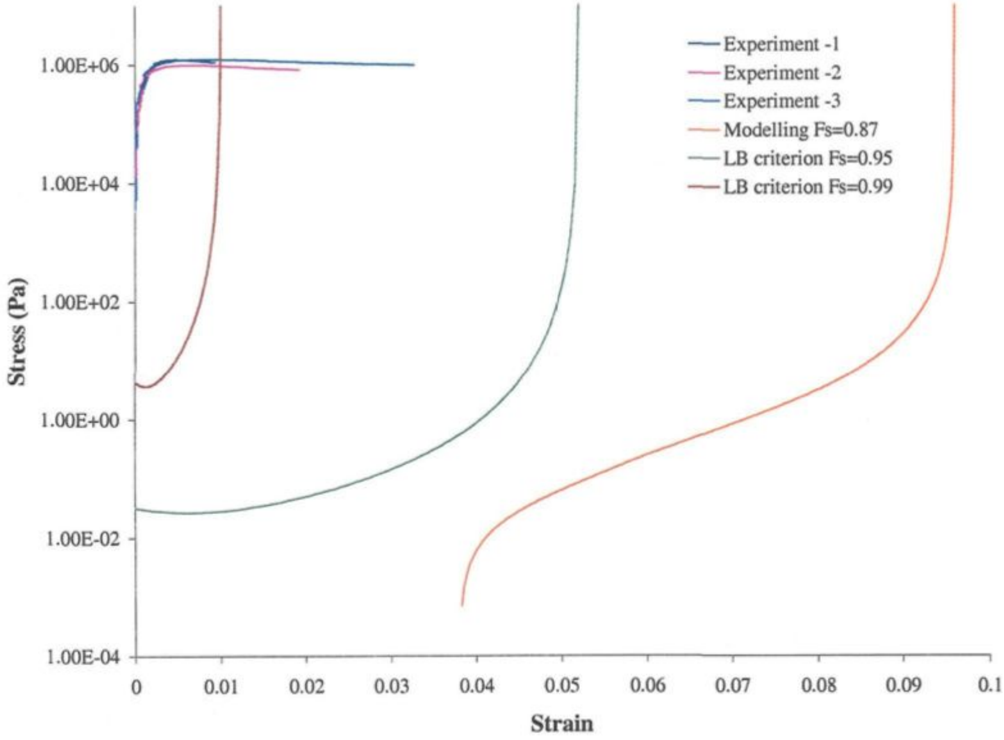

Figure 5.24 The influence of solid fraction on the critical strain

5.5.4 Difference of the Concept

There is another point that is considered to mention. The modeling condition of the present model emphasizes a natural solidification process. With temperature decreasing, a thermal contraction induced stress begins acting on the dendrite network after the coherency point. Simultaneously, the thermal strain cumulates gradually with the progress of solidification until it reaches a critical limit within the semi-solid body, which could lead to hot tearing. Unlikely, to investigate the susceptibility of the hot tearing, an external tensile load was applied at some predetermined temperatures in the experiments using the DC casting ingot surface simulator. From the beginning of the applied load to the appearance of hot tearing, it usually only sustains a few seconds. Hence, the behavior of the current modeling based on an internal growing stress is not the same as the mechanical load from an uniaxial tensile test [96]. This difference could affect the comparison results between the modeling and experiments. To better characterize the behavior of a real casting under the external loading, a rheological mechanism is necessary to be considered in the model [91, 94].

CONCLUSIONS

The existing two-dimensional microstructural model has been improved and two hot tearing criteria have been incorporated. In order to validate the coupled microstructure – hot tearing model emphasising the LB criterion, the experiments were carried out on the DC Casting Ingot Surface Simulator. The modeling results were compared with the experimental results.

Microstructural model

This model involves the solidification phenomena such as nucleation, dendrite growth, latent heat release effect and the columnar to equiaxed transition as well as the heat transfer effect like the interaction of temperature distribution between the specimen and the cooling plate. It provides basic information, like temperature field, evolution of fraction solid, final grain size and microstructure morphology, which are essential for the further studies of hot tearing, which involves both solidification and process. The modelling results of the microstructure evolution agree well with the experimental data.

Microstructure – hot tearing model using LB criterion

This model, which is based on an idealized representation of the microstructure, describes the mechanical response of the semi-solid body. By combining the constitutive law that reflected the viscous behavior and the critical fracture based on the capillary force, a critical strain can be calculated to identify when and where hot tearing could occur. The modeling results give an overall indication of the appearance of hot tearing, and can be used to investigate the susceptibility of hot tearing tendency influencing by the solidification parameters and the thermal properties of the Al-Cu alloys.

Generally, the critical strain is influenced by:

- Cooling condition. A cooling rate reduces the critical strain.
- Alloy composition. Al-1.5%Cu alloy shows more sensitive to hot tearing than Al-4.5%Cu and Al-5.7%Cu alloy.
- Strain rate. A higher strain rate reduces the critical limit, thus increases the risk of hot tearing.

The surface of the specimen was under lower temperature conditions, higher volumes of solid fraction, and subjected to smaller critical strains than others were. Therefore, the surface region had a higher hot tearing tendency.

To predict hot tearing, the model at the current stage provides a general fracture stress level as well as the location and time point of hot tearing. However, it cannot yet adequately describe the deformation behaviors of the reality nor give a reasonable critical strain range, due to some simplified assumptions and a lack of the rheological mechanisms in the model. Using a modified model, this weakness may be corrected and more comparable results between modeling and experiments can be expected.

Microstructure – hot tearing model using RDG criterion

This model considers the influence of pressure drop from both the thermal deformation and the solidification shrinkage. The modeling results show that it is more suitable for the central type of hot tearing. In general the modeling results for the RDG criterion are unsatisfactory in the current applied condition. It needs to be studied more to know whether this criterion is applicable for the surface hot tearing as in the case of DC cast sheet ingots.

SUGGESTIONS FOR FUTURE WORK

In order to get better-appropriate prediction model for hot tearing, some improved works should be done in the future.

First, it is necessary to solve the stability and convergence problems, especially for columnar growth mode in the microstructural model. A concentrated study of the surface is also important to obtain more details on the behaviours within this region during the later stages of solidification, to obtain better modelling accuracy.

Second, it is recommended to couple the modified constitutive model in reference [94] with the microstructural model to properly describe the deformation behaviour of the semi-solid body in the mushy zone. The influences of different microstructures, thermal conditions, composition of the alloys as well as microsegregation and macrosegregation on hot tearing tendency should be further investigated to better predict the hot tearing occurrence.

Third, for the study of surface hot tearing during DC casting, more effort is required to adapt future microstructure-hot-tearing models using the RDG criterion. It is worth to mention that the shrinkage porosity has been considered in the hot tearing forming process in the RDG criterion. But the hydrogen level in the liquid aluminium also has a great impact on the porosity. The significance of hydrogen influence on the hot tearing, particularly on the initiation of hot tearing, should be further studied.

APPENDIX A

A Modified Constitutive Model for LB Criterion [94]

In a less idealized microstructure model (see Figure 5.20), the average stress $\langle\sigma\rangle$ depends on the local channel thickness h:

$$\langle\sigma\rangle = \int_0^\infty \sigma \cdot \Psi_{\ln} \cdot dh \qquad (1)$$

$\Psi_{\ln}$ is the probability density of h, which follows a log-normal distribution:

$$\Psi_{\ln} = \frac{1}{h \cdot \ln\phi_g \cdot \sqrt{2\pi}} \exp\left[-\frac{1}{2}\left[\frac{\ln h - \ln h_{med}}{\ln\phi_g}\right]^2\right] \qquad (2)$$

where, h_{med} is the median value of h and ϕ_g is the geometric standard deviation.

As it in reference [64], the local fraction solid f_s is related to the channel thickness h:

$$h = a\sqrt{3}\left[\frac{1-f_s^m}{f_s^m}\right] \qquad (3)$$

and according the log-normal distribution, h_{med} is then given by:

$$h_{med} = h_{mean} \cdot \exp\left[-\frac{(\ln\phi_g)^2}{2}\right] = a\sqrt{3}\left[\frac{1-f_{s\,\mathrm{mean}}^m}{f_{s\,\mathrm{mean}}^m}\right] \cdot \exp\left[-\frac{(\ln\phi_g)^2}{2}\right] \qquad (4)$$

Assuming there are only two sliding mechanisms operate to the local value of h:

- Fully lubricated sliding if $h > h_{trans}$, as analyzed by Lahaie and Bouchard
- Grain boundary sliding for $h \leq h_{trans}$, as experienced in creep

The average stress is thus be given by:

$$\langle \sigma \rangle = \int_{0}^{h_{trans}} \sigma_{creep} \cdot \Psi_{\ln} \cdot dh + \int_{h_{trans}}^{\infty} \sigma_{visc} \cdot \Psi_{lin} \cdot dh \qquad (5)$$

where, σ_{visc} is the lubricated component of the stress:

$$\sigma_{visc} = \frac{\mu \dot{\varepsilon}}{9}\left[\frac{f_s^m}{1-f_s^m}\right]^3 \left[\left[1-1/2\left[\frac{f_s^m}{1-f_s^m}\right]\varepsilon\right]^{-3} + 2\left[1+\left[\frac{f_s^m}{1-f_s^m}\right]\varepsilon\right]^{-3}\right] \qquad (6)$$

and σ_{creep} is deduced from a creep law as:

$$\sigma_{creep} = K_0 \exp\left[\frac{pQ}{RT}\right] \cdot \dot{\varepsilon}^{p} \qquad (7)$$

The transition value for h (h_{trans}) corresponds to the channel thickness where the stress produced by hydrodynamic forces is equal to the creep stress. For a given applied strain and strain rate, h_{trans} is calculated by first solving the following equation for $f_{s\,trans}$:

$$\sigma_{\text{visc trans}} = \frac{\mu \dot{\varepsilon}}{9}\left[\frac{f_{\text{s trans}}^m}{1-f_{\text{s trans}}^m}\right]^3 \left[\left[1-1/2\left[\frac{f_{\text{s trans}}^m}{1-f_{\text{s trans}}^m}\right]\varepsilon\right]^{-3} + 2\left[1+\left[\frac{f_{\text{s trans}}^m}{1-f_{\text{s trans}}^m}\right]\varepsilon\right]^{-3}\right] = \sigma_{creep} \qquad (8)$$

Equation (4) can be used to obtain h_{trans} from $f_{s\,trans}$. Once h_{trans} is known for a given strain, the average stress can be calculated with Equation (6), which becomes, after insertion of the respective expression for σ_{visc} (Equation 1) and σ_{creep} (Equation 7):

$$\begin{aligned}\langle\sigma\rangle = {} & K_0 \exp\left[\frac{pQ}{RT}\right]\cdot\dot{\varepsilon}^{p}\int_0^{h_{trans}}\Psi_{\ln}\cdot dh + \\ & \frac{\mu\dot{\varepsilon}}{9}\int_{h_{trans}}^{\infty}\left[\frac{f_s^m}{1-f_s^m}\right]^3\left[\left[1-1/2\left[\frac{f_s^m}{1-f_s^m}\right]\varepsilon\right]^{-3}+2\left[1+\left[\frac{f_s^m}{1-f_s^m}\right]\varepsilon\right]^{-3}\right]\cdot\Psi_{\ln}\cdot dh\end{aligned} \tag{9}$$

The first integral is the well-known cumulative function of the log-normal distribution. The second integral can be performed using the relationship existing between h and f_s, so that the average stress is finally given by:

$$\begin{aligned}\langle\sigma\rangle = {} & K_0 \exp\left[\frac{pQ}{RT}\right]\cdot\dot{\varepsilon}^{p}\int_0^{h_{trans}}\Psi_{\ln}\cdot dh + \frac{\mu\dot{\varepsilon}}{9}\cdot\frac{m}{\ln\phi_g\sqrt{2\pi}}\cdot \\ & \int_0^{f_{strans}}\frac{f_s^{3m-1}}{(1-f_s^m)^4}\left[\left[1-1/2\left[\frac{f_s^m}{1-f_s^m}\right]\varepsilon\right]^{-3}+2\left[1+\left[\frac{f_s^m}{1-f_s^m}\right]\varepsilon\right]^{-3}\right]\cdot \\ & \exp\left\{-\frac{1}{2(\ln\phi_g)^2}\left[\ln\left(\frac{f_s^m}{1-f_s^m}\right)+\ln\left(\frac{f_{smean}^m}{1-f_{smean}^m}\right)+\frac{1}{2}(\ln\phi_g)^2\right]^2\right\}\cdot df_s\end{aligned} \tag{10}$$

Notice that the mean fraction solid has to be evaluated according to the temperature distribution inside the test zone.

APPENDIX B

Symbol	Meaning	Unit
C^*	concentration at the solid/liquid interface	wt. %
C_o	initial alloy concentration	wt.%
C_e	eutectic concentration	wt.%
C_p	specific heat	J/kg K (or °C)
D	diffusion coefficient in liquid	m^2/s
G	volume free energy	J/mol
	thermal gradient	K (or °C)/m
G_c^*	thermal gradient at the interface in liquid	K (or °C)/m
G_s^*	thermal gradient at the interface in solid	K (or °C)/m
I_{soc}	isothermal compressibility	Pa
K	proportionality coefficient	
K_1, K_2	constant in classic heterogeneous nucleation	
L	latent heat of fusion per volume	J/m^3
N_0	number density of nucleating sites	
P	Peclet number	-
R	dendrite tip radius	m
	growth velocity	m/s
$\bar{R}$	mean radius of equiaxed dendrite	m
R_g	radius of a equiaxed grain envelope	m
R_{tot}	final equiaxed grain radius	m
T	temperature	K, °C
T^*	liquid/solid interface temperature	K, °C
$\dot{T}$	cooling rate	K (or °C)/s
T_{cg}	coalescence temperature	K, °C

T_m	melting point of pure metal	K, °C
T_l	liquidus termperature of alloy	K, °C
T_{mf}	temperature of mass feeding	K, °C
T_n	nucleation temperature	K, °C
T_o	termperature of bulk liquid	K, °C
T_q	measurable temperature	K, °C
$\mathrm{T_s}$	solidus tempreature	K, °C
V	liquid/solid interface movement rate	m/s
	dendrite tip growth velocity for columnar growth	m/s
	growth velocity for equiaxed growth	m/s
a	grain size	m
f_g	volume fraction of equiaxed dendritic grain	
f_i	internal solid fraction of equiaxed dendritic grain	
f_l	liquid fraction	
f_s	fraction solid	
h	liquid film thickness	m
h_0	initial liquid film thickness	m
h_i	limiting film thickness on inclined channel	m
h_{med}	median value of liquid channel thickness	m
h_{trans}	transit liquid channel thickness	m
k	partition coefficient	
	permeability	
k_1, k_2, k_3	adjustable parameters in heterogeneous nucleation	
l	length of the hot spot	m
m	liquidus slope	K (or °C)/wt.%
	grain type parameter	
n	nucleation sites density	$\mathrm{m^{-3}}$

	constant		
n_o	initial nucleation site density		m^{-3}
$\dot{n}$	nucleation rate		$m^{-3}s^{-1}$
p	complemented distribution coefficient	1-k	
q_e	external heat flux		W/m^2
q_i	internal heat source		W/m^2
r	radius		m
r^*	critical size of radius		m
t_f	local solidification time		s
t_r	time available for stress relaxation processes		s
t_v	vulnerable time period for tears to spread		s
x	coordinate in s/l interface		m
y	coordinate in s/l interface		m
z	coordinate perpendicular to planar s/l interface		m
ΔC	concentration difference between liquidus and solidus		wt.%
ΔG	change of free energy		J/mol
ΔG_v	change of volume free energy		J/mol
$\Delta P_c, dP_c$	cavitation depression		Pa
$\Delta P_{max}, dP_{max}$	maximum pressure drop		Pa
$\Delta P_{mec}, dP_{mec}$	pressure drop caused by deformation		Pa
$\Delta P_{sh}, dP_{sh}$	pressure drop caused by shrinkage		Pa
ΔT	undercooling		K, °C
ΔT_c	concentration undercooling		K, °C
	growth undercooling of the columnar dendrites		K, °C
ΔT_o	liquidus-solidus range at C_o		K, °C
ΔT_{max}	maximum undercooling at recalescence		K, °C

ΔT_n	critical nucleation undercooling		K, °C
ΔT_N, dT_N	average nucleation undercooling		K, °C
ΔT_σ, dT_σ	standard deviation of nucleation		K, °C
Γ	Gibbs-Thomson coefficient		
	Isothermal compressibility		Pa
$\Psi_{\ln}$	probability density of liquid channel thickness		
Ω	dimensionless solutal supersaturation		-
α	coefficient of thermal expansion		
β	Shrinkage factor	ρ_S/ρ_L-1	
γ	surface tension		J/m^2
$\gamma_{l/g}$	liquid/gas surface energy		J/m^2
δ, δ_c	solute boundary layer thickness in liquid		m
ε	strain		
ε_0	equivalent strain		
ε_{fr}	dependent critical strain		
$\varepsilon_{p\max}^{ii}$	plastic strain		
ε_{cr}	critical strain		
$\dot{\varepsilon}$	strain rate		
$\dot{\varepsilon}^{el}$	elastic strain rate		
$\dot{\varepsilon}^{vp}$	visco-plastic strain rate		
$\dot{\varepsilon}^{th}$	thermal contraction strain rate		
$\dot{\varepsilon}^{tr}$	transformation strain rate		
κ	thermal conductivity		W/m K (or °C)
λ_1	primary dendrite arm spacing		m

λ_2	secondary dendrite arm spacing	m
μ	viscosity of liquid	kg/m*s or Pa*s
v_T	velocity of the isotherms	m/s
ρ	density	kg/m^3
ρ_l	density of liquid	kg/m^3
ρ_s	density of solid	kg/m^3
σ	tensile strength	Pa
σ_f	fracture stress	Pa
σ_i	accumulated stress in the semi-solid body	Pa
σ_{creep}	creep mechanisms related stress	Pa
σ_{visc}	viscosity mechanisms dependable stress	Pa
ϕ_g	microstructure relevant geometric standard deviation	

REFERENCES

---

1 M. C. Flemings, ***Solidification Processing***, McGraw-Hill, USA, 1974.

2 W. Kurz, D. J. Fisher, ***Fundamentals of Solidification***, Trans Tech. Publications, 1998.

3 John D. Verhoeven, ***Fundamentals of Physical Metallurgy***, John Wiley & Sons, 1975.

4 Modeling for Casting and Solidification Processing, Edited by Kuang-O Yu, Marcel Dekker, Inc., 2002.

5 J. Campbell, ***Castings***, (Oxford, UK: Butterworth – Heinemann Ltd, 1991).

6 Robert W. Cahn and Peter Haasen, Physical Metallurgy, Fourth, Revised and Enhanced Edition, North-Holland, 1996, p.784.

7 J. D. Hunt, ***Steady State Columnar and Equiaxed Growth of Dendrites and Eutectic***, Materials Science and Engineering, 65 (1984), p75-78.

8 M. Rappaz and Ch. A. Gandin, 1993, Acta, Metall. Mater. 41, p345.

9 L. J. Ledgard and D. G. McCartney, ***Unidirectional Steady State Growth of Grain Refined Aluminum Alloys***, Proceeding of the 4th Decennial International Conference on Solidification Processing, Sheffield, July 1997, p.277-280.

10 Grandfield John F., Davidson Cameron J. and Taylor John A., ***The Columnar to Equiaxed Transition in Horizontal Direct Chill Cast Magnesium Alloy AZ91***, Light metals 2001, Edited by J. L. Anjier, TMS, 2001, p911-916.

11 S. G. R. Brown and J. A. Spittle, ***A 2D Implicit Finite Difference Model to Simulate the Columnar to Equiaxed Zone Transition***, Modeling of Casting, Welding and Advanced Solidification Processes – V, Sept. 16-21, 1990, p395-402.

12 ***Aluminum and Aluminum Alloys***, ASM Specialty Handbook, 1993.

13 Alicia E. Ares, Carlos T. Rios, Rubens Caram and Caros E. Schvezov, ***Dendrite Spacing in Al-Cu and Al-Si-Cu Alloys as Function of the Growth Parameters***, Light Metals 2002, Edited by Wolfgang Schneider, TMS, 2002.

14 Ravi Vijayaraghavan, Nagendra Palle, James Boileau, Jake Zindel, Randy Beals and Fred Bradly, ***A Micro-Model for Aluminum-Silicon Alloys***, Scripta Materialia, Vol.35, No.7, 1996, p861-867.

15 M. Rappaz, ***Modeling of Microstructure Formation in Solidification Processes***, International Materials Reviews 1989, Vol.34 No.3, p93-123.

16 Tony C. Midea, ***1999 Casting Simulation Software Survey***, Modern Casting, May 1999.

17 J. Du, B. S. -J. Kang, K. -M. Chang and J. Harris, ***Computational Modeling of D. C. Casting of Aluminum Alloy Using Finite Element Method***, Light Metals 1998, p1025-1030.

18 M. F. Horstemyer, ***Mapping Failure by Microstructure-Property Modeling***, JOM September 2001, p24-27.

19 Nigel Saunders, ***Modeling of Solidification in Al-Alloys***, Light Metals 1997, Edited by Reidar Huglen, p911-918.

20 X. Yang, ***Modeling of Microstructure in Solidification – A literature Survey***, UQAC/CSMA, March 1997.

21 Arild Håkonsen, Dag Mortensen, Steinar Benum and Erik Vatne, ***A Micro/Macro Model for the Equiaxed Grain Size Distribution in DC Casting Aluminum Ingots***, Light Metals 1999, p921-827.

22 Ph. Thévos, J. L. Desbiolles and M. Rappaz, Metall. Trans., 1989, 20A, p311.

23 J. L. Desbiolles, Ph. Thévos and M. Rappaz, ***Modeling of Equiaxed Dendritic Microstructure Formation in Castings***, Modeling of Casting and Welding processes IV (1988), p625-634.

24 Ph. Thévoz, ***Solidification Cours***, Switzerland, May 21-26, 2000.

25 Elizabeth A. Holm and Corbett C. Battaile, ***The Computer Simulation of Microstructural Evolution***, JOM, September 2001, p20-23.

26 L. Nastac, Numerical Modeling of Solidification Morphologies and Segregation Patterns in Cast Dendritic Alloys, Acta Mater. Vol.47, no.17, 1999, p4253-4262.

27 D. C. G. Lees, ***The Hot-tearing Tendencies of Aluminium Casting Alloys***, J. Inst. Metals, 1946, 72, pp.343-364.

28 Bruno Hannart, Frédéric Cialti, Ruben Van Schalkwuk, ***Thermal Stresses in DC Casting of Aluminum Slabs: Application of a Finite Element Model***, Light Metals, 1994, pp.879-887.

29 H.F. Bishop, C.G. Ackerlind, W.S. Pellini, ***Metallurgy and Mechanics of Hot Tearing***, Trans AFS 60(1952) p818-833.

---

30 Dr. J. Verö, ***The Hot-Shortness of Aluminium Alloys***, The Metal Industry, April 10, 1936, p431-442.

31 Stephen Instone, ***The Development of a Hot Cracking Test***, Proceedings of Material 1998, p125-130.

32 ***Solidification Structure of Aluminum Alloy Ingots Metallography***, Microstructures, and Phase Diagrams, p523-531.

33 Pellini W.S., ***Strain Theory of Hot Tearing***, Foundry, 80, (1952).

34 Dodd, R. A. ***Hot-tearing of Castings: A Review of the Literature***, Foundry Trade Journal, Sep. 20, (1956), p321-331.

35 Singer, A.R.E. and Jennings, P. H., Journal Inst. of Metals, vol. 72, 1946, 197.

36 C.H. Dickhaus, L. Ohm, S. Engler, ***Mechanical Properties of Solidifying Shell of Aluminum Alloys***, AFS Transaction 93-18, p677-684.

37 F. Paray, B. Kulunkt and J. E. Gruzleski, ***Hot Tearing in 319 Alloy***, Int. J. Cast Metals Res., 2000, 13, p147-159.

38 R. G. Liptai and C. A. Tatro, ***In Proceedings, Fourth Annual Symposium on Nondestructive Testing of Aircraft and Missile Components***, Southwest Research Institute, San Antonio, Texas, 1963, p287-341.

39 J. –M. Drezet, M. Rappaz, B. Carrup, and M. Plata, ***Experimental Investigation of Thermomechanical Effects During Direct Chill and Electromagnetic Casting of Aluminum Alloys***, Metallurgical and Materials Transitions, vol.26B, August 1995, p821-829.

40 H. A. Suhartono, K. Pötter, A. Schram, and H. Zenner, ***Modeling of Short Crack Growth Under Biaxial Fatigue: Comparison Between Simulation and Experiment, Mutiaxial Fatigue and Deformation: Testing and Prediction***, ASTM STP 1387, S. Kalluri and P. J. Bonacuse, Eds., American Society for Testing and Materials, West Conshohocken, PA, 2000, pp. 323-339.

41 I. Farup, J. –M. Drezet and M. Rappaz, ***In Situ Observation of Hot Tearing Formation in Succinonitrile-Acetone***, Acta Mater. 49 (2001), p1261-1269.

42 P. –D. Grasso, J. –M. Drezet, and M. Rappaz, ***Hot Tear Formation and Coalescence Observation in Organic Alloy***, http://www.tms.org/pubs/journals/JOM/0201/Grasso/Grasso-0201.html.

43 Ivar Farup and Asbjørn Mo, ***Two-Phase Modeling of Mushy Zone Parameters Associated With Hot Tearing***, metallurgical and Materials Transactions, Vo.31A, May 2000, p1461-1472.

---

44 M. Rappaz, I. Farup and J. –M. Drezet, ***Study and Modeling of Hot Tearing Formation, Proceeding of the Merton C. Flemings Symposium on Solidification and Materials Processing***, Edited by R. Abbaschian, H. Brody and A. Mortensen, 2001, p213-222.

45 W. M. van Haaften, W. H. Kool and L. Katgerman, ***Microstructural Observations of Cracking in AA5182 at Semi-Solid Temperatures***, Materials Science Forum Vols.331-337 (2000), p265-270.

46 W. I. Pumphrey, J. V. Lyons, ***Cracking During the Casting and Welding of the More Common Binary Aluminium Alloys***, J. Inst. Met., 1947, 74, p439-455.

47 J. Campbell and T.W. Clyne, Hot Tearing in Al-Cu Alloys. Cast Metals, vol. 3 (1991), p224-226.

48 P. Suvanchai, T.Okane, and T.Umeda, ***Deformation Behavior of Aluminium Alloys During Solidification***, Proceeding of the 4th Decennial International Conference on Solidification Processing, Sheffield, July 1997, p190-194.

49 D.Warrington and D.g.McCartney, ***Hot-cracking in Aluminium Alloys 7050 and 7010 – a Comparative Study***, CAST Metals vol.3, no.4 1991, p202-208.

50 Ludger Ohm, Siegfried Engler, ***Festigkeitseigenschaften Erstarrender Randschalen aus Aluminumlegierung***, Giesserei Forschung, Nr.3 & 4 (1990), p137-147 and 149-162.

51 C. S. Wu, ***Causes of the Formation of Longitudinal Surface Cracks on the DC-Cast 7039 Aluminium Alloy***, Journal of Materials Science, Vol.23, No.2 1988.

52 Tony Overfelt, ***The Manufacturing Significance of Solidification Modeling***, JOM June (1992) p17-20.

53 H. Fjær, A.Mo, ***Mathematical Modeling of Thermal Stresses During D.C. Casting of Aluminum Billets***, Light Metals, 1990, p945-949.

54 G.Upadhya, S. Cheng and U. Chandra, ***A Mathematical Model for Prediction of Hot Tears in Castings***, Light Metals, 1995, p1101-1108.

55 U. Chandra, ***Computer Prediction of Hot Tears, Hot Cracks, Residual Stresses and Distortions in Precision Castings: Basic Concepts and Approach***, Light Metals 1995, pp.1107-1117.

56 J. –M. Drezet, M. Rappaz and Y.Krähenbühl, ***Modeling of Thermomechanical Effects During Direct Chill Casting of AA1201 Aluminum Alloy***, Materials Science Forum Vols. 217-222 (1996), p305-310.

57 A Giron, M. G. Chu, and H. Yu, ***Effete of Mushy Zone Mechanical Properties on the Calculate Stresses and Deformations During the Casting Aluminum Alloy***, Light Metals 2000, p579-584.

58 Clyne, T.W. and Davies, G.J., ***Comparison Between Experimental Data and Theoretical predictions Relating to Dependence of Solidification Cracking on Composition***, in: Solidification and Casting of Metals (London, UK: Metals Society Conference, 1979), p275-278.

59 L. Katgerman, ***A Mathematical Model for Hot Cracking of Aluminum Alloys During D.C. Casting***, Light Metals, AIME 1981, p845-853.

60 P. N. Hasen, Varmrevner I Stobestal, Danmarks Tekniske, Hojskole and Lyngby, 1975.

61 U. Feurer, Giesserei Forschung 28, Nr.2 (1976), p25-29.

62 E. Flender, P. N. Hasen, P. R. Sahm, Giesserei Forschung 39, Nr.4 (1987), p137-149.

63 Sellars, C.M., Inst. Met., Reviews, 17 (1972).

64 D. J. Lahaie and Dr. M. Bouchard, ***Physical Modeling of the Deformation Mechanisms of Semi-Solid Bodies and a Mechanical Criterion for Hot Tearing***, Metallurgical and Materials Trancaction B, Vol.B August 2001, p697-705.

65 F. Decultieux, P. Vicente-Hernandez, C. Levailant, ***Hot Tearing Test: Experiments and FEM Modeling, Modeling of Casting***, Welding and Advanced Solidification processes VI 1993, p617-624.

66 Liangyi Zhao, Baoyin, Na Wang, Sahajwllla and R. D. Pehlke, ***The Rheological Properties and Hot Tearing Behavior of an Al-Cu Alloy***, Int. J. Cast Metals Res., 2000, 13, p167-174.

67 B. Magnin, L. Maenner, L. Katgerman. S. Engler, ***Ductility and Rheology of an Al-4.5%Cu Alloy from Room Temperature to Coherency Temperature***, Materials Science Forum Vols. 217-222 (1996), p1209-1214.

68 E. R. De Freitas and M. Ferrante, ***Rheological Behaviour and Deformation Characteristics of a Commercial and a Laboratory-Cast Al-4.5%Cu Alloy in the Semi-Solid State***, Acta Mater., 49 (2000), p3839-3847.

69 J.-M. Drezet and M. Rappaz, ***Direct Chill Casting of Aluminum Alloys: Ingot Distortion and Stress Build-up***, The 4th decennial International Conference on Solidification processing, SP'97, Sheffield, UK, 7-10 July 1997.

70 S. Cheng, S. Sundarraj, J. Jo, U. Chandra, ***Computer Prediction of Hot Tears in Castings***, ASME-HTD vol.323, 1996, p59-68.

---

71 A. K. Dahle, S. M. Nabulsi, D. H. St. John, ***Thermo-Mechanical Basis for Understanding and Predicting Hot Tearing During Solidification***, AFS Transactions, 98-33 p137-142.

72 M. Rappaz, J.-M. Drezet, and M. Gremaud, ***A New Hot-Tearing Criterion***, Metallurgical and Materials Transactions Vol.30A, February 1999, p449-455.

73 J.-M. Drezet and M. Rappaz, ***Prediction of Hot Tears in DC-cast Aluminum Billets***, Light Metals 2001, TMS, 2001, p887-893.

74 John F. Grandfield, Cameron J. Davidson and John A. Taylor, ***Application of a New Hot Tearing Analysis to Horizontal Direct Chill Cast Magnesium Alloy AZ91***, TMS, 2001, p895-901.

75 M. Rappaz, Hot Tearing and Stress-related Defects, ***Solidification Course 2000***, Les Diablerests, Switzerland, May 21-26, 2000.

76 K.C. Chiang and H. L. Tsai, ***Interaction Between Shrinkage-Induced Fluid Flow and Natural Convection During Alloy Solidification***, Int. J. Heat Mass Transfer, Vol. 35, No. 7, 1992, p1771-1778.

77 Mohammed M'Hamdi and A. Mo, ***Microporosity and Other Mushy Zone Phenomena Associated with Hot Tearing***, Light Metals 2002.

78 X. Yang, M.Ö. Pekgüleryüz, ***Modeling of Microstructure of Al Alloys in a Laboratory Scale DC-Simulator***, Light Metals 1999, Proceedings of the International Symposium on Light Metals 1999, Edit. M. Bouchard and A. Faucher, p301-314.

79 X. Yang, M.Ö. Pekgüleryüz and M. Bouchard, ***Modeling of Solidification of Al Alloys in a Laboratory Scale DC-Simulator***, Light Metals, TMS, 2000.

80 J. Langlais and J. E. Gruzleski, ***A Novel Approach to Assessing the Hot Tearing Susceptibility of Aluminium Alloys***, Materials Science Forum, vols. 331-337 (2000), p167-172.

81 ***Aluminum: Properties and Physical Metallurgy***, edited by John E. Hatch, ASM, American Society for Metals, 1984, p47.

82 S. Chan and D. M. Stefanescu, ***A Model for Macrosegregation and its Application to Al-Cu Castings***, Metallurgical and Material Transactions A, Vol.27A, Sept. 96, p2713.

83 J. D. Hunt and R. W. Thomas, ***Alloy***, p29.

84 Lennart Bäckerud, Ella Krol, Jarmo Tamminen, ***Solidification Characteristics of Aluminum Alloys***, SkanAluminum universitetsforlaget AS, vol.1 (Wrought Alloys), 1986.

85 J. -M. Drezet and M. Rappaz, ***Modeling of Ingot Distortions During Direct Chill Casting of Aluminum Alloys***, Metallurgical and materials Transitions A, Vol. 27A, October 1996, p3214-3225.

86 M. Fortin, D. J. Lahaie and M. Bouchard, ***Mold Surface Roughness Effects on the Microstructure and Hot Tearing Strength for an Al-4.5%wtCu Alloy***, TMS 2001.

87 J. R. Dryden, D. Kucerovsky, D. S. Wilkinson and D. F. Watt, ***Creep Deformation due to a Viscous Grain Boundary Phase***, Acta metal. Vol.37, No.7, p2007-2015, 1989.

88 G. K. Sigworth, ***Hot Tearing of Metals***, AFS Trans., 1999, p1053-1062.

89 T. G. Nguyen, D. Favier, and M. Suery, ***Theoretical and Experimental study of the Isothermal Mechanical Behaviour of Alloys in the Semi-Solid State***, International Journal of Plasticity, Vol. 10, No.6, 1994, p663-693.

90 W. M. van Haaften, W. H. Kool and L. Katgerman, ***Tensile Behavior of DC-cast AA5182 in Solid and Semi-solid State***, p239-244.

91 M. Braccini, C. L. Martin, M. Suéry and Y. Bréchet, ***Hot tearing Phenomena in Al-Cu Alloys: Grain Refinement Effect***, Matériaux & techniques N° 5-6 2000, p19-24.

92 N. A. Gokcen, ***Thermodynamics***, 1975, p455.

93 Y. M. Haddad, ***Viscoelasticity of Engineering Materials***, 1995.

94 D. Larouche, ***A constitutive Model for the Tensile Deformation of a Binary Aluminum Alloy in the Semisolid Interval***, August 2002.

95 M. C. Schneider, S. Andersen, ***Simulated Analysis of Macrosegregation, Hot Tears and Heat Treatment in Steel Castings***, AFS Transactions 99-90, p547-554.

96 Florent Decultieux, Michel Bellet, Alain Lefloch, Denis Delagnes and Christophe Levaillant, ***Development of Stress During the Solidification of an Aluminium Alloy: Experimental and Numerical Assessment of Influence of Elasticity Parameters During Solidification***, The 4th Decennial International Conference on Solidification processing, SP'97 Sheffield, UK, 7-10 July 1997, p195-197.